DASA Report Number 1889

Final Report

"Further Detailed Analysis of Telemetry Records Obtained by Explorer IV Satellite Concerning Geomagnetically Trapped Radiation"

Defense Atomic Support Agency, Washington, D. C., 20301;

Contract No. DA-49-146-XZ-494: "Research concerning analysis of telemetry records."

Period of contract: 1 November 1965 - 30 November 1966

Personnel
A. H. Weber, Principal Investigator
A. F. Briskeh, Graduate Student, M.S. program (physics)
M. E. Coughlin, Undergraduate Research Aide
J. F. Fennell, Graduate Student, Ph.D. program (physics)
J. A. George, Associate Professor of Aerospace Engineering, Parks College, Saint Louis University
Wm. K. Kottmeyer, Graduate Student, M.S. program (physics)
D. J. Manson, Post-doctorate Research Associate
J. R. Ockerse, S.J., Graduate Student, M.S. program (physics)
J. M. Paikeday, Post-doctorate Research Associate

DASA Project Officer
Dr. Charles A. Blank
Radiation Division
Defense Atomic Support Agency
Department of Defense
Washington, D. C.

30 November 1966

Saint Louis University

Physics Department

St. Louis, Missouri 63103

Final Report - Defense Atomic Support Agency Contract No. DA-49-146-XZ-494

Acknowledgments

1. This research was supported by the Department of Defense, Defense Atomic Support Agency, Radiation Division, under Contract No. DA-49-146-XZ-494. In addition to the funding support of DASA, the authors wish to express their considerable appreciation of the valued cooperation and help of Dr. Charles A. Blank of the same division.

2. Dr. Juergen K. Bock, recently of the Nuclear Physics Branch of the Ballistic Research Laboratories, Aberdeen Proving Ground, Maryland, rendered essential scientific aid in the present work. E. O. Baicy, Chief of the Nuclear Physics Branch of BRL was instrumental in effecting scientific liaison between his branch and the group in the physics department of Saint Louis University. The assistance of BRL in this scientific work was indispensable.

3. The Yalem Computer Center, Saint Louis University, rendered invaluable services via unrestricted time on the IBM-1620 Computer.

4. Washington University Computing Facilities, through National Science Foundation Grant G-22296, rendered valuable assistance and support of the present project during the last three months of the contract period.

5. The assistance of Messrs. Roy Cochran and D. G. Aichele of the staff of the Computation Laboratory, George C. Marshall Space Flight Center, Huntsville, Alabama is especially acknowledged. These computer experts provided a new group of "playbacks" of the set of telemetry tapes selected for analysis in the present work. These playbacks were much superior in elimination of noise and clarity of record to the group of records which were originally available. The availability of these new high quality playbacks enabled considerable improvement in the analysis.

Contents

Abstract

This report (Preface P1, P2; Parts A-E) is essentially a Summary of the five M.S. Theses and Ph.D. Dissertations completed during the contract year for contract No. DA-49-146-XZ-494. The titles of these theses and dissertations are the heading titles for each of the five Parts A-E.

This Final Report is more than a mere Summary since all results have been condensed, compared, corrected and interpreted as a group. Figures A8, C14 and D4 exhibit count-rates and/or particle flux densities, both for the Natural and the ARGUS Events 1 and 2 radiations, in 3-dimensional B-L coordinates. These 3-dimensional plots exhibit most clearly the coordination of all the data and are presented for the first time in this Summary Final Report.

P1. Preface - Glossary

SYMBOL	DEFINITION
A	Nucleon number (Ref. P1, Sec. 1)
$\hat{A}$	Vector, along axis of minimum moment of inertia Explorer 4. Also the direction of the satellite symmetry axis. (Ref. P1, Fig. 2.2).
A_{eff}	Effective area (product of counter efficiency and geometric area A) of directional counter Explorer 4 (cm^2)
a_i	Scale height for atmospheric model defined by $a_i = \frac{1}{h_{i+1} - h_i} \ln \frac{N_i}{N_{i+1}}$, where N_i = number/unit volume at altitude h_i where h_i is the altitude in kilometers (Ref. P2)
a	Equatorial radius of international ellipsoid (km)
A_p	Daily equivalent planetary amplitude (Ref. P3, Sec. 1.5)
a_p	Three-hour equivalent planetary amplitude (Ref. P3, Sec. 1.5)
$\vec{B}$	Geomagnetic flux density vector (gauss)
$\hat{B}$	Geomagnetic flux density unit vector, $\vec{B}/B$
$\hat{B}_o$	Magnetic flux density unit vector at the time the satellite inertial coordinate system is established (time of any rf-null prior to data to be analyzed)
B_m	Mirror point value of B (gauss)
$B_\perp$	A vector in the plane perpendicular to the magnetic flux density vector B (gauss)
B_x, B_y, B_z	Components of a unit vector B in Vernal Equinox coordinates
B_e	Equatorial value of B
b	Polar radius of international ellipsoid
b_1, b_2, b_3	Components of $\hat{B}$ on the X_s, Y_s, Z_s axes of satellite inertial coordinate system (Ref. P1, Eq. (3.14))

b_n, b_e, b_d	Normalized (divided by B) components in topcentric coordinate system of ephemeris (north, east, down)
C	Omnidirectional count-rate corrected for deadtime (sec^{-1})
c	Speed of light in free space
C'	Observed count-rate corrected for counter dead-time (sec^{-1})
$C_{obs}(\theta)$	Observed directional count-rate for detector A (sec^{-1})
C_{obs}	Omnidirectional observed count-rate (sec^{-1})
$C(\theta)$	True directional count-rate ($C_{obs}(\theta)$ corrected for deadtime, efficiency and effective area) ($sec^{-1} cm^{-2}$)
$C(\tau)$	Auto-covariance function (Ref. P1, P4, Eq. (A1.2))
E	Kinetic energy of a particle
$\vec{E}$	Electric field vector
e	Electronic charge
$f(h')$	Mirror-point density (Ref. P2, Eq. (2.24))
$F(\alpha, \phi)d\Omega$	Fraction of particles with directions within $d\Omega$ at (α, ϕ) (Ref. P3, Sec. 4.5)
(f)	Fraction of fission electrons that penetrate a shielding (Ref. P3, Sec. 2.4)
H	Receiver antenna height above the international ellipsoid (mean sea level) (earth radii)
H, H_R	Relativistic Hamiltonian (Ref. P3, Sec. 3.2)
h	Distance measured from the center of the earth to a field line (km)
I	Parameter related to the longitudinal invariant (Ref. P3, Eq. (3.22))
I(E)	Omnidirectional intensity of particles with energy greater than E (Ref. P3, Eq. (4.38))
i(E)	Omnidirectional spectral intensity (Ref. P3, Eq. (4.32))
$I_p(x)$	Modified Bessel function of order p
$I_{x'}$	Moment of inertia about the X' axis
$I_{y'}$	Moment of inertia about the Y' axis

$I_{z'}$	Moment of inertia about the Z' axis
$J_1(x)$	First order Bessel function regular at the origins
$j(\alpha, \phi; E)$	Unidirectional spectral intensity (Ref. P3, Eq. (4.32))
$J(\theta')$	Directional flux density of particles as a function of angle between J and a plane perpendicular to B
J_o	Omnidirectional flux density (particles $cm^{-2}sec^{-1}$)
ℓ	Length of nose cone and instrument section Explorer 4
$\hat{L}$	Angular momentum unit vector
L	McIlwain's geomagnetic shell parameter (earth radii)
M	Earth dipole moment (Ref. P3, Eq. (1.9))
m	Relativistic mass of electron
m_o	Rest mass of electron
N	The number of digitizer counts per digitizing interval T
N(E)	Absolute differential spectral intensity, electrons/fission/MeV (Ref. P3, Eq. (1.5))
$n_{i+1}-n_i$	The number of digitizer counts measured to correspond to one frequency change (flip) on data record
n	Index of refraction (Ref. P3, Eq. (4.10))
$\vec{P}$	Relativistic particle momentum; also a transformation parameter in the conversion from B-L to R-λ (Ref. P3, Eq. (1.13))
$\hat{P}$	Counter symmetry axis unit vector
$P_\perp$	Component of particle momentum perpendicular to the magnetic flux density vector B
$P_\parallel$	Component of particle momentum parallel to the magnetic flux density vector B
P(f)	Relative spectral intensity of frequency f (Ref. P1, Eq. (A1.1))
r	Distance of a particle from the center of the earth (km)
$\vec{R}$	Vector from center of earth to tracking station in Vernal Equinox coordinates (km)

$\vec{r}$	Vector from center of earth to satellite in Vernal Equinox coordinates (km)
R_e	Radius of the earth, 0.63712×10^7 meters
r_e	Equatorial distance from dipole center to B line (km)
R_E	Extrapolated range of particles penetrating an absorber (Ref. P1, P3, P4; gm cm^{-2})
$R_{1/2}$	Range for 50 percent transmission of radiation through an absorber (gm cm^{-2})
S	Scaling factor - twice the number of accumulated particle counts corresponding to one frequency change on the data record (particle counts per flip-flop)
s	Normalized particle momentum (Ref. P3, Sec. 4.23)
$S(\alpha)$	Detector A response function (Ref. P4)
S_{ij}	Matrix element representing the kernel of the integral equation relating the true count-rate $C(\theta)$ and the directional flux density $J(\theta')$
S(p)	A parameter in the transformation from B-L to R-λ (Ref. P3, Eq. (1.14))
T	Time interval selected for digitazation (usually 24 sec)
T_a	Longitudinal drift period (Ref. P3, Eq. (3.29))
T_b	Bounce period (Ref. P3, Sec. 3.26) (sec)
T_g	Cyclotron period (Ref. P3, Eq. (3.9)) (sec)
$T(\lambda)$	Bounce period of a particle with mirror-point at latitude λ_{gm} defined by Eq. (2.8) (Ref. P2) (sec)
t_i	Time at which particle count-rate for interval between frequency change (flip) is assigned (center of interval) (UT min)
t_o	Initial time of time interval T (UT min)
$\vec{U}$	Vector from tracking station to satellite
$\vec{V}_A$	Alfven velocity (Ref. P3, Eq. (4.6)) (km sec^{-1})
v	Speed of particle
W	Total energy (Ref. P3, Sec. 3.2)
X'	Axis of maximum moment of inertia Explorer 4

$\hat{X},\hat{Y},\hat{Z}$	Axes of Vernal Equinox inertial coordinate system; $\vec{X}$ in direction of Vernal Equinox of 1951; Y in earth's equatorial plane; $\vec{Z}$ to form right hand orthogonal system
$\hat{X}_r,\hat{Y}_r,\hat{Z}_r$	Axes of satellite fixed rotating coordinate system; $\vec{X}_r$ space fixed in direction of angular momentum vector L; Y_r in the direction of satellite symmetry vector A (rotating in a plane perpendicular to L in propeller-like motion); $\vec{Z}_r$ to form a right-hand orthogonal system
$\hat{X}_s,\hat{Y}_s,\hat{Z}_s$	Axes of satellite inertial coordinate system; $\vec{X}_s$ in direction of angular momentum vector L; $\hat{X}_s$-$\hat{Y}_s$ plane oriented to include B_o the magnetic flux density unit vector at time zero when an r-f null is observed; $\hat{Z}_s$ to form a right-hand orthogonal system
$Y_1(x)$	First order Bessel function irregular at the origin
Z	Atomic number of scattering atoms
Z'	Axis of minimum moment of inertia Explorer 4
α	Pitch angle. The angle between the particle momentum vector and the magnetic flux density vector (deg)
α_c	Pitch angle of the particle that defines the loss cone (deg)
β	Ratio of particle speed to speed of light in free space
γ	Relativistic mass ratio (Ref. P3), Spectral exponent (Ref. P3, Eq. (4.19))
γ	Phase angle of tumble motion of satellite
Δ	Geodetic latitude (radian)
Δ'	Geocentric latitude (radian)
Δ'_S	Geocentric latitude of satellite (radian)
δ	Phase angle of roll (spin) motion of satellite
ϵ	Detection efficiency of counter
η	Minimum scattering angle (Ref. P2) (deg)
$\textcircled{H}$	Hour angle of the Vernal Equinox (radian)
$\textcircled{H}_{gi}$	Angle between the Greenwich meridian and Vernal Equinox at t_i
$\textcircled{H}_E$	East longitude of the tracking station (radian)

ϵ	Euler angle specifying the opening angle of precession about angular momentum vector L (Ref. P1, P4, Fig. 2.5)
θ	Angle between the directional counter symmetry axis and the plane perpendicular to the magnetic flux density B; $\theta = \pi/2 - \alpha$ (deg); $\lambda = \pi/2 - \theta$
θ'	Angle between directional flux density vector J and the plane perpendicular to the magnetic flux density vector B (deg)
θ_s	East longitude of satellite from Vernal Equinox (radian)
λ_g	Geographic latitude (radian)
λ_{g*}	Conjugate geographic latitude (radian)
$\lambda_{gm'}$	Geomagnetic latitude (radian)
μ	Magnetic dipole moment
τ	Time parameter
τ_i, τ_D	G-M counter deionization (deadtime) (sec)
τ_D	Scintillation counter deadtime
ν	Whistler frequency (Ref. P3, Eq. (4.13))
ν_c	Cyclotron frequency (Ref. P3, Eq. (4.2))
ν_A	Hm wave frequency (Ref. P3, Eq. (4.2))
ϕ	Flux invariant (Ref. P3, Eq. (3.28))
ϕ	Euler angle measured in X-Y plane
$\dot{\phi}$	Precession rate about angular momentum vector L (rad sec^{-1})
ψ	Euler angle in the plane of rotation about Z'-axis from the line of nodes to the rotating satellite fixed X'-axis (deg)
$\psi(\theta')$	Element of an orthonormal set
$\dot{\psi}$	Residual angular velocity about Z'-axis after transition to propeller-like configuration (rad sec^{-1})
ω_p	Plasma frequency (Ref. P3, Eq. (3.28))
ω_L	Doppler shifted whistler frequency (Ref. P3, Eq. (4.7))
ω'_z	Angular velocity about Z'-axis (rad sec^{-1})
$(\omega'_z)_0$	Initial angular velocity about the Z'-axis at orbit insertion (rad sec^{-1})

References:

P1. "Van Allen Radiation Belt and ARGUS Directional Flux Density Distributions, Explorer 4 Satellite Data", Ph.D. Dissertation, D. J. Manson, February 1967, Saint Louis University, St. Louis, Missouri

P2. "Interpretation of Directional Flux Densities in ARGUS Shells, Explorer 4 Satellite Data", Ph.D. Dissertation, J. M. Paikeday, June 1966, Saint Louis University, St. Louis, Missouri

P3. "Omnidirectional Fluxes; Explorer 4 Satellite Data, ARGUS Events 1 and 2", Ph.D. Dissertation, J. A. George, February 1967, Saint Louis University, St. Louis, Missouri

P4. "Analysis of ARGUS/Explorer 4 Records", DASA 1613, January 1965, Saint Louis University, Physics Department, St. Louis, Missouri

P2. Preface - Calibrations, Corrections and Telemetry Information.

Table P2-1. Instrumentation calibration information, Explorer 4

Detectors	Channel	Deadtime (sec)	Effective Shielding ($gm\text{-}cm^{-2}$)	Particles (e, electrons; p, protons; ph, photons)	Saturation Counts (sec^{-1})	Geometric Factors $G_o(cm^2)$	Counter efficiency x effective area, $\epsilon A_{eff}, (cm^2)$; $\frac{1}{\epsilon A_{eff}} = \frac{f}{G_o}$
Detector A, Plastic Scintillation	2,5	91×10^{-6}, Van Allen (7); 112×10^{-6}, Baicy (2); 100×10^{-6}, SLU (3)	0.14 Al, of window, Van Allen (1)	$E_e > 0.58$ MeV, Van Allen (1); $E_e > 0.7$ MeV, Baicy (2); $E_p > 10$ MeV, Van Allen (1)	10×10^3 from max observed count-rates, SLU (3)	Response function $S(\alpha)$ Baicy (2)	0.0026, Baicy-Bock (6); 6.29×10^{-4} for photons, Baicy (2)
Detector C, Anton 302 G-M counter; unshielded	3	62.5×10^{-6} from max observed count-rates, SLU (3)	1.2 stainless steel (satellite shell), Van Allen (1) (=1.6 Al, SLU (4))	$E_e > 3$ MeV, $E_p > 30$ MeV, Van Allen (1)	2000 photons, Baicy (2); 5800 electrons from max observed count-rates, SLU (3)	$G_o = 0.60$ for fission electrons, SLU (4); $G_o = 0.37$ for protons in natural region, SLU using McIlwain (5)	0.015 for fission electrons, SLU (4); 0.32 for protons in natural region, SLU using McIlwain (5)
Detector D, Anton 302 G-M counter; shielded	1	62.5×10^{-6} assumed, same as Detector C	1.2 stainless steel +1.6 lead, Van Allen (1); (=3.88 Al, SLU (4))	$E_e > 5$ MeV, $E_p > 40$ MeV, Van Allen (1)	None	$G_o = 0.48$ for protons in natural region, SLU using McIlwain (5)	0.41 for protons in natural region, SLU using McIlwain (5)

E_e, electron energy
E_p, proton energy
E_{ph}, photon energy

Fig. P2-1. Block diagram, Explorer 4 instrumentation and telemetry

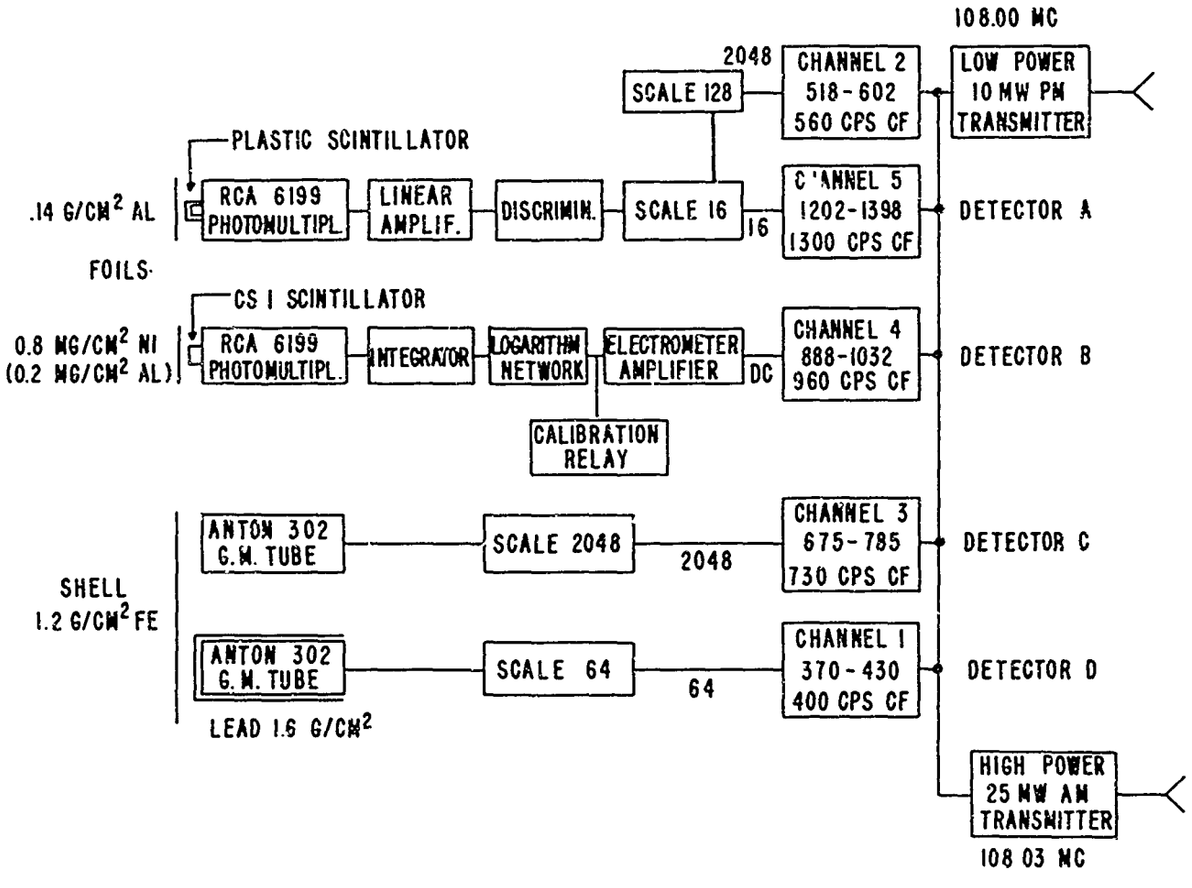
108.00 MC
2048
SCALE 128
CHANNEL 2
518-602
560 CPS CF
LOW POWER
10 MW PM
TRANSMITTER
PLASTIC SCINTILLATOR
.14 G/CM² AL
FOILS
RCA 6199
PHOTOMULTIPL.
LINEAR
AMPLIF.
DISCRIMIN.
SCALE 16
16
CHANNEL 5
1202-1398
1300 CPS CF
DETECTOR A
CS I SCINTILLATOR
0.8 MG/CM² NI
(0.2 MG/CM² AL)
RCA 6199
PHOTOMULTIPL.
INTEGRATOR
LOGARITHM
NETWORK
ELECTROMETER
AMPLIFIER
DC
CHANNEL 4
888-1032
960 CPS CF
DETECTOR B
CALIBRATION
RELAY
SHELL
1.2 G/CM² FE
ANTON 302
G.M. TUBE
SCALE 2048
2048
CHANNEL 3
675-785
730 CPS CF
DETECTOR C
ANTON 302
G.M. TUBE
SCALE 64
64
CHANNEL 1
370-430
400 CPS CF
DETECTOR D
LEAD 1.6 G/CM²
HIGH POWER
25 MW AM
TRANSMITTER
108 03 MC

P2-2. References

P2-1. Van Allen, J. A., et al, "Satellite Observations of Electrons Artificially Injected into the Geomagnetic Field", J. Geophys. Res. 64, 877-891 (1959).

P2-2. Baicy, E. O., "Calibrations of Explorer IV Prototype", DASA WT-1671 Ballistic Research Laboratory, Aberdeen Proving Ground, Maryland (October, 1963).

P2-3. 'Analysis of ARGUS/Explorer IV Records", DASA WT-1613, Saint Louis University, Physics Department, St. Louis, Missouri, (January, 1965).

P2-4. George, John A., "Omnidirectional Fluxes; Explorer 4 Satellite Data, ARGUS Events 1 and 2", Ph.D. Dissertation, Physics Department, Saint Louis University, St. Louis, Missouri (1967).

P2-5. McIlwain, C. E. and G. Pizzela, "On the Energy Spectrum of Protons Trapped in the Earth's Inner Van Allen Zone", J. Geophys. Res. 68, 1811-1822 (1963).

P2-6. Bock, J. K., Ballistic Research Laboratories, Aberdeen Proving Ground, Maryland (private communication, March 1966).

P2-7. Van Allen, J. A., et al, "Radiation Observations with Satellite 1958 ", J. Geophys. Res. 64, 271-286 (1959).

A. Summary of Ph.D. Dissertation, Donald J. Manson, "Van Allen Radiation Belt and ARGUS Directional Flux Density Distributions, Explorer 4, Satellite Data"; Saint Louis University, Physics Department (February 1967).

A1. Introduction

A recent determination (Ref. A1) of the correct roll (or spin) rate for satellite Explorer 4 has allowed, for the first time, systematic and reliable determinations of directional flux density distributions of geomagnetically trapped charged particles injected by the ARGUS Event 1 of 27 August 1958. The results of the present analysis (1) indicate a pronounced and unique omnidirectional penetrating radiation effect associated only with ARGUS Event 1, (2) include a comparison of directional flux density distributions (particles $cm^{-2}sec^{-1}ster^{-1}$) of the naturally (inner Van Allen Belt) and artificially (ARGUS Event 1) injected radiation, and (3) permit determination of a decay curve for a limited time period of the measured maximum (perpendicular to $\vec{B}$) directional particle flux density of the artificially injected (ARGUS Event 1) radiation.

A2. Analysis and Experimental Details

The angle θ between the directional (scintillation Detector A, Channel 2,5) counter and a plane perpendicular to the magnetic flux density vector B is determined as a function of time by calculating the rotational (roll and tumble motion) and forward motions of the satellite in the Vernal Equinox coordinate system. Critical phase angles for the roll and tumble motions at an initial reference time

are determined by analysis of the r-f electric field strength patterns from the telemetry and by "loop closure-search" (based on the assumption that at equal angles of the counter axis relative to $\vec{B}$ the counting rates are equal; see Ref. A2 for details). Each short time-period section of count-rate data between signal fadeouts (corresponding to one-half a tumble cycle) is analysed separately. Satellite telemetry yields primarily count-rates versus time (Ref. A2) which, combined with the calculation of θ as a function of time, yields observed count-rate C_{obs} as a function of θ. Correcting for deadtime, counter efficiency and effective area (Ref. A2), and solving the integral equation (Ref. A3) relating count-rate to the directional flux and the counter response function, yields by an unfolding procedure the directional flux density $J(\theta')$ (particles $cm^{-2}sec^{-1}ster^{-1}$). With the aid of the magnetic mirror condition $J_{max}(\theta')$, (θ', angle between vector J and a plane perpendicular to $\vec{B}$), the directional particle flux density perpendicular to $\vec{B}$ is then calculated for larger values of B of the L shell on which the $J(\theta')$ vs θ' distribution data was acquired by Explorer 4.

Figure A1 demonstrates the validity of the method used to calculate θ as a function of time by indicating the consistency of all the data acquired by the directional counter for 4 minutes of trajectory in the Natural region of radiation ($L \approx 1.35$-1.44; approximately 1200 miles of satellite trajectory). It is evident that much of the observed scatter is due to decrease in the maximum count-rate as the satellite moves to increased values of B and L, and that the shape of the count-rate vs θ distribution is sensibly constant with small variations of L for the Natural radiation in this region. The relatively constant counting rate for large values of θ indicates a penetrating component of the radiation.

A3. Results

All the data acquired from the unshielded G-M counter (Detector C, Channel 3) and the directional scintillator (Detector A, Channel 2) for Passes 414 and 427 are summarized in Figs. A2 (Upper and Lower). Triangle-points for each of the two Figures are count-rate maxima (counter axis perpendicular to $\vec{B}$) determined from directional distributions such as shown by Fig. A1, dot-points are in turn the minima (counter axis parallel to $\vec{B}$); the dashes are the average count-rate from the unshielded G-M counter (detects electrons of energy greater than 3 MeV; protons, greater than 31 MeV) and the X-points are the average count-rates from the shielded (Detector D, Channel 1) omnidirectional G-M counter (detects electrons of energy greater than 6 MeV; protons, greater than 40 MeV). Decrease in maximum count-rate with increasing B and L (Fig. A2) is evident for the Natural radiation (to the "left" of the arrows along the time axes); clearly visible is ARGUS Event 1 at L = 1.62 - L = 1.76. For Pass 414 a core of penetrating radiation is indicated (between arrows along time axes) at L = 1.71 to 1.76, 1.8 hrs following the nuclear event; this directional penetrating component is not observed 24 hrs later (Pass 427). Comparison of Passes 414 and 427 indicates essential constancy of the Natural radiation but rapid decay of the ARGUS shell within a 24-hour period, and also indicates a change in energy distribution suggested by a difference in ratios (of the penetrating component of the directional scintillator count-rates to the average count-rates of the omnidirectional unshielded G-M counter) for the same 24-hour period.

Figure A3 indicates a comparison of the directional flux density distribution, $J(\theta')$ vs θ'; for the Natural (left-hand plot), and the ARGUS Event 1 radiation (right-hand plot) of 28 August 1958, 25.48 hrs following the event.

A4. Short-lived Penetrating Radiation Phenomena Possibly Related to Geomagnetically Trapped Debris

This section contains a revised (relative to our Final Report, DASA Report 1613, 15 January 1965) interpretation of the penetrating radiations observed during Pass 414 (over Huntsville) of Explorer 4. Hence Figs. A4, 5, 6 from Report 1613 are reproduced in the present section.

Figures A4, A5, and A6 are the result of detailed directional analysis of the data acquired from the region indicated by the arrows on time axis (Fig. A2, Upper) where the penetrating radiation mentioned in A3 above was observed. The method of treating each limited portion of telemetry data between signal fadeouts allows plotting of the count-rate, vs time and θ, during each fractional part of a rotation of the scintillator counter axis with respect to $\vec{B}$. As indicated by Fig. A1 this method yields a consistent disk-like shape for the Natural radiation with all data clustering around one curve.

Figures A4, A5, and A6 indicate considerable departure of the ARGUS Event 1 radiation, 1.8 hrs after the event, from the disk-like shape of the Natural radiation and so each partial rotation of the counter axis with respect to $\vec{B}$ has been plotted separately except for Fig. A4 (b,c,d) where three such rotations (from the early penetration of the ARGUS shell have been superimposed to yield a count-rate vs θ distribution much like that for the Natural radiation).

In Fig. A4(f) the time sequence shown by the arrows indicates that the average count-rate is increasing rapidly during one partial rotation (approx. 3.6 secs) so that at equal angles of the counter axis with respect to $\vec{B}$ (e.g., $\theta \simeq 60$ deg) two different count-rates

are observed, the later count-rate having increased as the satellite penetrated farther into the ARGUS shell. It should be noted that the omnidirectional penetrating component (at large θ values) has increased rapidly (from 2000counts sec^{-1} in Fig. A4(b,c,d) to approximately 5000 counts sec^{-1} in Fig. A4(f).) The large count-rate (9000 sec^{-1}, θ = 52 deg, Fig. A4(f)), at larger angles of θ indicates a departure from the disk-like shape of the radiation. Figure A4(g) indicates that the scintillation counter is saturating (count-rate, greater than 10,000 sec^{-1}) when perpendicular to $\vec{B}$ (θ = 0) while the count-rate at θ = 50 deg has dropped (from 9000 to 7000 sec^{-1}). Figure A4(h) indicates saturation at small to moderate θ angles ($\geq$ 10,000 sec^{-1}, $\theta \leq$ 40 deg) and a count-rate of almost 7000 sec^{-1} at θ = 60 degrees - again a considerable departure from disk-like shape of the count-rate vs θ distribution.

Figure A5(j) (acquired 2.5 secs later than Fig. A4(h)) indicates a more normal disk-like shape but for a limited range around θ = 0. Figures A5(j,k,l and m) if superimposed would yield a single consistent distribution much like Fig. A5(m) where the C_{obs} vs θ distribution is disk-like ($\theta \leq$ 30 deg) but with a large omnidirectional penetrating background component ($>$ 5000 sec^{-1}). The final 5 points of the time sequence (arrows) shown in Fig. A5(m) indicate a sudden saturation of the counter ($\theta \leq$ 30 deg).

This saturation is continued in Fig. A6(n) at θ = 30-35 degrees but is followed in Figs. A6(o) by an abrupt change to a more nearly disk-like distribution; followed immediately in turn by saturation for all angles $\theta \leq$ 40 deg. Figure A6(p) (0.2 sec later) indicates a return to the normal disk-like shape followed by a sharp drop in the

count-rate at $\theta = 0$ as the satellite leaves the ARGUS shell. Figure A4(q) is for the last measurable count-rates from the ARGUS Event 1 wing as the satellite moves into the slot between the two Van Allen belts away from the ARGUS shell.

The analysis presented relative to Figs. A4, 5, 6 suggests that the data from Pass 414, 1.8 hrs after Event 1 contains evidence for short term penetrating components (directional and omnidirectional) of the radiation which are neither spatially homogenous nor isotropic. The fact that the scintillation counter goes to saturation suddenly during one portion of the rotation of the counter axis with respect to vector B as in Fig. A5(m) and A6(o) while the remaining portion of the rotation measures a fairly normal distribution suggests a varying directional component of the flux at these points (possibly due to gamma radiation from trapped debris near the ARGUS shell). The normal disk-like distributions (Fig. A3) measured in the ARGUS shell 1 day later for Pass 427 apparently are present in Pass 414 but are obscured and distorted by the large penetrating omnidirectional component and bursts of directional radiation which saturate the counter. These effects are greatly diminished in Pass 415, (3.67 hrs following Event 1) and are not found in Pass 427 (25.48 hrs following Event 1).

No such effects were found from ARGUS Event 2 where data from Pass 454 (1.87 hrs following Event 2, 30 August 1958; Refs. A2, A4) indicate the usual disk-like distributions.

Figure A7 indicates the time decay of maximum directional flux density $J_{max}(\theta')$ for two days following ARGUS Event 1. It was not possible to follow the decay for a longer period than two days because by the third day the directional trapped radiation intensity has diminished to near background value.

The x-points lie well on a straight line (exponential decay law), the solid-line curve is a plot of the $t^{-1.13}$ law (observed for the omnidirectional radiation, see Part C of the present report) for comparison. Because of the short time interval represented, about 2 days, a decision between the two decay laws is not considered valid.

Figure A8 is a 3-dimensional plot of $J_{max}(\theta')$, the directional flux density perpendicular to $\vec{B}$, vs B and L; both Natural and ARGUS Events 1 and 2 radiations are shown. Figure A8 summarizes most of the data analysed for the scintillation counter, Detector A.

A5. Conclusions

Detailed analysis of ARGUS directional flux density distributions from Explorer 4 data (Passes 414 and 427, over Huntsville, Alabama, on 27 and 28 August 1958 respectively) for 1.8 and 25.48 hrs respectively after Event 1 and comparison with Natural flux density distributions indicate that the disk-like shape as measured by the scintillation counter in the ARGUS shell is not substantially different from the Natural radiation (by Fig. A3, the half-width at half-maximum (hwhm) is 7 deg broader on the average for the ARGUS $J(\theta')$ compared to the Natural radiation; maximum values of directional flux densities are 12×10^7 for the Natural vs 6.7×10^7 $cm^{-2}sec^{-1}ster^{-1}$ for ARGUS). The 27 August 1958 data from Pass 414 (Ref. A2) and Pass 415 (Ref. A3) indicate that these measured distributions are temporarily obscured and distorted by a large penetrating omnidirectional component and a varying directional component. The short-time limited decay data suggest an exponential decay of maximum directional flux density at L = 1.7 but a $t^{-1.13}$ law observed for the omnidirectional data from

G-M counter (Detector C) is not excluded. It may be suggested that particle and energy differences between Natural and ARGUS radiations can be expected to yield somewhat different decay laws.

A6. References

A1. Bock, J. K., Delaney, R. M., Manson, D. J., "Explorer 4 (1958 Epsilon) Spin Rate Correction", Transactions American Geophysical Union, April 1966.

A2. "Van Allen Radiation Belt and ARGUS Directional Flux Density Distributions, Explorer 4 Satellite Data", Ph.D. Dissertation, D. J. Manson, Saint Louis University, Physics Department, 1 July 1966.

A3. "Interpretations of Directional Flux Densities in ARGUS Shells, Explorer 4 Satellite Data", Ph.D. Dissertation, J. M. Paikeday, Saint Louis University, Physics Department, 1 June 1966.

A4. "Van Allen Radiation Belt and ARGUS Directional Flux Density Distributions, Explorer 4 Satellite Data, ARGUS Event 2", M.S. Thesis. J. F. Fennell, Saint Louis University, Physics Department, 8 July 1966.

A5. Lundquist, C. A., Naumann, R. J., and Weber, A. H., "Directional Flux Densities and Mirror Point Distributions of Trapped Particles from Satellite 1958 Epsilon Measurements", J. Geophys. Res. 67, 4125-4133 (1962).

A6. Van Allen, J. A., McIlwain, C. E., and Ludwig, G. H., "Radiation Observation with Satellite 1958€ ", J. Geophys. Res. 64, 271-286 (1959).

A7. Baicy, E. O., Bock, J., and Jeter, T. R., "The ARGUS Experiment Calibration of Explorer IV Prototype", Defense Atomic Support Agency Report WT-1671, Ballistic Research Lab., Aberdeen, Maryland (1963).

Fig. A1. Pass 427 (over Huntsville, Alabama, 28 August 1958) observed directional count-rate C_{obs} vs θ for 4 min in the region of Natural radiation.

o, C_{obs} vs θ; 227.5 - 229.5 min UT; L, 1.35 - 1.42 earth radii; B, 0.145 - 0.164 gauss; ^, C_{obs} vs θ; 229.5 - 231.5 min UT; L, 1.42 - 1.49 earth radii; B, 0.164 - .180 gauss.

Data were plotted by combining about one-half of the 100 individual sections of C_{obs} vs θ described in Ref. A2, Sec. 3.3. All data acquired within the time period 227.5 - 231.5 UT are plotted to show the amount of scatter in the data and to demonstrate the consistency of the analytic interpretation using the experimentally determined parameters: roll and tumble phase angles δ and γ, and the roll and tumble rates.

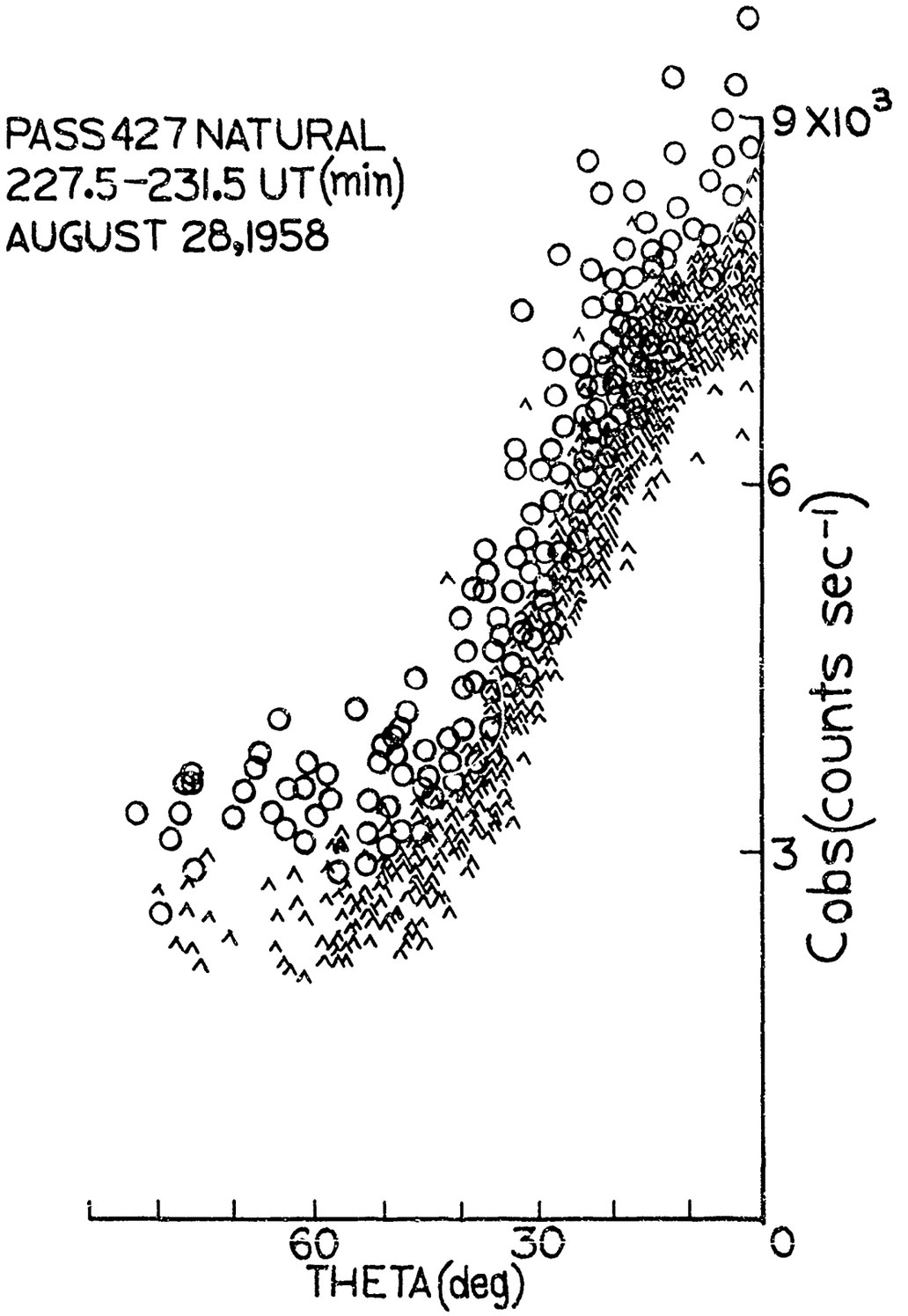
PASS 427 NATURAL
227.5-231.5 UT (min)
AUGUST 28, 1958
9 X 10³
6
3
0
Cobs (counts sec⁻¹)
60
30
THETA (deg)

Fig. A2. (Upper, Lower)

Natural and ARGUS Event 1 count-rates vs time and B-L coordinates for Passes 414 and 427 over Huntsville, Alabama. Comparison of Average Omnidirectional Count-Rate with Maximum (perpendicular to $\vec{B}$) and Minimum (parallel to $\vec{B}$) Directional Counting Rates.

Triangle-points, maxima; and dot-points, minima, scintillation counter (Detector A) observed count-rates;

Dash-points, 15-sec averages of observed omnidirectional (unshielded G-M counter, Detector C) count-rates;

X-points, 6-sec averages of observed omnidirectional count-rates (shielded G-M counter, Detector D).

Arrows on the time axis indicate time region in which distributions of Figs. A4, 5, and 6 (Pass 414) were acquired (ARGUS Event 1). Calibration information for the three counters is summarized in the Preface (P1) of the present report.

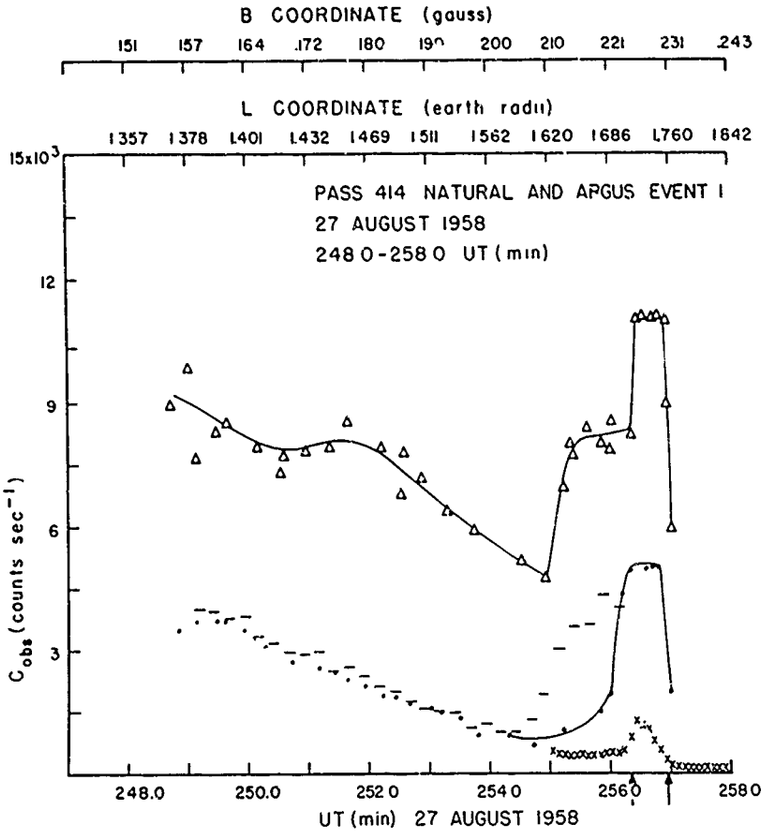
B COORDINATE (gauss)
151 157 164 172 180 190 200 210 221 231 243
L COORDINATE (earth radii)
1357 1378 1401 1432 1469 1511 1562 1620 1686 1760 1842
15x10^3
12
9
6
3
C_obs (counts sec^-1)
PASS 414 NATURAL AND ARGUS EVENT I
27 AUGUST 1958
2480-2580 UT (min)
248.0 250.0 252.0 254.0 256.0 258.0
UT (min) 27 AUGUST 1958

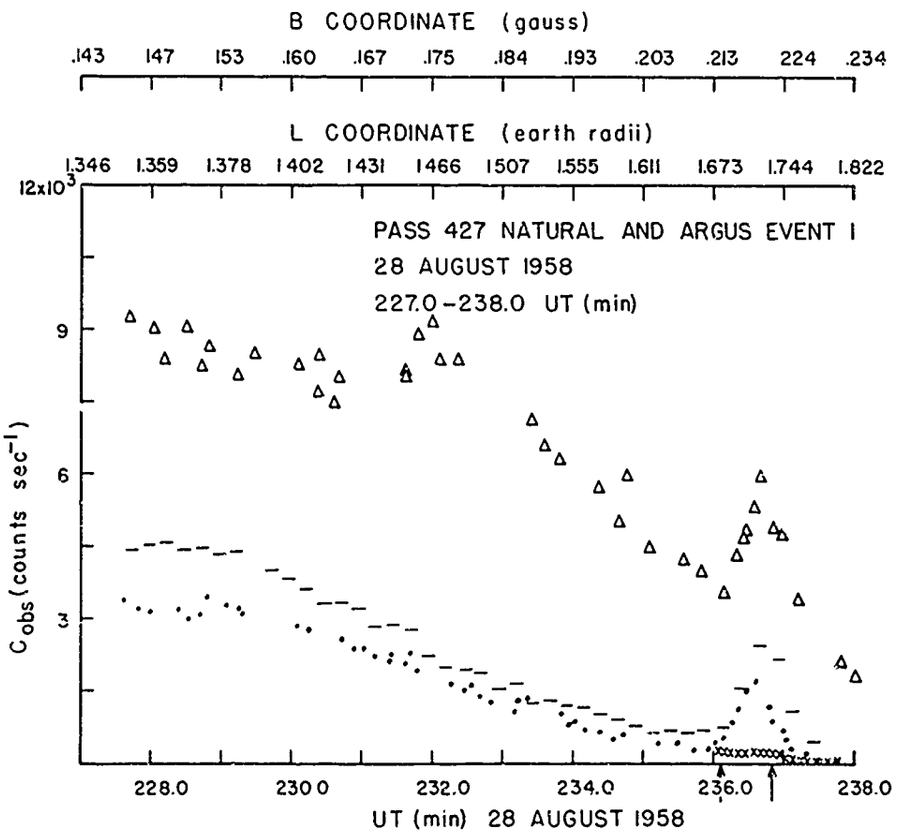
B COORDINATE (gauss)
.143 147 153 160 167 175 184 193 203 213 224 234
L COORDINATE (earth radii)
1.346 1.359 1.378 1.402 1.431 1.466 1.507 1.555 1.611 1.673 1.744 1.822
12x10^3
9
6
C_obs (counts sec^-1)
PASS 427 NATURAL AND ARGUS EVENT I
28 AUGUST 1958
227.0-238.0 UT (min)
228.0 230.0 232.0 234.0 236.0 238.0
UT (min) 28 AUGUST 1958

Fig. A3. Directional flux density distributions $J(\theta')$ vs θ for Pass 427, 28 August 1958; Natural (left-hand plot) and ARGUS Event 1 (right-hand plot) radiations. Variations of magnitudes of $J_{max}(\theta') = J(0)$ and shape of the distributions are shown. $J(\theta')$ for ARGUS Event 1 radiation were corrected for varying penetrating radiation component as explained in Ref. A2.

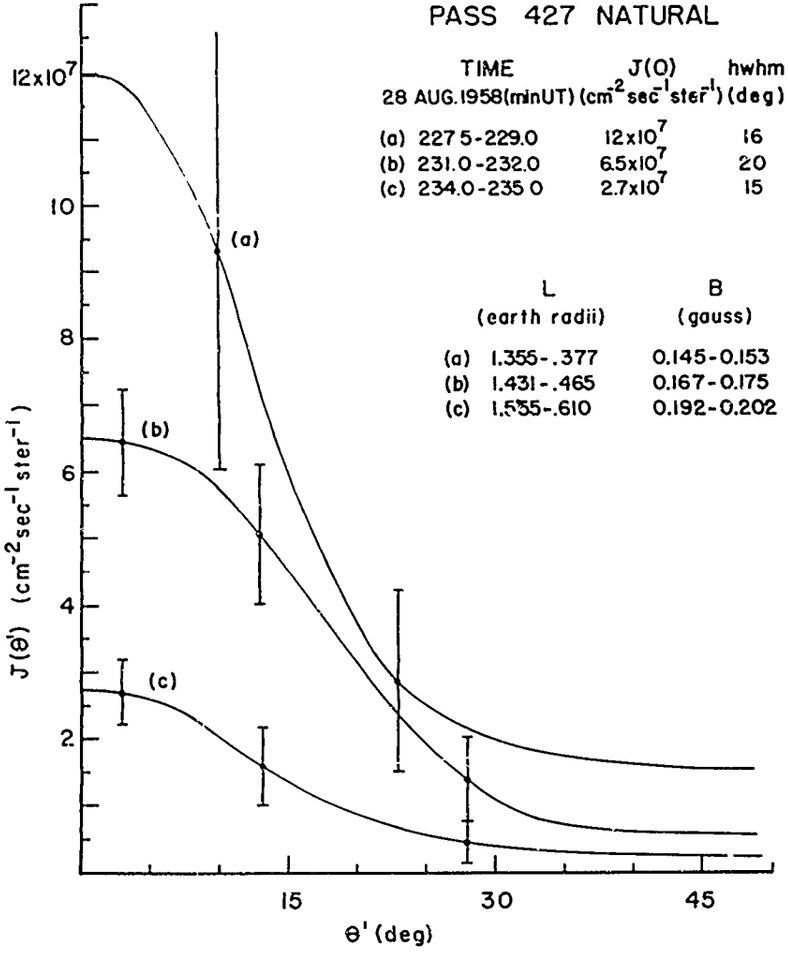
PASS 427 NATURAL
TIME
28 AUG. 1958 (min UT)
J(0) (cm⁻² sec⁻¹ ster⁻¹)
hwhm (deg)
(a) 227 5-229.0 12x10⁷ 16
(b) 231.0-232.0 6.5x10⁷ 20
(c) 234.0-235 0 2.7x10⁷ 15
L (earth radii)
B (gauss)
(a) 1.355-.377 0.145-0.153
(b) 1.431-.465 0.167-0.175
(c) 1.555-.610 0.192-0.202
12x10⁷
10
8
6
4
2
J(θ') (cm⁻² sec⁻¹ ster⁻¹)
15
30
45
θ' (deg)

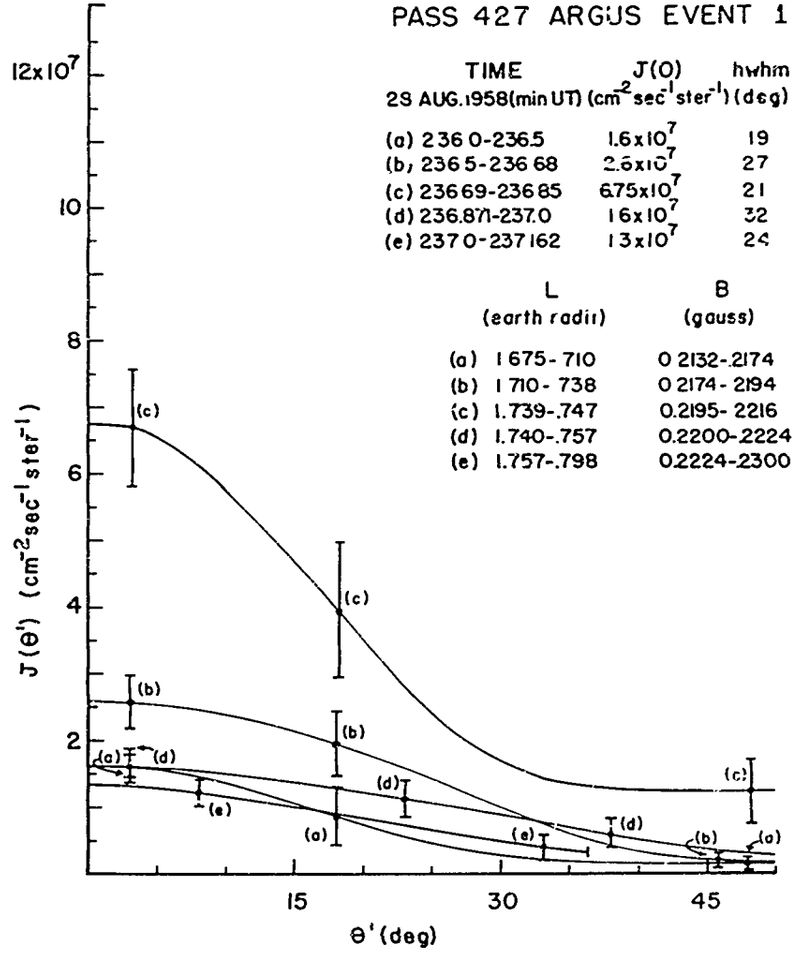
PASS 427 ARGUS EVENT 1
TIME
28 AUG. 1958 (min UT)
J(0) (cm⁻² sec⁻¹ ster⁻¹)
hwhm (deg)
(a) 236 0-236.5 1.6x10⁷ 19
(b) 236 5-236 68 2.6x10⁷ 27
(c) 236 69-236 85 6.75x10⁷ 21
(d) 236.871-237.0 1 6x10⁷ 32
(e) 237 0-237 162 1 3x10⁷ 24
L (earth radii)
B (gauss)
(a) 1 675-710 0 2132-.2174
(b) 1 710-738 0 2174-2194
(c) 1.739-.747 0.2195-2216
(d) 1.740-.757 0.2200-2224
(e) 1.757-.798 0.2224-2300
12x10⁷
10
8
6
4
2
J(θ') (cm⁻² sec⁻¹ ster⁻¹)
15
30
45
θ' (deg)

Figs. A4, A5, and A6

Detailed sequence of scintillation counter count-rates C_{obs} vs θ (angle between scintillation counter axis and the plane perpendicular to $\vec{B}$) for Pass 414 ARGUS Event 1 penetration, 27 August 1958. Where used arrows indicate time sequence in acquisition of points. Distributions indicate a large omnidirectional penetrating component and a varying directional component of the radiation (discussed in detail in the text).

ARGUS EVENT 1

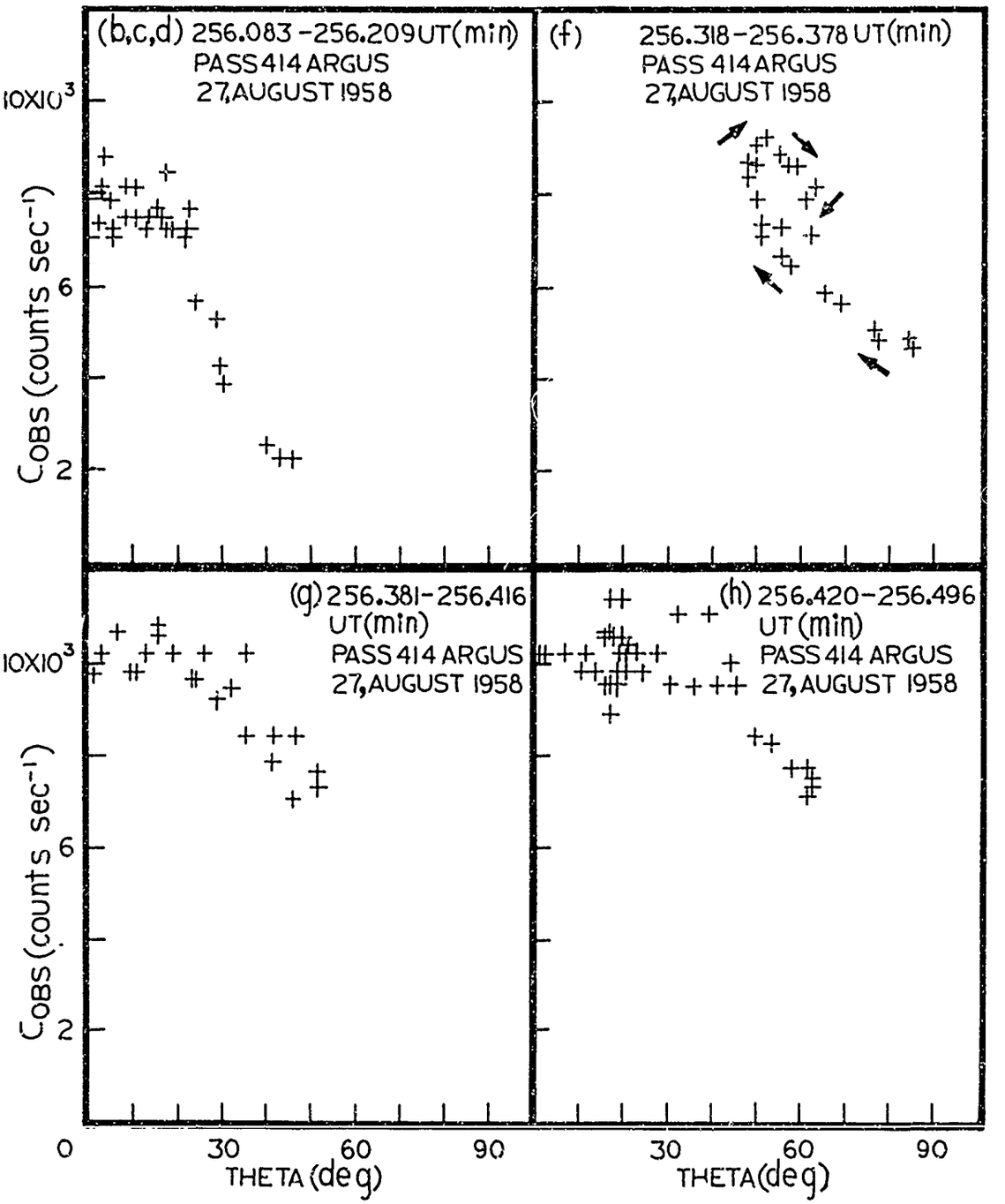

ARGUS EVENT 1

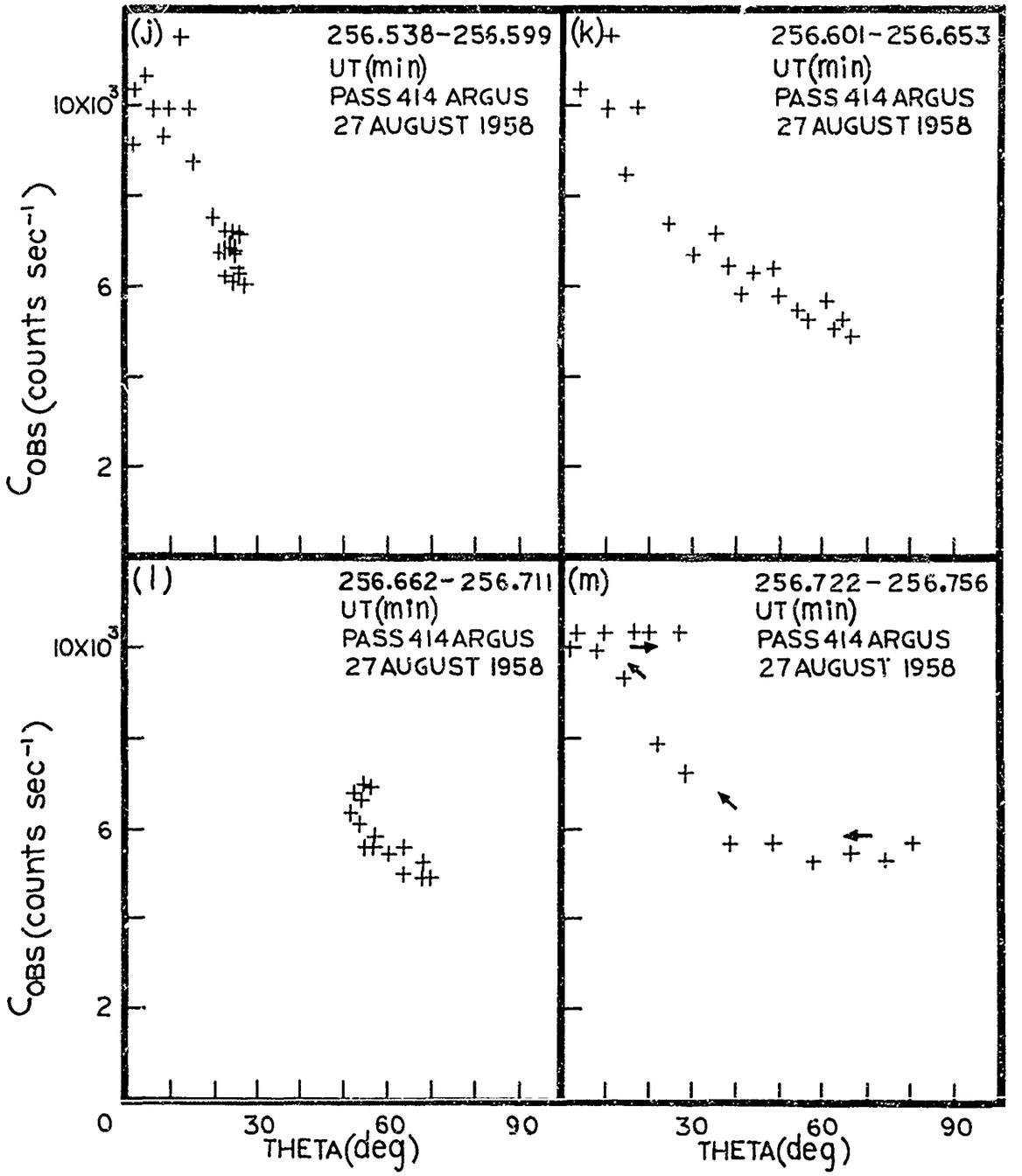

ARGUS EVENT 1

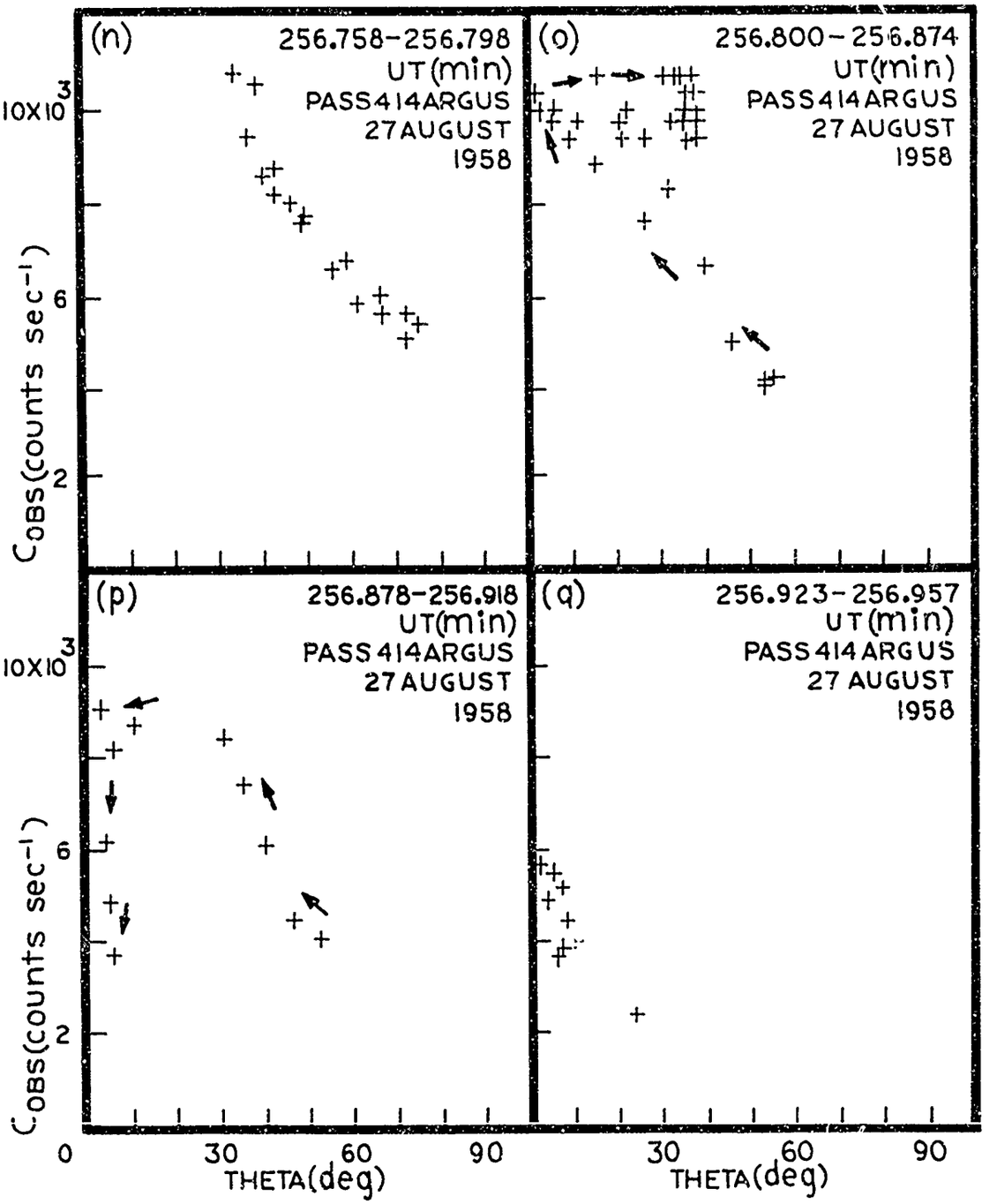

Fig. A7. Decay of maximum directional particle flux densities $J_{max}(\theta')$ vs time for ARGUS Event 1. Plotted points are for flux density distributions $J(\theta')$ at $\theta' = 0$. The maximum ARGUS Event 1 radiation is observed to decay one order of magnitude in 45 hrs. The lower curve is a plot of the $t^{-1.13}$ law (observed for the omnidirectional radiation, Part C of the present report, for the same ARGUS Event 1 radiation).

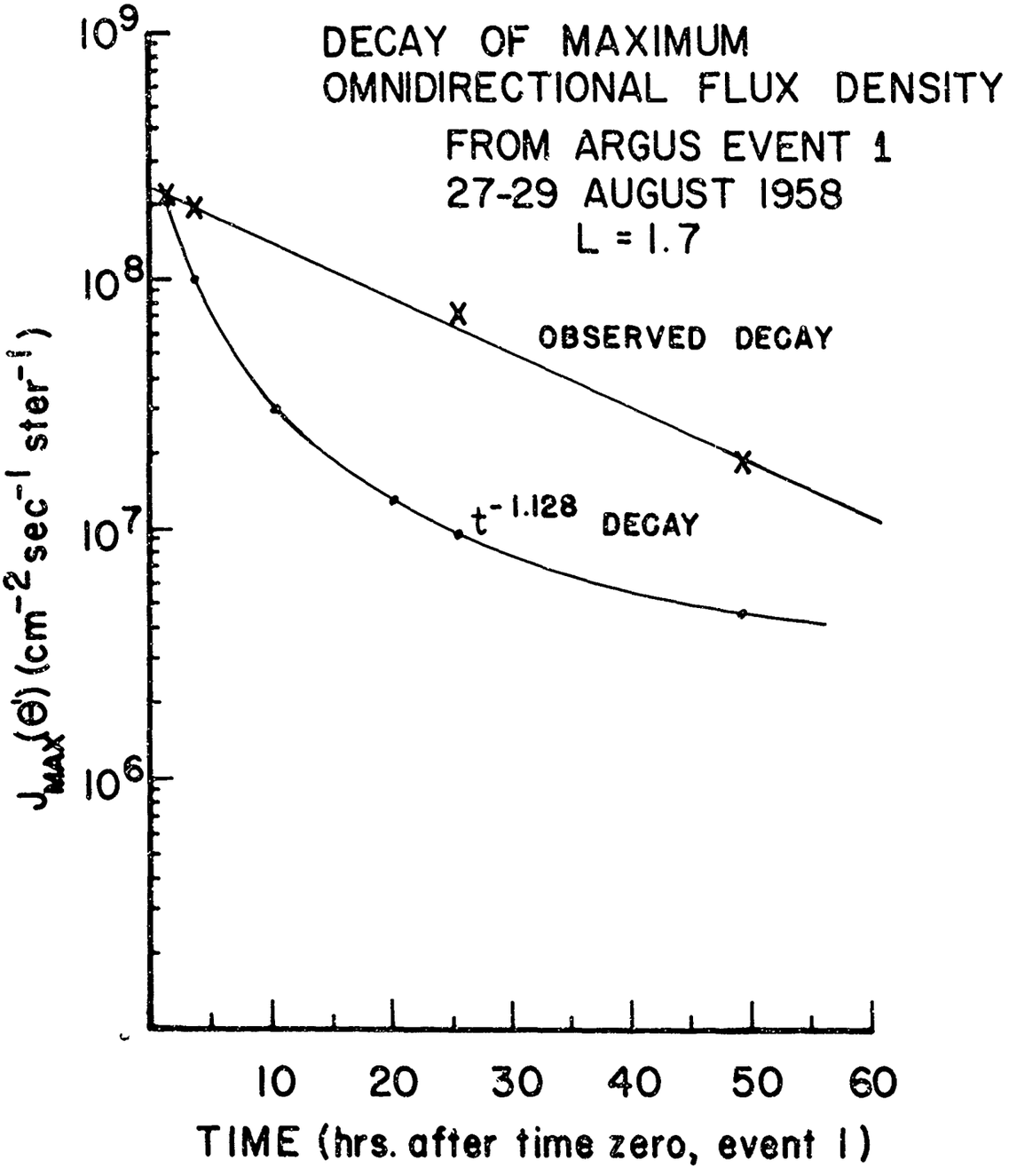
DECAY OF MAXIMUM
OMNIDIRECTIONAL FLUX DENSITY
FROM ARGUS EVENT 1
27-29 AUGUST 1958
L = 1.7
OBSERVED DECAY
$t^{-1.128}$ DECAY
10^9
10^8
10^7
10^6
$J_{MAX}(\theta')$ (cm^{-2} sec^{-1} ster^{-1})
10
20
30
40
50
60
TIME (hrs. after time zero, event 1)

Fig. A8. Directional maximum particle flux density $J_{max}(\theta')$ vs B and L for both Natural and ARGUS Events 1 and 2 radiations (Detector A, Channel 2)

Detailed information is tabulated as follows.

Natural Radiation

	L (earth radii)	Slope	Pass No.	Date
α	1.360	-7.92	427	28 Aug. 1958
β	1.380	-4.82	414	27 Aug. 1958
γ	1.407	-7.15	427	28 Aug. 1958
δ	1.409	-2.76	414	27 Aug. 1958
ϵ	1.434	-7.15	454	30 Aug. 1958
ζ	1.458	-7.15	454	30 Aug. 1958
η	1.580	-7.92	427	28 Aug. 1958

ARGUS EVENT 1

θ	1.690	-3.78	414	27 Aug. 1958
ι	1.694	-6.42	427	28 Aug. 1958
κ	1.724	-4.10	427	28 Aug. 1958
μ	1.728	-4.11	440	29 Aug. 1958
ν	1.730	-3.58	415	27 Aug. 1958
ξ	1.743	-5.05	427	28 Aug. 1958
o	1.748	-2.00	427	28 Aug. 1958
λ	1.777	-4.48	427	28 Aug. 1958

ARGUS EVENT 2

π	2.124	-7.55	454	30 Aug. 1958
ρ	2.124	-3.60	454	30 Aug. 1958
σ	2.144	-15.40	454	30 Aug. 1958
τ	2.172	-10.40	454	30 Aug. 1958

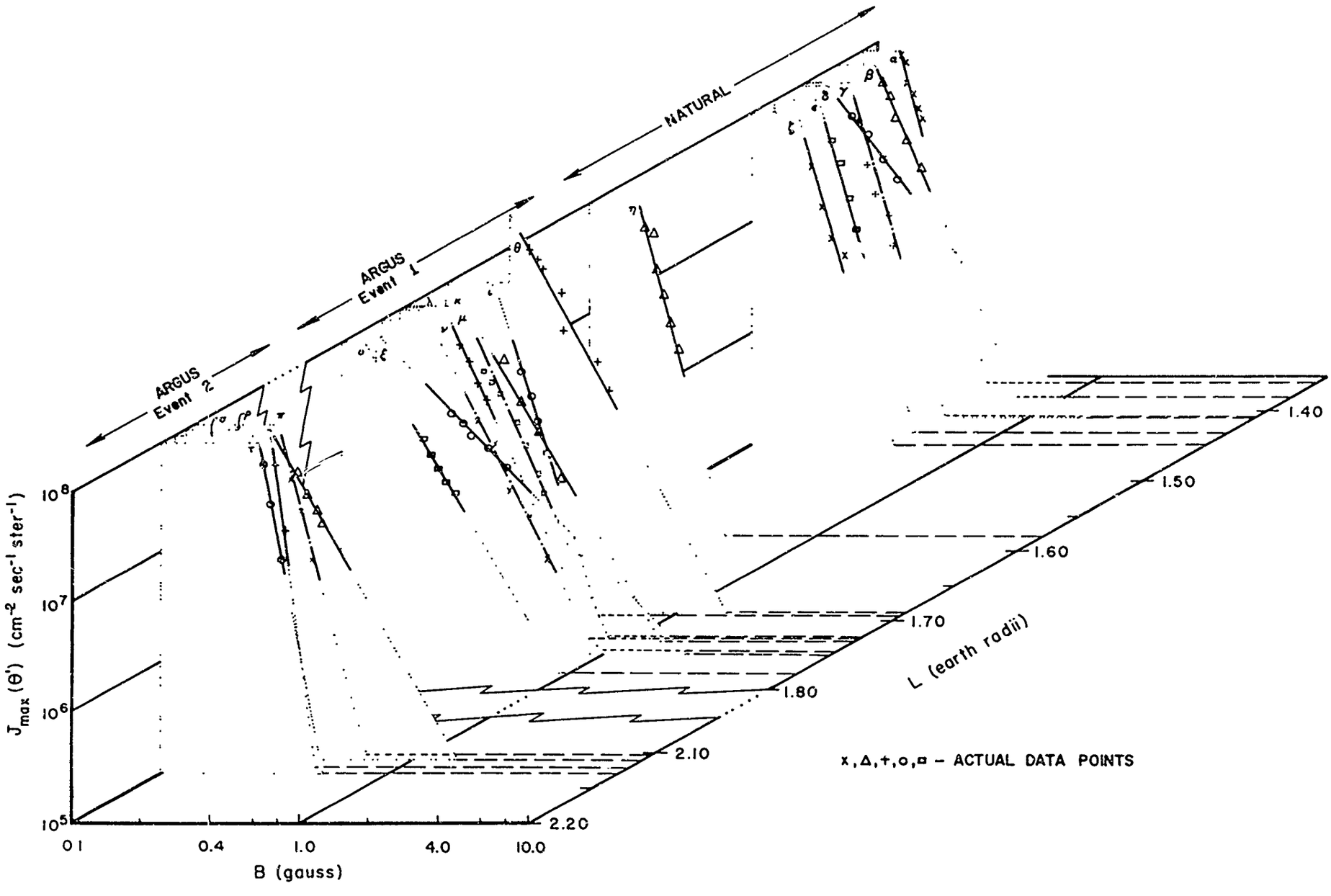
NATURAL
ARGUS
Event 1
ARGUS
Event 2
$J_{max}(\theta')$ (cm^{-2} sec^{-1} ster^{-1})
10^8
10^7
10^6
10^5
0.1
0.4
1.0
4.0
10.0
B (gauss)
1.40
1.50
1.60
1.70
1.80
2.10
2.20
L (earth radii)
x, Δ, +, o, □ – ACTUAL DATA POINTS

B. Summary of M.S. Thesis of Joseph P. Fennell, "Van Allen Belt and ARGUS Directional Flux Density Distributions, Explorer 4 Satellite Data, ARGUS Event 2", Saint Louis University, Physics Department (July 1966).

B1. Introduction

This Thesis, Reference B1, contains essentially an analysis of the directional distribution of flux densities (particles $cm^{-2}sec^{-1}ster^{-1}$) vs the angle between the counter symmetry axis and the plane perpendicular to the magnetic flux density vector. of geomagnetically trapped naturally occurring and artificially injected charged particles associated with ARGUS Event 2 for Pass 454 over Huntsville, Alabama (for a time interval of about 10 min. beginning 1.8 hrs following the Event). The purpose of this limited analysis was to compare the situation with that of Pass 414 (Manson Dissertation, Ref. B2) with the Passes occurring approximately 3 days apart. The count-rate data were obtained from a scintillation photomultiplier detector (Detector A, Channel 2 Ref. B2); window aperture, 15 degrees half-width at half-maximum; $A_{eff}\epsilon$, 0026 cm^2; deadtime 100 microsecs aboard Satellite Explorer 4.

The thesis represents the first detailed examination of the directional data for ARGUS Event 2 by the Saint Louis University group. There is presented a short discussion of a method for determining the proper roll phase angle used in this analysis and the results from determinations of satellite roll frequencies for times at which they had not been previously determined with sufficient precision to yield reliable determinations of observed count-rate $C_{obs}(\theta)$ vs angle θ (between the counter symmetry axis and a plane perpendicular to the magnetic flux density vector B).

B2. Determination of the Phase Angle for the Roll Motion of Satellite

To determine the directional flux density $J(\theta')$ vs angle θ' between the counter axis and the incident flux direction, $C_{obs}(\theta)$ as a function of θ must be known. θ at time t (relative to an arbitrary reference time) is given by

$$\theta = \text{Arcsin}[\, b_1 \sin(\dot{\psi}t + \delta) - b_2 \cos(\dot{\psi}t + \delta) \sin(\dot{\phi}t + \gamma) + b_3 \cos(\dot{\psi}t + \delta) \cos(\dot{\phi}t + \gamma)\,], \quad \text{(B1)}$$

where all parameters are known explicitly except δ and γ, the roll and tumble motion phase angles. γ was determined as

$$\gamma = \text{Arccos}\ (\hat{A} \cdot \hat{Y}_s), \quad \text{(B2)}$$

where A is the satellite symmetry axis vector and Y_s is a unit vector in Vernal Equinox Coordinates (Ref. B2).

δ is determined (Ref. B1) in Eq. (B1) by assuming counting rates are equal approximately at equal angles θ in the Natural radiation region (over short periods of time, $t \leq 0.5$ min). Taking two times t_i, t_j with equal counting rates, it can be shown (Ref. B1) from Eq. (B1) that

$$\delta_{ij} = \text{Arctan}\,(-f_{ij}/g_{ij}) \quad \text{(B3)}$$

where $f_{ij} = f_i + f_j$, $g_{ij} = g_i + g_j$,

$f_i = b_1(t_i) \sin(\dot{\psi} t_i) + F(t_i, \gamma) \cos(\dot{\psi} t_i)$,

$g_i = b_1(t_i) \cos(\dot{\psi} t_i) - F(t_i, \gamma) \sin(\dot{\psi} t_i)$

and $F(t_i, \gamma) = b_3(t_i) \cos(\dot{\phi} t_i + \gamma) - b_2(t_i) \sin(\dot{\phi} t_i + \gamma)$.

An average δ is then determined by considering

$$\delta_{avg} = Arctan\left(-\frac{\sum(f_{ij}/g_{ij})}{N}\right) \qquad (B4)$$

where the sum is over N time pairs t_i, t_j. The consistency of the data can be seen by considering the variations in the δ_{ij} from δ avg. If the spread in the values of δ_{ij} is small the random fluctuations in the data are small. δ_{avg} was determined (with respect to an arbitrary reference time) as 94° for Pass 454 and this value reproduced the count-rate variations in a simulator program (see Ref. B2).

The roll rate for Explorer 4 was determined for the entire telemetry times of Passes 414 through 454 by fitting a least square polynomial to the known roll rate values at discrete reference times of Passes 414, 415, 427, and 454. A second method for determining the roll rate, based on the fact that Sin θ is a minimum when $C_{obs}(\theta)$ is maximum is presented by Fennell (Ref. B1). (The second method was applied to Pass 440 and the resulting roll rate was used by J. M. Paikeday (Ref. B3) to obtain a directional flux density distribution for Pass 440 ARGUS Event 1 radiation.)

B3. Results

With θ determined as a function of time, plots $C_{obs}(\theta)$ vs θ are made and then corrected for the counter deadtime and (effective area x counter efficiency) to yield the true count-rate $C(\theta)$

$$C(\theta) = \frac{C_{obs}(\theta)}{\epsilon A_{eff}\left(1 - \tau_D C_{obs}(\theta)\right)}. \qquad (B5)$$

The corrected or true count-rates $C(\theta)$ are used to compute the corresponding directional flux densities $J(\theta')$ as described by J. M. Paikeday (Ref. B3). Representative examples of the observed count-rates $C_{obs}(\theta)$ vs θ, true count-rates $C(\theta)$ vs θ, and directional flux densities $J(\theta')$ vs θ', for Pass 454 Natural radiation are shown by Figs. B1 and B2. The $C_{obs}(\theta)$ vs θ curves showed an "open loop" phenomena (see Fig. B3(a)) which is due in part to the rapid rate of change of both the omnidirectional and directional components of the radiation as the satellite moves through the ARGUS Event 2 shell. The curve was reduced to a single valued curve by subtracting out this component (compare Fig. B3(a) and $C_{obs}(\theta)$) of Fig. B3(c)). The resulting $C_{obs}(\theta)$ vs θ, $C(\theta)$ and $J(\theta')$ vs θ, θ' curves for the ARGUS radiation are shown in Figs. B3,4. Figures B1,2,3,4 and Tables B1, B2 in the Figs. B2, B4 captions represent the results of this analysis.

B4. Conclusions

The maximum directional flux density and observed count-rate vary considerably in the six minutes of the Natural radiation observed for Pass 454 while the half-width at half-maximum (hwhm) remains relatively constant at 17 ± 5 degrees (see Table B1, Fig. B2 caption). The variation in maximum count-rate and flux density is probably related to the large spatial and magnetic flux density changes involved in the satellite motion.

The non-zero $J(\theta')$ for $\theta' \geq 50$ to 60 degrees (Fig. B2), in the Natural radiation region is due probably to penetrating (independent of θ') radiation capable of transmission by the counter shielding ($E_e \geq 3$ Mev); it is the background count-rate for the detector in the region of Natural radiation.

The flux densities and hwhm vary considerably for the ARGUS Event 2 Pass 454 radiation. By Fig. B4 the ARGUS radiation appears generally to have a smaller hwhm (16° vs 18°) and a larger maximum flux density (6.4×10^7 vs 4.9×10^7 particles $cm^{-2}sec^{-1}ster^{-1}$) than the Pass 454 Natural radiation. It is noted that there are large differences in B and L coordinates between the Natural and ARGUS radiations. The results for Pass 454 are included in Table B2 for comparison with previous analysis (Refs. B2, B3, B4, B5).

The maximum flux intensity and hwhm of the Pass 454 ARGUS Event 2 are considerably lower (6.4×10^7 vs 2.3×10^8 particles $cm^{-2}sec^{-1}ster^{-1}$) and narrower (16° vs 24°) respectively than those of Pass 414 for ARGUS Event 1 with both Passes occurring about 1.8 hours after their respective events. Assuming both nuclear devices were the same, the differences in Pass 414 and Pass 454 ARGUS results may be due to spatial or geomagnetic effects. The data occurred at the two L's, 1.72 (Event 1) and 2.1 (Event 2).

Some tentative conclusions can be offered for Pass 454 Event 2, as follows:

(1) ARGUS radiation is more intense than the Natural as is evidenced from the Tables B1 and B2 (see Figs. B1, B4 captions).

(2) ARGUS radiation appears to be slightly more disk-like than Natural as is evidenced from the hwhm (Tables B1, B2, B3).

(3) ARGUS radiation showed no sign of any rapidly varying omnidirectional penetrating radiation effect as was observed by Manson (Ref. B2) in Pass 414

Since Pass 454 is the only ARGUS Event 2 directional data which has been analyzed by the methods presented in Refs. B1 and B2 to date, a more intensive study of Event 2 data and a more complete comparison with Event 1 directional data must await the analysis of more Event 2 directional data.

B5. References

B1. Fennell, J. F., "Van Allen Radiation Belt and ARGUS Directional Flux Density Distributions, Explorer 4 Satellite Data, ARGUS Event 2", M.S. Thesis, Physics Department, Saint Louis University, St. Louis, Missouri (1966).

B2. Manson, D. J., "Van Allen Radiation Belt and ARGUS Directional Flux Density Distributions, Explorer 4 Satellite Data", Ph.D. Dissertation, Physics Department, Saint Louis University, St. Louis, Missouri (1966).

B3. Paikeday, J. M., "Interpretation of Directional Flux Densities in ARGUS Shells, Explorer 4 Satellite Data", Ph.D. Dissertation, Physics Department, Saint Louis University, St. Louis, Missouri (1966).

B4. Bock, J. K., "Directional Dependency of Trapped Radiation After the First Nuclear High Altitude Detonation (ARGUS) as Measured by Explorer 4 (1958 Epsilon)", Preliminary Version of Final Report 1672, Defense Atomic Support Agency, Ballistic Research Laboratory, Aberdeen, Maryland (1964).

B5. Lundquist, C., Naumann, R., and Weber, A. H., "Directional Flux Densities and Mirror Point Distributions of Trapped Particles from Satellite 1958 Epsilon Measurement", J. Geophys. Res. 67, 11, 4125-4133 (1962).

Fig. B1. Representative $C_{obs}(\theta)$ vs θ curves for Pass 454 Natural radiation. Actual data points are shown to indicate the scatter in $C_{obs}(\theta)$ vs θ.

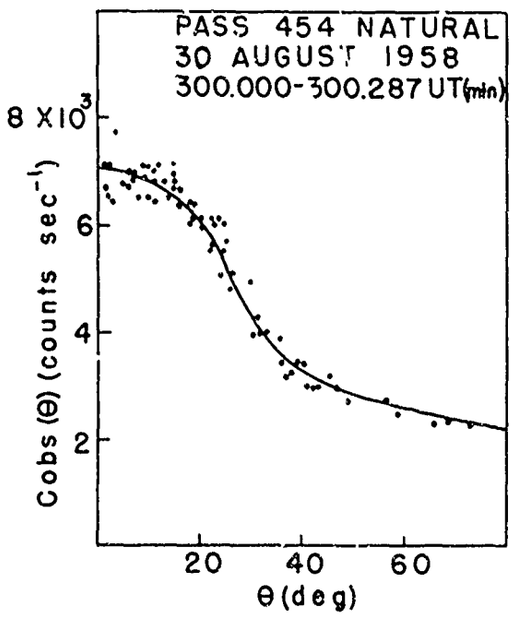
PASS 454 NATURAL
30 AUGUST 1958
300.000-300.287 UT(min)
8 X10³
6
4
2
Cobs (θ) (counts sec⁻¹)
20
40
60
θ(deg)

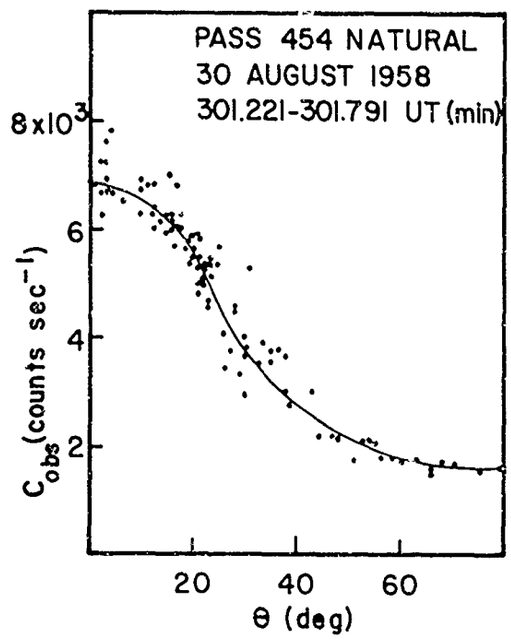
PASS 454 NATURAL
30 AUGUST 1958
301.221-301.791 UT (min)
8x10³
6
4
2
Cobs (counts sec⁻¹)
20
40
60
θ (deg)

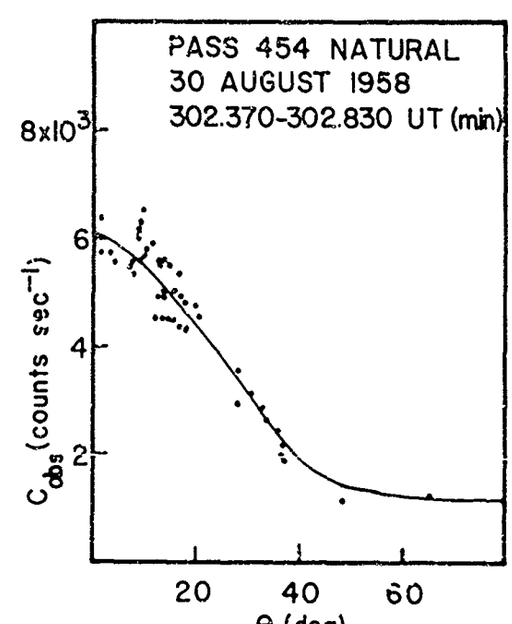
PASS 454 NATURAL
30 AUGUST 1958
302.370-302.830 UT (min)
8x10³
6
4
2
Cobs (counts sec⁻¹)
20
40
60
θ (deg)

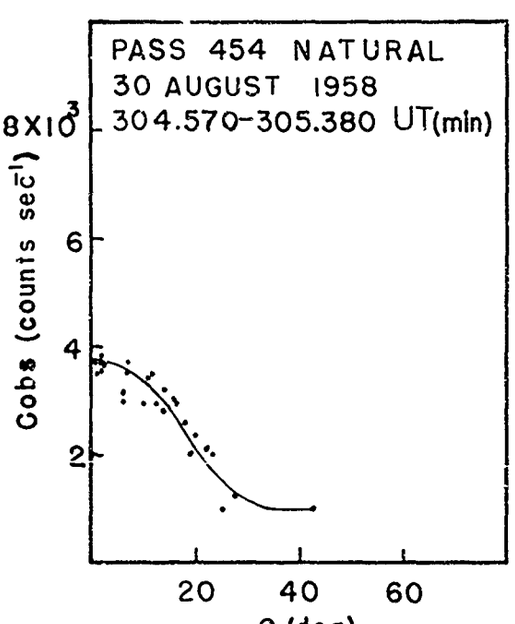
PASS 454 NATURAL
30 AUGUST 1958
304.570-305.380 UT(min)
8X10³
6
4
2
Cobs (counts sec⁻¹)
20
40
60
θ (deg)

Fig. B2. True count-rate $C(\theta)$ (counts $cm^{-2}sec^{-1}$ corrected for deadtime, effective area and counter efficiency) and directional flux $J(\theta')$ (particles $cm^{-2}sec^{-1}ster^{-1}$) vs θ and θ' for the Fig. B1 $C_{obs}(\theta)$ curves. The bars on the $J(\theta')$ vs θ' curves indicate the scatter in calculated values of $J(\theta')$ due in turn to the scatter of points in the corresponding $C_{obs}(\theta)$ vs θ curves.

Table B1. Characteristics of Natural radiation (from Ref. B1)

Time (min)	*hwhm (deg)	$J(\theta')_{max}$	B (gauss)	L(earth radii)
300.00	22.0	4.9×10^{7}	.1734	1.376
301.221	17.5	4.9×10^{7}	.1782	1.414
301.915	17.5	4.7×10^{7}	.1806	1.434
302.370	17.5	3.5×10^{7}	.1834	1.458
304.570	16.0	1.4×10^{7}	.1912	1.583
305.725	16.0	8.2×10^{6}	.2172	1.640
306.990	12.0	7.7×10^{6}	.2316	1.776

* half-width at half-maximum

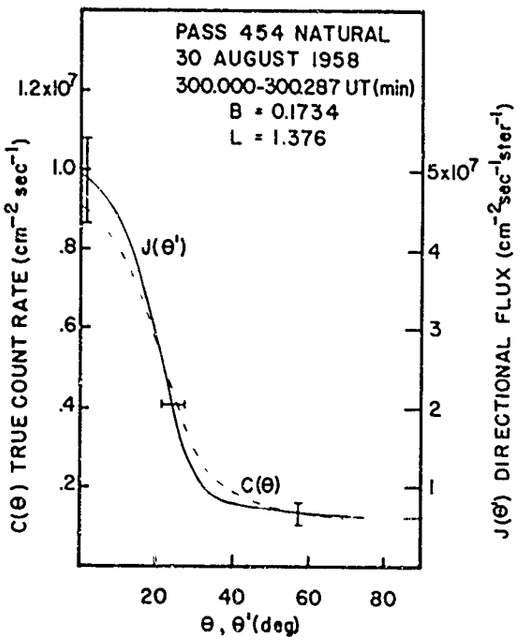
PASS 454 NATURAL
30 AUGUST 1958
300.000-300.287 UT(min)
B = 0.1734
L = 1.376
J(θ')
C(θ)
C(θ) TRUE COUNT RATE (cm⁻² sec⁻¹)
J(θ') DIRECTIONAL FLUX (cm⁻²sec⁻¹ster⁻¹)
θ, θ'(deg)

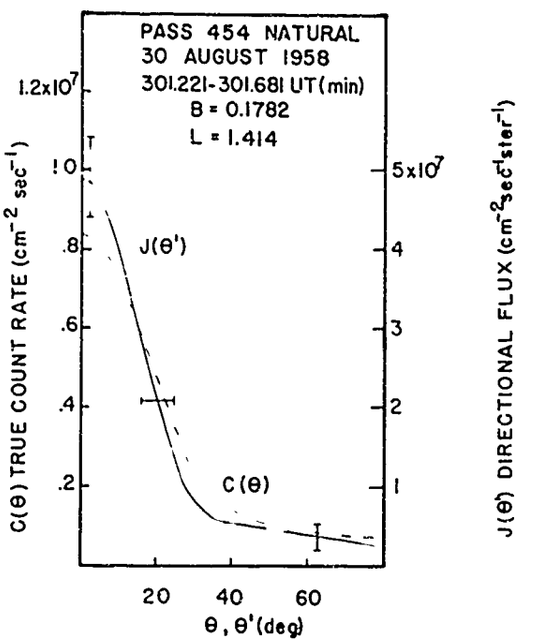
PASS 454 NATURAL
30 AUGUST 1958
301.221-301.681 UT(min)
B = 0.1782
L = 1.414
J(θ')
C(θ)
C(θ) TRUE COUNT RATE (cm⁻² sec⁻¹)
J(θ') DIRECTIONAL FLUX (cm⁻²sec⁻¹ster⁻¹)
θ, θ'(deg)

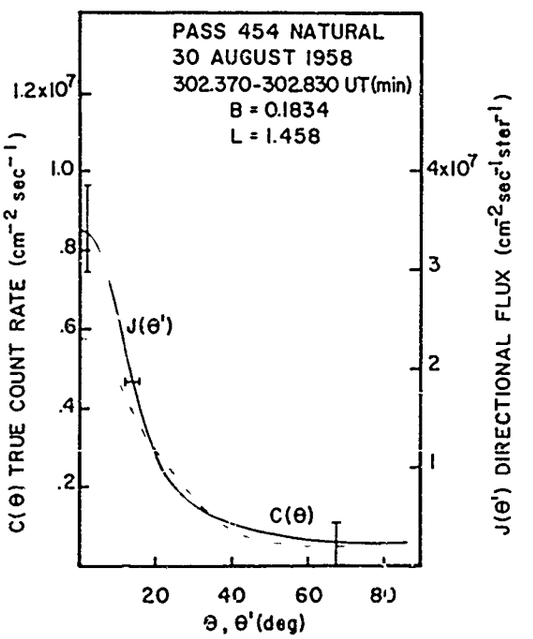
PASS 454 NATURAL
30 AUGUST 1958
302.370-302.830 UT(min)
B = 0.1834
L = 1.458
J(θ')
C(θ)
C(θ) TRUE COUNT RATE (cm⁻² sec⁻¹)
J(θ') DIRECTIONAL FLUX (cm⁻²sec⁻¹ster⁻¹)
θ, θ'(deg)

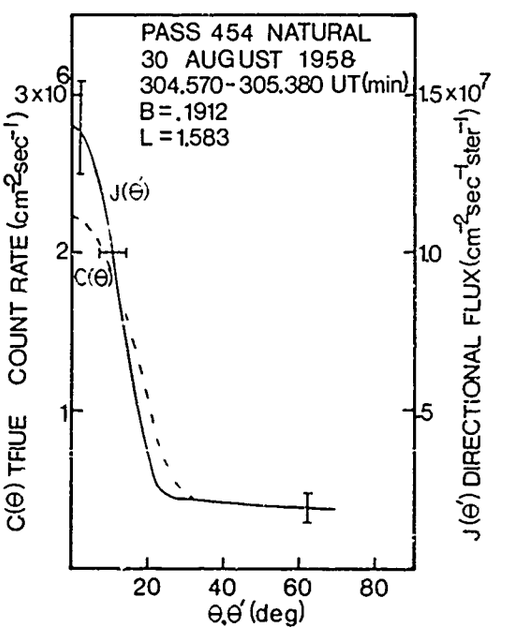
PASS 454 NATURAL
30 AUGUST 1958
304.570-305.380 UT(min)
B = .1912
L = 1.583
J(θ')
C(θ)
C(θ) TRUE COUNT RATE (cm⁻²sec⁻¹)
J(θ') DIRECTIONAL FLUX(cm⁻²sec⁻¹ster⁻¹)
θ,θ' (deg)

Fig. B3.

(a) $C_{obs}(\theta)$ vs θ ARGUS Event 2 'loop' before the linearly increasing background has been subtracted. Compare Fig. B3(c) which is the resulting $C_{obs}(\theta)$ vs θ curve after subtraction of background. The background subtracted is represented by (constant x t_i), where t_i is the time (following the time of the first point of a given $C_{obs}(\theta)$ vs θ curve) corresponding to the i^{th} point of the given curve.

(b)(c)(d) $C_{obs}(\theta)$ vs θ for Pass 454 ARGUS Event 2 radiation after loop closure is accomplished.

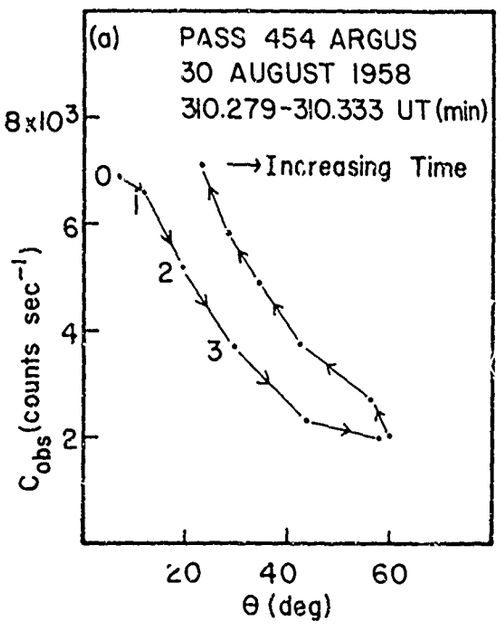
(a)
PASS 454 ARGUS
30 AUGUST 1958
310.279-310.333 UT(min)
→Increasing Time
0
1
2
3
8x10³
6
4
2
C_obs(counts sec⁻¹)
20
40
60
θ (deg)

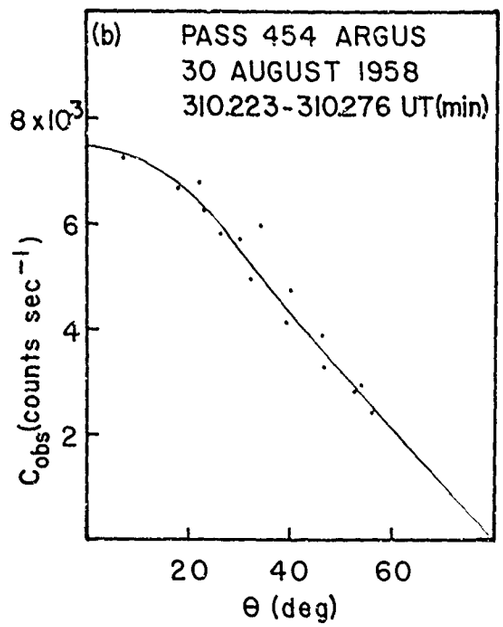
(b)
PASS 454 ARGUS
30 AUGUST 1958
310.223-310.276 UT(min)
8x10³
6
4
2
C_obs(counts sec⁻¹)
20
40
60
θ (deg)

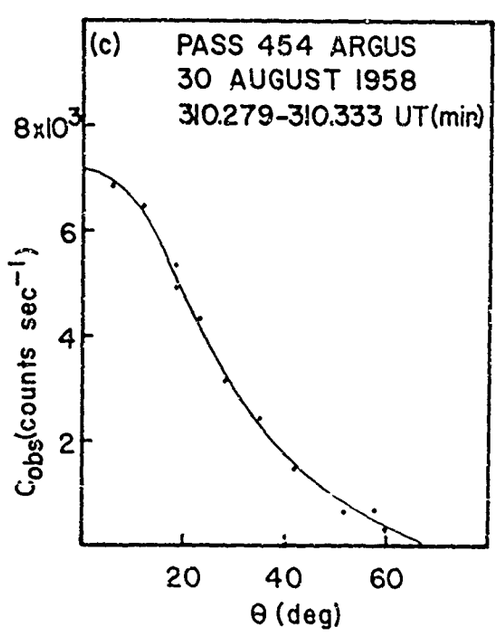
(c)
PASS 454 ARGUS
30 AUGUST 1958
310.279-310.333 UT(min)
8x10³
6
4
2
C_obs(counts sec⁻¹)
20
40
60
θ (deg)

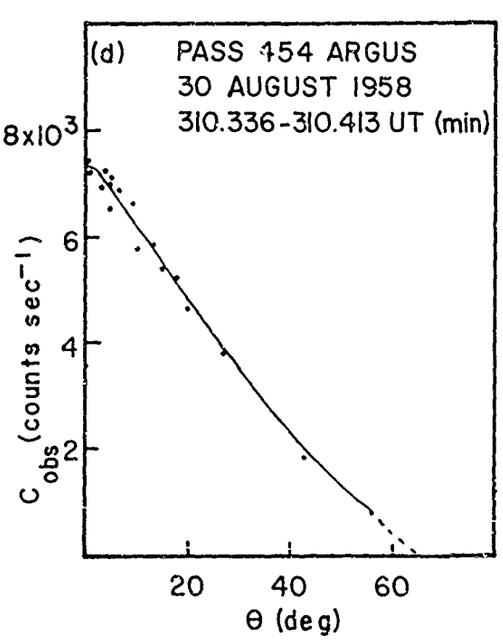
(d)
PASS 454 ARGUS
30 AUGUST 1958
310.336-310.413 UT (min)
8x10³
6
4
2
C_obs (counts sec⁻¹)
20
40
60
θ (deg)

Fig. B4. $C(\theta)$ and $J(\theta')$ vs θ and θ' for the $C_{obs}(\theta)$ vs θ curves (Fig. B3), Pass 454 ARGUS Event 2. The bars on curves indicate the scatter in calculated values of $J(\theta')$ as above (Fig. B2).

Table B2. Characteristics of the Pass 454 ARGUS Event 2 radiation (taken from Ref. B1).

Time (min)	hwhm (deg)	$J(\theta')_{max}$	B (gauss)	L(earth radii)
310.178	12.0	3.2×10^7	.2720	2.120
310.223	24.0	5.65×10^7	.2726	2.124
310.279	13.0	5.95×10^7	.2740	2.128
310.336	14.0	6.45×10^7	.2742	2.144
310.496	19.0	2.82×10^6	.2764	2.172

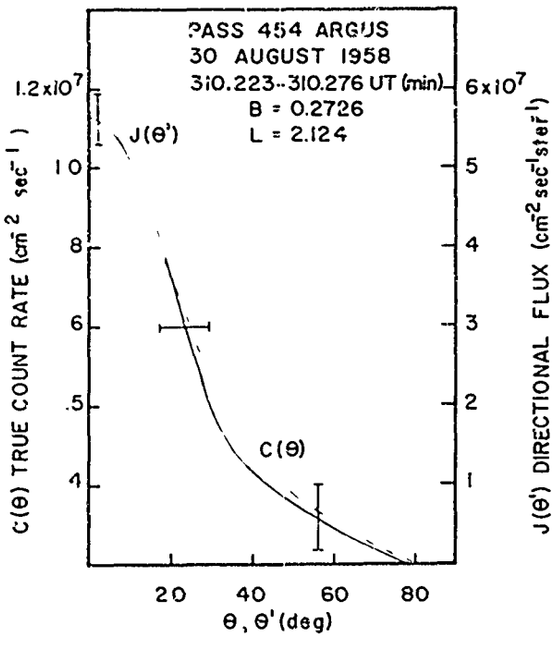
PASS 454 ARGUS
30 AUGUST 1958
310.223-310.276 UT (min)
B = 0.2726
L = 2.124
J(θ')
C(θ)
C(θ) TRUE COUNT RATE (cm⁻² sec⁻¹)
J(θ') DIRECTIONAL FLUX (cm⁻² sec⁻¹ ster⁻¹)
θ, θ' (deg)

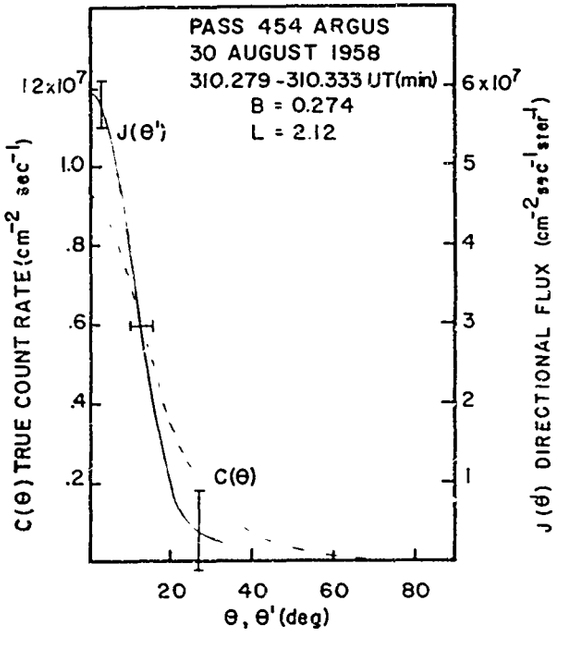
PASS 454 ARGUS
30 AUGUST 1958
310.279 -310.333 UT(min)
B = 0.274
L = 2.12
J(θ')
C(θ)
C(θ) TRUE COUNT RATE (cm⁻² sec⁻¹)
J(θ') DIRECTIONAL FLUX (cm⁻² sec⁻¹ ster⁻¹)
θ, θ' (deg)

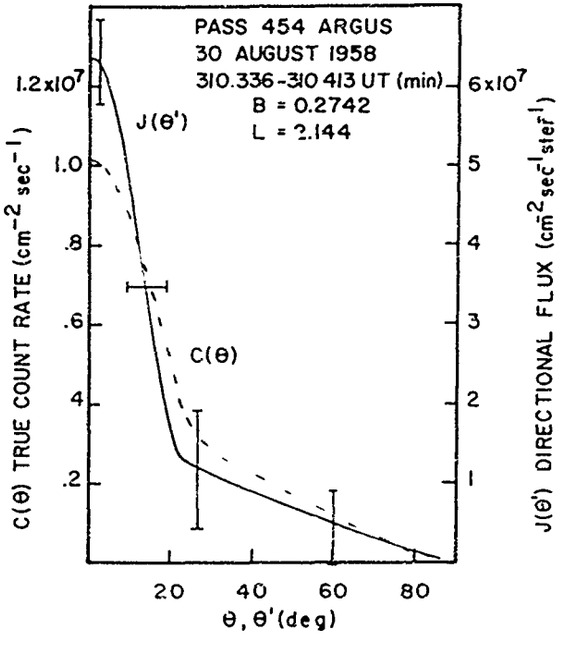
PASS 454 ARGUS
30 AUGUST 1958
310.336-310 413 UT (min)
B = 0.2742
L = 2.144
J(θ')
C(θ)
C(θ) TRUE COUNT RATE (cm⁻² sec⁻¹)
J(θ') DIRECTIONAL FLUX (cm⁻² sec⁻¹ ster⁻¹)
θ, θ' (deg)

Table B3. Summary of results, Natural and ARGUS radiations

Natural Radiation

Pass No.	Max flux density $J(\theta')$ ($cm^{-2}sec^{-1}ster^{-1}$)	hwhm (deg)	B,L, (gauss, earth radii)	Time UT (min)
414*	7.3×10^7	21	.158, 1.38	249.049-249.302
	5.6×10^7	27	.166, 1.41	250.004-250.559
427*	1.2×10^8	16	.149, 1.366	227.500-229.000
	6.5×10^7	20	.171, 1.447	231.000-232.000
	2.7×10^7	15	.198, 1.580	234.000-235.000
454*	5.0×10^7	27	.157, 1.35	299.000-299.217
454	4.9×10^7	17.5	.178, 1.414	301.221-301.681
	4.7×10^7	17.5	.181, 1.434	301.915-302.143
453***	4.5×10^5	23	.155	188.300
479***	4.5×10^5	29	.155	145.450

Continued on next page

Table B3. (continued)

ARGUS Radiation

Event, time following Event, Pass No.	Max flux density $J(\theta')$ ($cm^{-2}sec^{-1}ster^{-1}$)	hwhm (deg)	B,L (gauss, earth radii)	Time UT (min)
1 + 1.8 hr, 414*	2.0×10^8	28	.221, 1.68	256.083-256.144
	2.3×10^8	24		256.177-256.209
	7.8×10^7	25		256.282-256.315
1 + 3.67 hr, 415##	1.96×10^8	32	.24 , 1.70	367.5 -368.0
1 + 25.48 hr, 427*	1.6×10^7	19	.213, 1.675	236.0 -236.5
	2.6×10^7	27	.217, 1.724	236.5 -236.68
	6.7×10^7	21	.219, 1.739	236.69 -236.85
	1.6×10^7	32	.220, 1.740	236.871-237.0
	1.3×10^7	24	.224, 1.757	237.0 -237.1
427##	2.3×10^7	20	.22 , 1.7	236.5 -237.0
1 + 39.13 hr, 440##	1.96×10^7	18	.22 , 1.7	216. -217.
2 + 1.87 hr, 454	5.65×10^7	24	.273, 2.124	310.223-310.276
	5.95×10^7	13	.274, 2.128	310.279-310.333
	6.45×10^7	14	.274, 2.144	310.336-310.413

Table B3. (continued)

Natural and ARGUS Radiation
(J. Bock#)

Pass	Max flux density# J(θ') ($cm^{-2}sec^{-1}ster^{-1}$)	hwhm (deg)	Time UT (min)
414 Natural	1.6×10^4	30	247.800-249.270
414 Natural	1.4×10^4	32	248.270-250.740
414 Natural	1.4×10^4	26	250.740-252.200
414 Natural	1.3×10^4	24	252.200-253.850
414 Natural	1.4×10^4	26	253.850-255.060
414 Natural	1.6×10^4	38	255.060-256.450
414 ARGUS	2.0×10^4		256.950-257.000
415 Natural	1.4×10^4	25	367.420-369.080
415 Natural	1.2×10^4	22	369.080-370.770
415 ARGUS	1.4×10^4	39	373.920-374.220
415 ARGUS	1.7×10^4	33	374.670-375.220
427 Natural	1.6×10^4	34	236.670-238.340
427 Natural	1.5×10^4	37	238.340-240.000
427 Natural	1.5×10^4	32	240.000-241.670
427 Natural	1.2×10^4	26	241.670-245.
427 ARGUS	$.9 \times 10^4$	30	245.470-246.270
428 Natural	1.4×10^4	31	347.550-349.220
428 Natural	1.4×10^4	25	349.220-352.550
	1.0×10^4		

* Taken from Manson (B2)
*** Lundquist-Weber et al (B5)
\# J. Bock (B4) Not corrected for counter response function and deadtime
\#\# J. M. Paikeday (B3)

C. Summary of Ph.D. Dissertation, John A. George, "Omnidirectional Fluxes; Explorer 4 Satellite Data, ARGUS Events 1 and 2", Saint Louis University, Physics Department (February 1967).

C1. Introduction

In August and September 1958, three low yield nuclear detonations (ARGUS Events 1, 2, 3) were produced at high altitude over the south Atlantic Ocean. Electrons emitted were subsequently trapped in the geomagnetic field. The characteristics of this radiation were measured by instruments on board Jason sounding rockets and in the Satellite Explorer 4. A number of papers have appeared in which the results of what is known as the ARGUS Experiment were described (Refs. C1, C2, C3).

The present Dissertation is concerned with further analysis of data obtained by Explorer 4 for ARGUS Events 1 and 2 for the G-M Detectors C (Channel 3) and D (Channel 1); therefore data for omnidirectional radiation is considered.

C2. Experimental Details

The characteristics of satellite Explorer 4 (1958 Epsilon) have been described in detail by Van Allen (Ref. C2). For later calibration information, as used in the present report, see Preface P2 of this report. The Anton 302 G-M counters only are involved in the present analysis. A summary of the characteristics of these two detectors is given in Table C1. These detectors are omnidirectional and do not differentiate the kinds of particles being detected. However for the ARGUS radiation, it will be assumed that the predominant contribution to the counting rates is by electrons resulting from the fission processes. Anton 302 G-M counters similar to those on Explorer 4

have since been flown on a number of satellites, and it has been concluded (Refs. C4, C5, C6) that the counting rates must be attributed to penetrating electrons of $E_e > 1.5$ MeV. Motz and Carter (Ref. C7) studied the response of Anton 302 counters to fission-spectrum electrons. They found that up to 2 gm/cm^2 of lead-absorber thickness the curves were as expected for β-transmission; however, for energies beyond this range the transmission was enhanced somewhat by bremmstrahlung. Detector C (the "unshielded" G-M counter, Channel 3) is shielded by 1.2 gm/cm^2 of stainless steel, which is equivalent to a shielding of 1.46 gm/cm^2 of aluminum. The extrapolated range R_E (gm/cm^2) versus energy E(MeV) for aluminum given by Marshall and Ward (Ref. C8) is

$$R_E = 0.528E - 0.094 \qquad \text{(C1)}$$

For Detector C, R_E by Eq. (1) corresponds to 2.95 MeV electrons (Table C2); for Detector D (the "shielded" G-M counter, Channel 1) which had an additional shielding of 1.6 gm/cm^2 of lead, the total shielding is equivalent to 3.89 gm/cm^2 of aluminum and R_E corresponds to 7.6 MeV electrons. For the unshielded Detector C at least the assumption of electrons being counted directly seems quite valid. However, the count-rate of the shielded Detector D may be enhanced somewhat by bremmstrahlung. A plot of the omnidirectional geometrical factors versus the energy necessary to penetrate the various thickness of material, using the information of Tables C1 and C2, is given in Fig. C1.

An automatic digitizer was used to analyze the telemetry playback data and transform it to punch cards. A computer program was

written to obtain count-rate versus time for each selected Pass of the Satellite Explorer 4 over Huntsville, Alabama. The observed count-rates C_{obs} (sec^{-1}) were corrected for the deadtime of the detectors and associated electronics to obtain true count-rates C (sec^{-1}) by using the approximation (instead of Eq. (D1), p. D2 below)

$$C_{obs} = \frac{C_{obs}}{1 - \tau_i C_{obs}} \qquad (C2)$$

where deadtime τ_i is 62.5 microsecs (Ref. C2) and was confirmed in the present work. Figure C2 is typical of the data available for analysis.

The B and L coordinates for the ARGUS region were obtained from GE TEMPO Data Center (Santa Barbara, California) through the offices of the Defense Atomic Support Agency. Figure C3 shows the regions of interest traversed by Explorer 4 in B-L space for typical Passes over Huntsville, Alabama. Table C3 lists the complete set of Passes analyzed and are arranged in three columns, each of which corresponds to nearly the same region of space relative to the earth. The orbital frequency of Explorer 4 was about 13 orbits per day.

In order to investigate the possible correlation of Explorer 4 ARGUS count-rates with solar activity, 3-hr K_p indices are presented by Fig. C4 for the period under investigation 27 August to 4 September 1958. Subsequent to the large geomagnetic fluctuations observed at the onset, a period of decreasing activity to relative magnetic quiet levels followed. No sudden commencements were observed until 3-5 September, a period which is classified as one of magnetically disturbed days.

C3. Results

ARGUS Event 1

The decay of the fission produced electrons trapped in the earth's magnetic field is indicated in Fig. C5, a log-log plot of the true count-rate versus T_e, the elapsed time since Event 1, at a fixed L value. The plotted points are the true omnidirectional count-rates of the unshielded G-M counter (Detector C, Channel 3). The count-rates are differences between total and estimated background rates, and are for the 414, 427, ...518 sequence of Passes. The maximum intensities observed are well represented by the L = 1.72 shell. The peak location did not shift, at least within the experimental error, from this L shell during the time interval indicated. If it is assumed C (sec^{-1}) versus t(hrs) is given by

$$C = C_o t^{-n}, \qquad (C3)$$

where C_o and n are undetermined constants, a least squares fit of the data for L = 1.72 yields n = 1.13, $C_o = 1.31 \times 10^5$; whence Eq. (C3) becomes

$$C = 1.31 \times 10^5 t^{-1.13}, \quad 0.19 < B < 0.23. \qquad (C4)$$

This $t^{-1.13}$ law agrees quite well with the decay rate determined by Cladis and Walt (Ref. C3) from Jason rocket data for ARGUS Event 2 (L = 2.1).

Figure C6 is a plot of the count-rate ratio unshielded/shielded omnidirectional G-M counters. Data for shielded and unshielded G-M counter of rates greater than 10 sec^{-1} and 30 sec^{-1} respectively, only were used to eliminate data averaged over larger regions of space.

The data for Pass 414 may be in considerable error due to saturation of the counters. The vertical bars are estimates of the spread of data arising principally from the scatter in the count-rates of the shielded G-M counter. The count-rate ratios terminate at Pass 466 due to the difficulty of separating the ARGUS electrons from the natural background radiation. The dashed line is the plot of $C = C_o t^{-1.13}$. Of interest is the sudden broadening of the ARGUS Event 1 shell subsequent Pass 453, Fig. C7. The shell width at half-maximum is given in terms of Δ L.Pass 453 was the first pass to record the effect of Event 2 but all data of Fig. C7 are for Event 1. However, Event 2 occurred subsequent to the satellite traversing the Event 1 Pass 453 shell. Since Passes up to 492 occurred during a period of low geomagnetic activity ($K_p < 3_o$) it is suggested that the broadening observed on Fig. C7 is due to ARGUS Event 2.

Figure C14, a 3-dimensional plot of true count-rate vs B and L, summarizes the data analyzed for the unshielded G-M counter (Detector C, Channel 3) for ARGUS Event 1.

ARGUS Event 2

The data analyzed for ARGUS Event 2 is over a smaller time interval than Event 1. Figure C8 gives the true count-rate versus elapsed time since Event 2. Again the data is for count-rates above the estimated background. The peak intensities were centered very nearly at L = 2.11. Pass 453 was the first to indicate ARGUS Event 2, 0.03 hours after the event. Considering the location of the satellite (297° E, 27° N) and the detonation (352° E, 50° S), fission electrons would need to have energies in excess of 19 MeV to reach the satellite position in

their eastward drift in the 108 seconds (Ref. C25). Although there is a significant number of MeV-range β-electrons available from the β-decay spectra of fission products, the β-decay end point energies are well below 19 MeV. Hence the initial count-rate may be due to direct illumination by γ -rays emitted by the fission debris. The bomb debris would have to expand to a higher altitude than the detonation point (about 480 km) in order to be in the line of sight of the satellite. Colgate (Ref. C9) discusses the mass motion of a high altitude nuclear explosion. He assumes that the detonation products produce a cavity in the magnetic field and, in general, the hole will expand until the work done against the magnetic field equals the kinetic energy of the detonation products. When the expansion of the detonation plasma products ceases, the subsequent motion will be a spreading along the lines of force away from the detonation hemisphere. This occurs in the order of seconds according to Colgate. With the debris distributed along the lines of force for L = 2.11, the satellite would be in a position to detect the emitted γ -rays.

The decay rates of ARGUS Event 2 are very nearly represented by a 1/t law if the data for Passes 466-492 are considered. However, Passes 505 and 518 indicate increases in count-rate in a manner difficult to explain (Fig. C9). A sudden commencement of solar activity did occur shortly after Pass 505 and 3-5 September are listed as magnetically disturbed days.

It is noted that the shielded G-M counter (Detector D, Channel 1) had very low count-rates for the sequence of Passes analyzed for ARGUS Event 2. These were typically less than 20 sec^{-1}. Figure C10 shows the count-rate ratio of the unshielded/shielded G-M counter for the L

shell of peak intensity (L = 2.11) for Passes 466-492. Subsequent to Pass 492 the ARGUS Event 2 electrons detected by the shielded counter were indistinguishable from the natural radiation.

C4. ARGUS Loss Mechanisms

The effect of the atmosphere on the decay of the trapped electrons has been calculated using a Fokker-Planck approach to derive a diffusion equation (Ref. C10). This technique was applied by Walt (Ref. C11), also Walt and Newkirk (Ref. C12) to the observed time variation produced by the Starfish nuclear explosion. In regions of the magnetosphere for which L = 1.3, it was found that the dominant factor limiting the trapping time of electrons is scattering by components of the atmosphere. However, for L = 1.3 the decay of trapped electrons is dominated by other loss mechanisms of electromagnetic-hydromagnetic character.

A breakdown of the adiabatic invariants which will eventually enhance the atmosphere losses has been proposed by a number of authors. The processes responsible for the violation of the third adiabatic invariant have been considered by Parker (Ref. C13), Davis and Chang (Ref. C14), and Nakada and Mead (Ref. C15). Large scale geomagnetic fluctuations associated with sudden commencements and the initial phase of geomagnetic storms can cause diffusion of electrons across L shells. However, the dominant effect would be in the outer radiation zone, and repeated magnetic storms would seem to be necessary for rapid diffusion. The exact analytic details are quite complicated and have not been attempted so far in the present work - however the concept is highly suggestive. Sudden commencements were observed on August 27 at 0243, 0303, and 0541 hrs UT. Pass 414 traversed the ARGUS Event 2 region at approximately 0456 UT, 1.8 hours after the event. No further

sudden commencements were observed until September 3 and 4 which coincide with Passes 505 and 518 respectively.

The effect of several other electromagnetic-type loss contributing factors have been studied by workers in this field, as follows. Resonant particle-wave interaction in which the magnetic moment invariance is violated has been studied by Wentzel (Ref. C16), Dragt (Ref. C17), and also Chang and Pearlstein (Ref. C18). A summary of Dragt's work (Ref. C17) on the effect of hydromagnetic waves is given by Fig. C11. Critical energies below which the magnetic moment is conserved in interactions with hm waves are shown for particles mirroring at latitudes greater than 30 degrees assuming the hm wave frequency is cut off sharply at ν_{max}. Various cut-off frequencies are indicated as it is assumed that hm waves may vary from 1 to 5 sec^{-1} up to the local proton cyclotron frequency. It is clear that such frequencies would not be very effective in interaction with ARGUS electrons. Wentzel gives a qualitative discussion to the effect that hm waves could influence the mirror point distribution of the relativistic ARGUS electrons during a geomagnetic storm. This may be a contributing factor to the large loss observed within the first day which was active magnetically.

Again, the precipitation of electrons through the action of whistlers has been investigated by Dungey (Ref. C19) and by Cornwall (Ref. C20). For resonant interaction to take place, the Doppler-shifted frequency of the whistler as seen by the electron must be equal to the relativistic cyclotron frequency of the moving electron. Figure C12 summarizes Cornwall's results showing the L dependence of the precipitating particles with increasing electron energy. The ARGUS

Events 1 and 2 regions are shown, indicating, at least qualitatively, that whistlers may not be a major mechanism driving electrons to larger B values.

Also, Paulikas et al (Ref. C21) suggest longitudinal waves propagating along magnetic field lines would interact with electrons at their mirror points and would be an efficient loss mechanism. These electrostatic waves may be able to move electrons to larger B values in times of the order of days.

Further detailed theoretical investigations are needed before quantitative results may be given to adequately explain the rapid decay of the ARGUS electron shells.

C5. Conclusions

The analysis of the data obtained by the omnidirectional G-M counters (Detectors D, C; Channels 1, 3) carried by Explorer 4 for the ARGUS Events 1 and 2 can be summarized as follows.

The two Events are centered on the L = 1.72 and L = 2.11 shells respectively. The locations of the peak intensities did not vary, at least within experimental error, from these values during the time of observation. The ARGUS Event 1 region showed a decay law of $t^{-1.13}$ for $E_e > 3$ MeV. The count-rate ratio of the unshielded to the shielded counter was found to decrease with time. This indicates spectral changes occur which is in apparent contradiction with the results of the published Jason rocket data. A general broadening of the ARGUS Event 1 region was observed subsequent to the detonation of ARGUS Event 2. The increase in the width at half-maximum was by a factor of 1.5. ARGUS Event 2 seemed to be influenced to a greater degree

than ARGUS Event 1 by the magnetically disturbed days of September 3-5. McIlwain (Ref. C22) theorized that magnetic storms produce a decrease in electron flux which occurs so quickly that it is difficult to follow and then is followed by an increase larger than normal. The observed increases on Passes 505 and 518 of Event 2 may be related to these magnetic storm effects. The larger value L shells of Event 2 compared to Event 1 may account for the variation of the storm influence. Although a general decrease in count-rate ratios were observed for both events, ARGUS Event 2 was not as sharp as the first event and may point to L dependence of the decaying fission spectrum. The data is too limited to determine the precise nature of this dependence.

The decay of the ARGUS Event 1 region was found to follow a $t^{-1.13}$ law. It may be coincidental that this is nearly identical to the fission product decay law. The fission fragment β-ray source strength decays approximately according to a $t^{-1.2}$ law (Ref. C23). Measurements indicate that although the $t^{-1.2}$ decay represents a reasonable average there have been instances where exponents in the range -0.9 to -2.0 are required to represent the rate of decay. Figure 13, from Heller (Ref. C24), gives the number of beta rays per fission from U^{235} per energy interval versus time for various energies. The ratio of high energy to low energy β-rays decreases with time. This contradicts the results of Figs. C6 and C10 which indicated the unshielded/shielded count-rate ratio that is, $C(E_e > 3$ MeV)/ $C(E_e > 7.6$ MeV), decreases with time. Further study is required on the lifetimes of the fission debris which is trapped in the earth's geomagnetic field.

A brief study was conducted of possible mechanisms which would

explain the rapid decay of the ARGUS Events. Theories involving the breakdown of the adiabatic invariants have been proposed by a number of workers. The author (J. George) applied these theories to the ARGUS data. Computations indicate that hydromagnetic waves and whistler interactions resulting in the violation of the first invariant are not, at least qualitatively, major mechanisms in removing ARGUS electrons. Although resonant particle-wave interactions, and other processes such as diffusion, may operate, they do not dominate. Further theoretical work is necessary to determine the controlling mechanism for the ARGUS decay.

Adiabatic processes such as betatron acceleration and deceleration cannot be excluded in any detailed analysis of irreversible loss mechanisms. The effect of slow changes in the magnetic field upon the omnidirectional intensity of particles was considered and calculations for the ARGUS time period show that the changes are not inconsequential. By making conservative assumptions concerning the change in the magnetic field during the main phase decrease following Pass 414, it was shown that the relative intensity could change by 15% due to the betatron acceleration alone.

C6. References.

C1. Christofilos, N. C., "The ARGUS Experiment", J. Geophys. Res. 64, 869-875, 1959

C2. Van Allen, J. A., McIlwain, C. E., and Ludwig, G. H., "Satellite Observations of Electrons Artificially Injected into the Geomagnetic Field", J. Geophys. Res. 64, 877-891, 1959.

C3. Cladis, J. B. and Walt, M., "Behavior of Geomagnetically Trapped Electrons Injected by High Altitude Nuclear Explosions", J. Geophys. Res. 67, 5035-5054, 1962.

C4. O'Brien, B. J., Van Allen, J. A., Laughlin, C. D., and Frank, L. A. "Absolute Electron Intensities in the Heart of the Earth's Radiation Zone", J. Geophys. Res. 67, 397-403, 1962.

C5. Frank, L. A., Van Allen, J. A., Whelpley, W. A., and Craven, J. D., "Absolute Intensities of Geomagnetically Trapped Particles with Explorer 14", J. Geophys. Res. 68, 1573-1579, 1963.

C6. Frank, L. A., Van Allen, J. A., and Hills, H. K., "A Study of Charged Particles in the Earth's Outer Radiation Zone with Explorer 14", J. Geophys. Res. 69, 2171-2191, 1964.

C7, Motz, H. T., and Carter, R. E., "Artificial Radiation Belt Studies with a Fission Beta-Ray Source", J. Geophys. Res. 68, 657-661, 1963.

C8. Marshall, J. S., and Ward, A. G., "Absorption Curves and Ranges for Homogeneous β-Rays, Can. J. Res. V. 15-A, 39-41, 1937.

C9. Colgate, S. A., "The Phenomenology of the Mass Motion of a High Altitude Nuclear Explosion", J. Geophys. Res. 70, 3161-3173, 1965

C10. MacDonald, W. M., and Walt, M., "Distribution Function of Magnetically Confined Electrons in a Scattering Atmosphere", Annals of Phys. 15, 44-62, 1961.

C11. Walt, M., "The Effects of Atmospheric Collisions on Geomagnetically Trapped Electrons", J. Geophys. Res. 69, 3947-3958, 1964.

C12. Walt, M., and Newkirk, L. L., "Addition to Investigation of the Decay of the Starfish Radiation", J. Geophys. Res. 71, 3265-3266, 1966

C13. Parker, E. N., "Geomagnetic Fluctuations and the Form of the Outer Zone of the Van Allen Radiation Belt", J. Geophys. Res. 65, 3117-3130, 1960.

C14. Davis, L., and Chang, D. B., "On the Effect of Geomagnetic Fluctuations on Trapped Particles", J. Geophys. Res. 67, 2169-2179, 1962.

C15. Nakada, M. P., and Mead, G. D., "Diffusion of Protons in the Outer Radiation Zone", J. Geophys. Res. 70, 4777-4791, 1965.

C16. Wentzel, D., "Hydromagnetic Waves and Trapped Radiation", Part 1 and 2, J. Geophys. Res. 66, 359-369, 1962.

C17. Dragt, A. J., "Effect of Hydromagnetic Waves on the Lifetimes of Van Allen Radiation Protons", J. Geophys. Res. 66, 1641-1649, 1961

C18. Chang, D. B., and Pearlstein, L. D., "On the Effect of Resonant Magnetic-Moment Violation on Trapped Particles", J. Geophys. Res. 70, 3075-3083, 1965.

C19. Dungey, J. W., "Loss of Van Allen Electrons due to Whistlers", Planetary Space Sci., 11, 591-596, 1963.

C20. Cornwall, J. M., "Scattering of Energetic Trapped Electrons by Very Low-Frequency Waves", J. Geophys. Res. 69, 1251-1258, 1964

C21. Paulikas, G. A., Blake, J. B., and Freden, S. C., "Precipitation of Energetic Electrons at Middle Latitudes", J. Geophys. Res. 71, 3165-3172 (1966)

C22. McIlwain, C. E., comment in Illinois Institute of Technology Report T6118 (1965); "Radiation Trapped in the Earth's Magnetic Field"

C23. Glasstone, S., editor, U. S. Atomic Energy Commission Report, Washington, D.C. (1962); "The Effects of Nuclear Weapons"

C24. Heller, R. B., "Energy and Time Beta Ray Spectra of Fission Products of U^{235} by Fission Neutrons and U^{238} by 14 MeV Neutrons", Weapon System Evaluation Group Res. Mem. 19, Pentagon, Washington, D.C., 1961

C25. Lew, J. S., "Drift Rate in a Dipole Field", J. Geophys. Res. 66, 2681-2685 (1961).

Table C1 (Ref. C2) Characteristics of G-M counters, Explorer 4

Detector	D (Channel 1)	C (Channel 3)
	"Shielded" Geiger-Mueller counter (Anton 302) Cylinder approximately 7 mm x 9 mm Scalar: 64	"Unshielded" Geiger-Mueller counter (Anton 302) Cylinder approximately 7 mm x 9 mm Scalar: 2048
Shielding	1.2 gm/cm^2 Fe + 1.6 gm/cm^2 Pb (minimum)	1.2 gm/cm^2 Fe (minimum)
Sensitive to:	Electrons of $E_e > 5$ MeV, Protons of $E_p > 40$ MeV, X-rays of $E > 80$ KeV with low efficiency	Electrons of $E_e > 3$ MeV, Protons of $E_p > 30$ MeV, X-rays of $E > 20$ KeV with low efficiency
Geometric Factor:	Omnidirectional geometric factor G_o: 0.14 cm^2 for minimum stopping power, 0.82 cm^2 for penetrability greater than 7 gm/cm^2	Omnidirectional geometric factor G_o: 0.14 cm^2 for minimum stopping power, 0.70 cm^2 for penetrability greater than 5 gm/cm^2

Table C2. Shielding and Range-energy data for G-M Detector C, D			
Detector	Shielding (gm/cm^2)	Equivalent Al. (gm/cm^2)	Energy (MeV)
C	1.2 Fe	1.46	2.95
D	1.2 Fe + 1.6 Pb	3.89	7.6

Table C3. Explorer 4 Passes "over" Huntsville, Alabama selected for omnidirectional radiation analysis

ARGUS Event 1 (time of burst: 0230 UT August 27, 1958)

Date		Pass	Pass	Pass
August	27, 1958	414	415	416
	28	427		
	29	440		
	30	453	454	
	31	466		
September	1, 1958	479		
	2	492		
	3	505		
	4	518		

ARGUS Event 2 (time of burst: 0320 UT August 30, 1958)

Date		Pass	Pass	Pass
August	30, 1958	453	454	455
	31	466		
September	1, 1958	479		
	2	492		
	3	505		
	4	518		

Fig. C1. Geometrical factor, G_o (cm^2), versus the energy (MeV) necessary for transmission by the various thicknesses of materials. Circled points are from Table C2, using Eq. (C1), assuming a linear dependence of G_o with E between plotted points and constant values for larger energies (as shown).

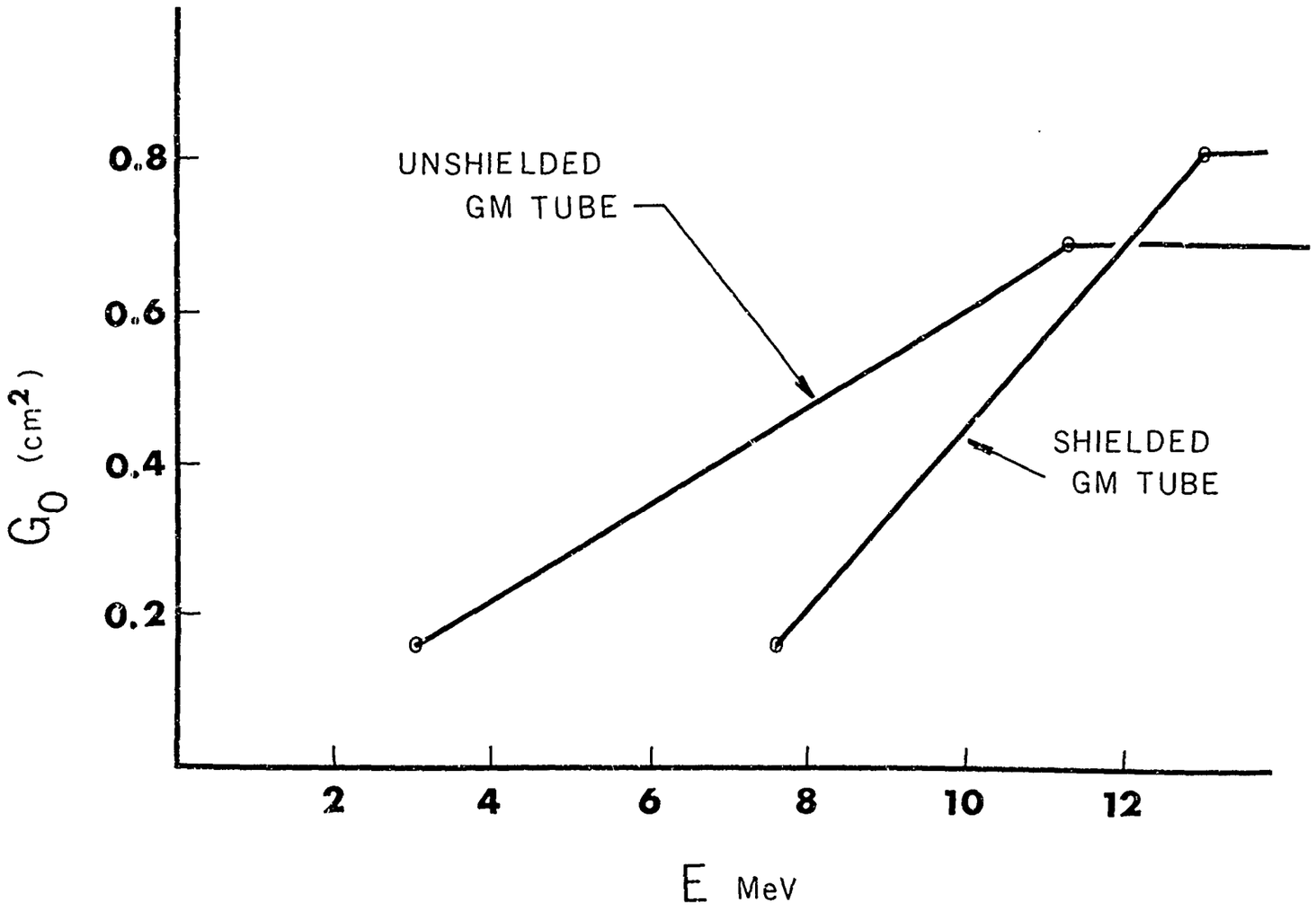
0.8
0.6
0.4
0.2
G_0 (cm^2)
UNSHIELDED
GM TUBE
SHIELDED
GM TUBE
2
4
6
8
10
12
E MeV

Fig. C2. Omnidirectional count-rates vs time for a typical Pass of Explorer 4 in the ARGUS Event 1 region. The solid lines are average count-rates drawn through points not shown.

Curve A. Unshielded G-M counter (Detector C, Channel 3) which detects electrons of energy greater than 3 MeV. The background has been drawn in by estimation.

Curve B. Shielded G-M counter (Detector D, Channel 1) which detects electrons of energy greater than 7.6 MeV. The background has been drawn in by estimation.

Curve C. Ratio of A/B, unshielded to shielded G-M count-rates. The ratios are of count-rates above the background.

Curve D. Difference A - B, unshielded minus shielded G-M count-rates above the background. This curve shows the omnidirectional count-rates due to electrons between 3 and 7.6 MeV, a roughly "monoenergetic" count-rate curve.

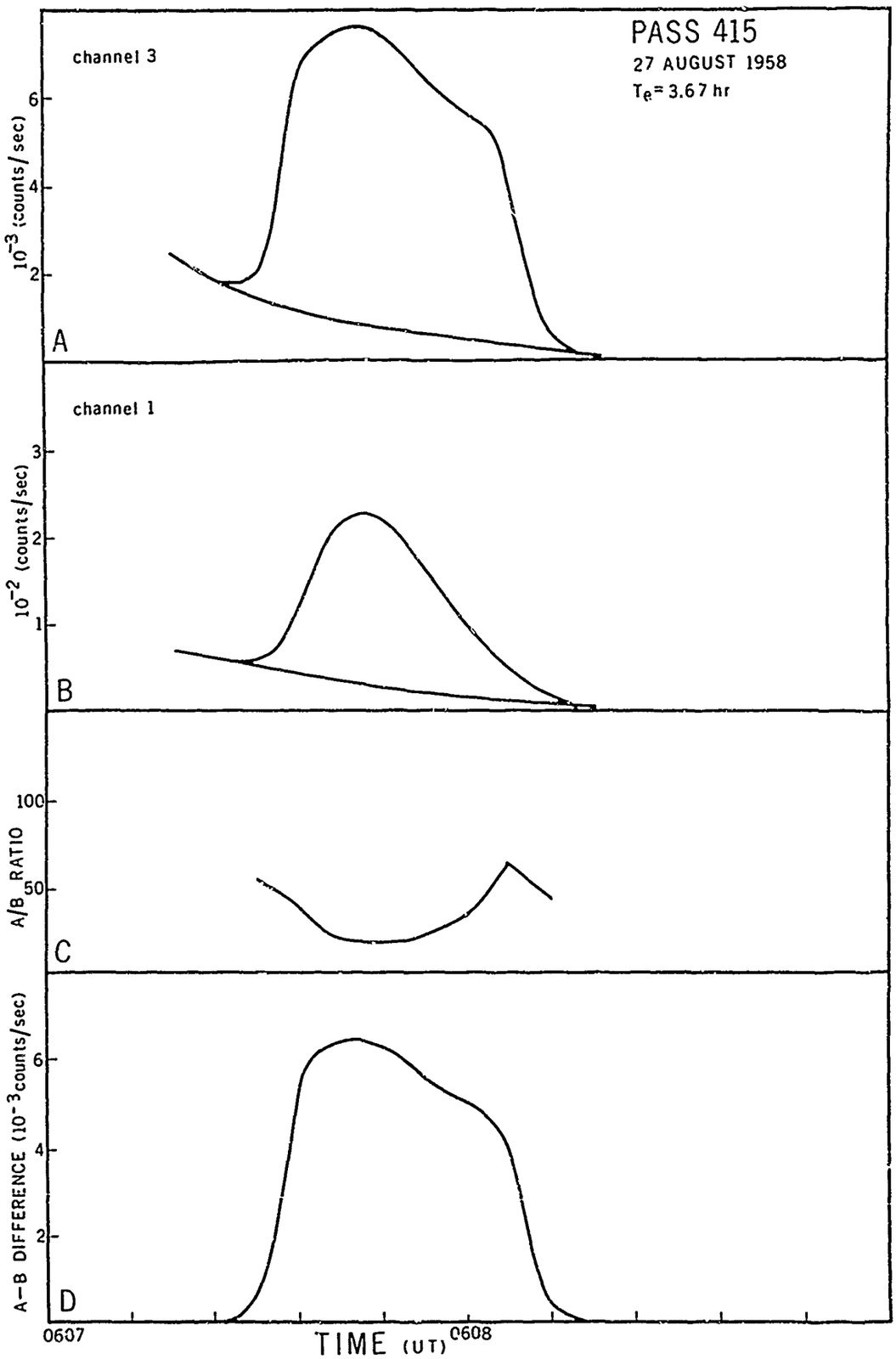
PASS 415
27 AUGUST 1958
T_e = 3.67 hr
channel 3
10^{-3} (counts/sec)
A
channel 1
10^{-2} (counts/sec)
B
A/B RATIO
C
A-B DIFFERENCE (10^{-3} counts/sec)
D
0607
0608
TIME (UT)

Fig. C3. Patn of satellite Explorer 4 in B-L coordinates. The regions of ARGUS Events 1 and 2 are shown also.

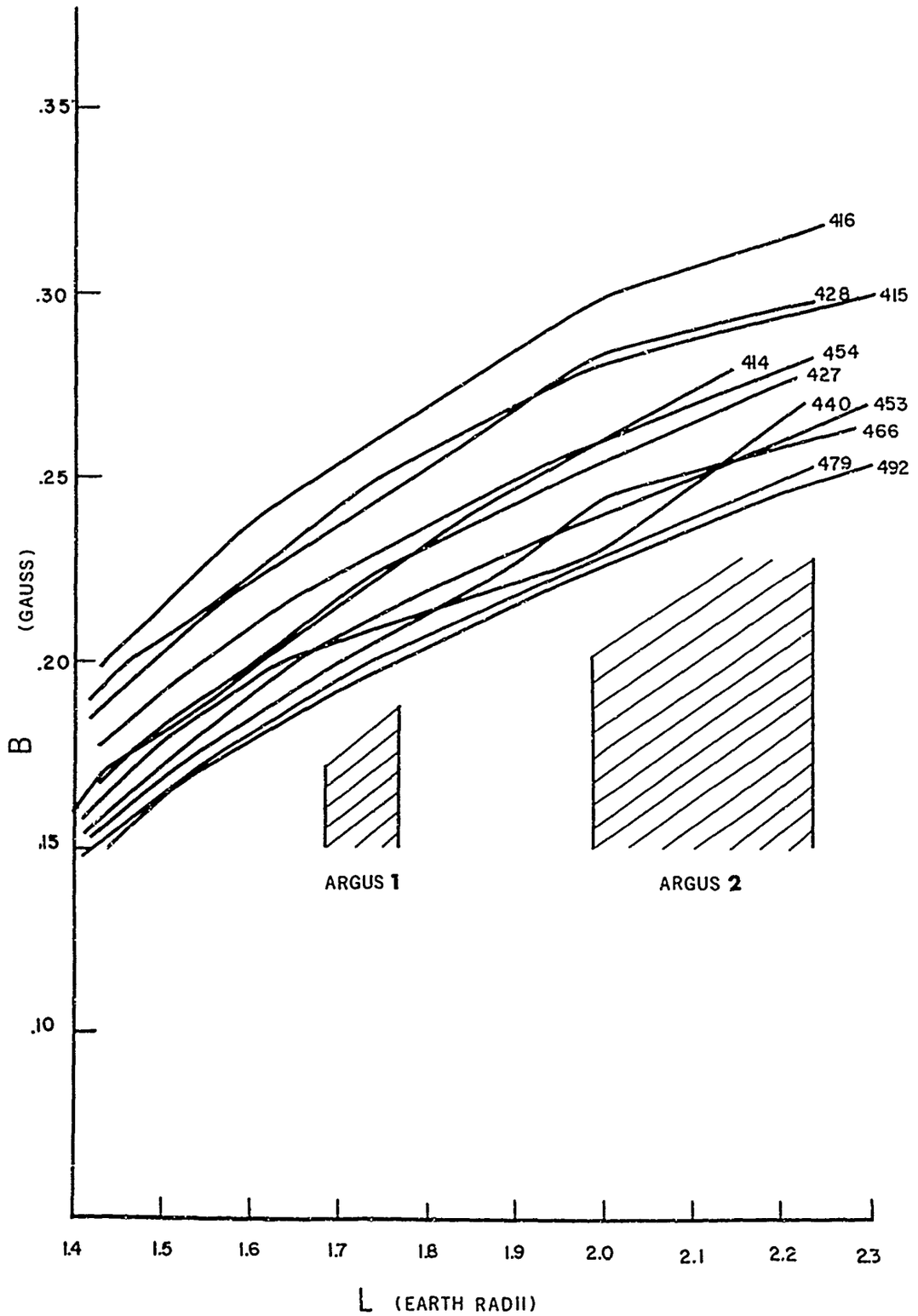
.35
.30
.25
.20
.15
.10
B (GAUSS)
416
428
415
414
454
427
440
453
466
479
492
ARGUS 1
ARGUS 2
1.4
1.5
1.6
1.7
1.8
1.9
2.0
2.1
2.2
2.3
L (EARTH RADII)

Fig. C4. Planetary magnetic three-hour range K_p indices during the time interval of ARGUS Events 1 and 2.

PLANETARY THREE-HOUR-RANGE INDICES K_p (1958)

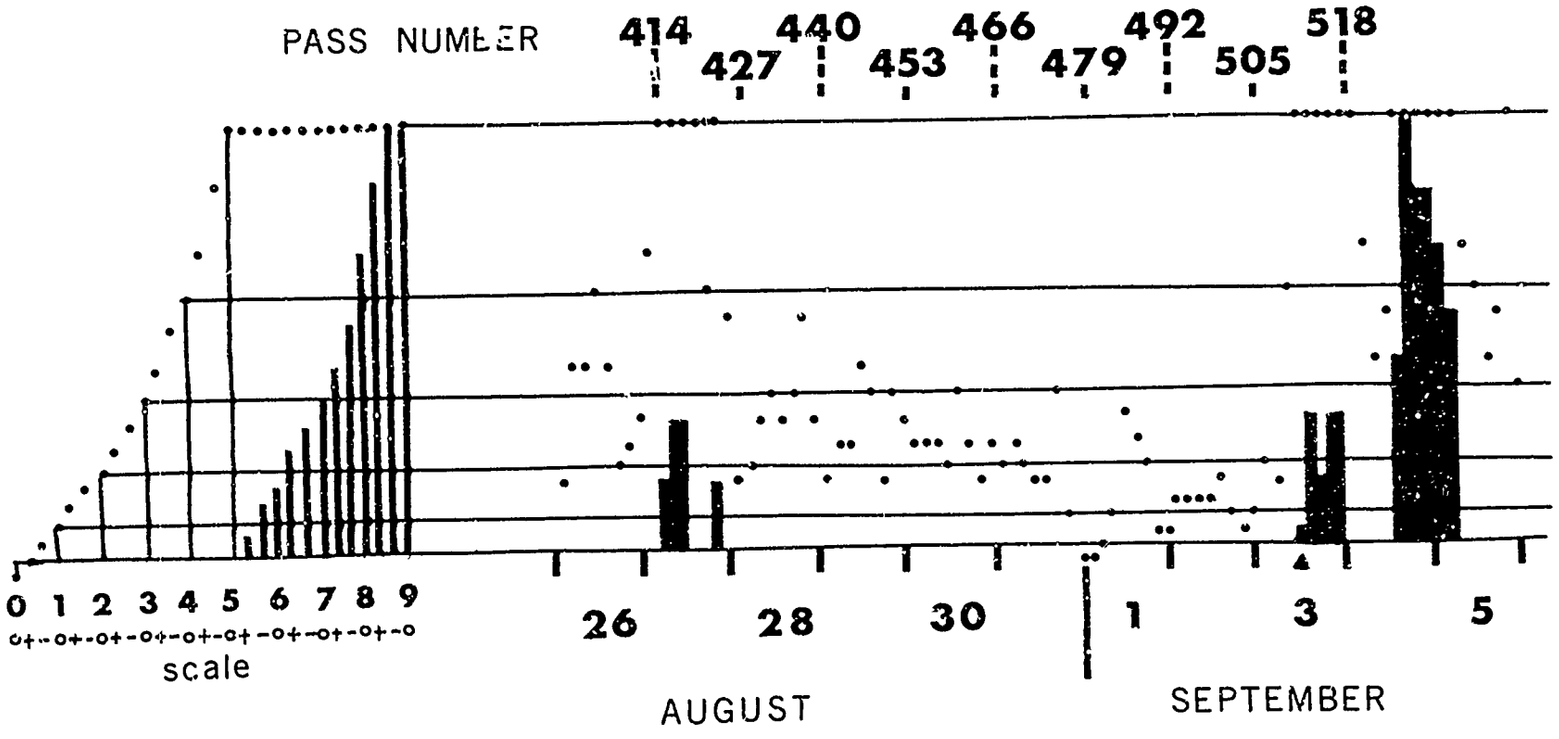

▲ sudden commencement

Fig. C5. Logarithmic plot of true count-rate of the unshielded G-M counter (Detector C, Channel 3) versus the elapsed time since detonation of ARGUS Event 1. The solid lines are least squares fit of Eq. (C3) for the data of the sequence of Passes 414, 427, ... 518. n = 1.13 for both curves. Intersection of the two straight lines with the ordinate axis yield values of C_o, Eq. (C3). The peak intensities were centered at L = 1.72.

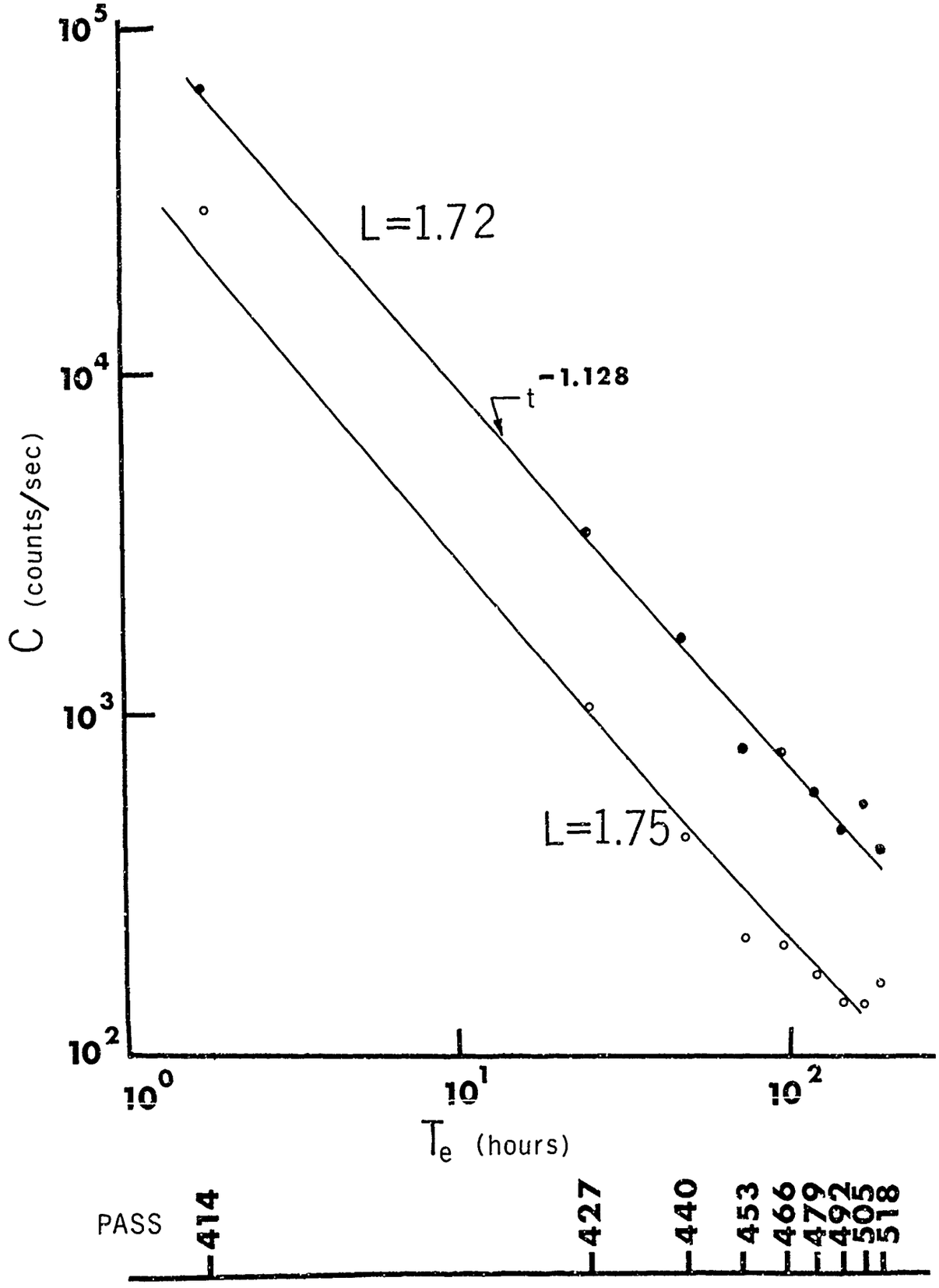
10^5
10^4
10^3
10^2
C (counts/sec)
L=1.72
$t^{-1.128}$
L=1.75
10^0
10^1
10^2
T_e (hours)
PASS
414
427
440
453
466
479
492
505
518

Fig. C6. Count-rate ratio, unshielded (Channel 3)/shielded (Channel 1) omnidirectional G-M counters versus elapsed time T_e since ARGUS Event 1. Both G-M count-rates were corrected for background count-rates. The dashed line is the plot of $C = C_o t^{-1.13}$, Eq. (C3).

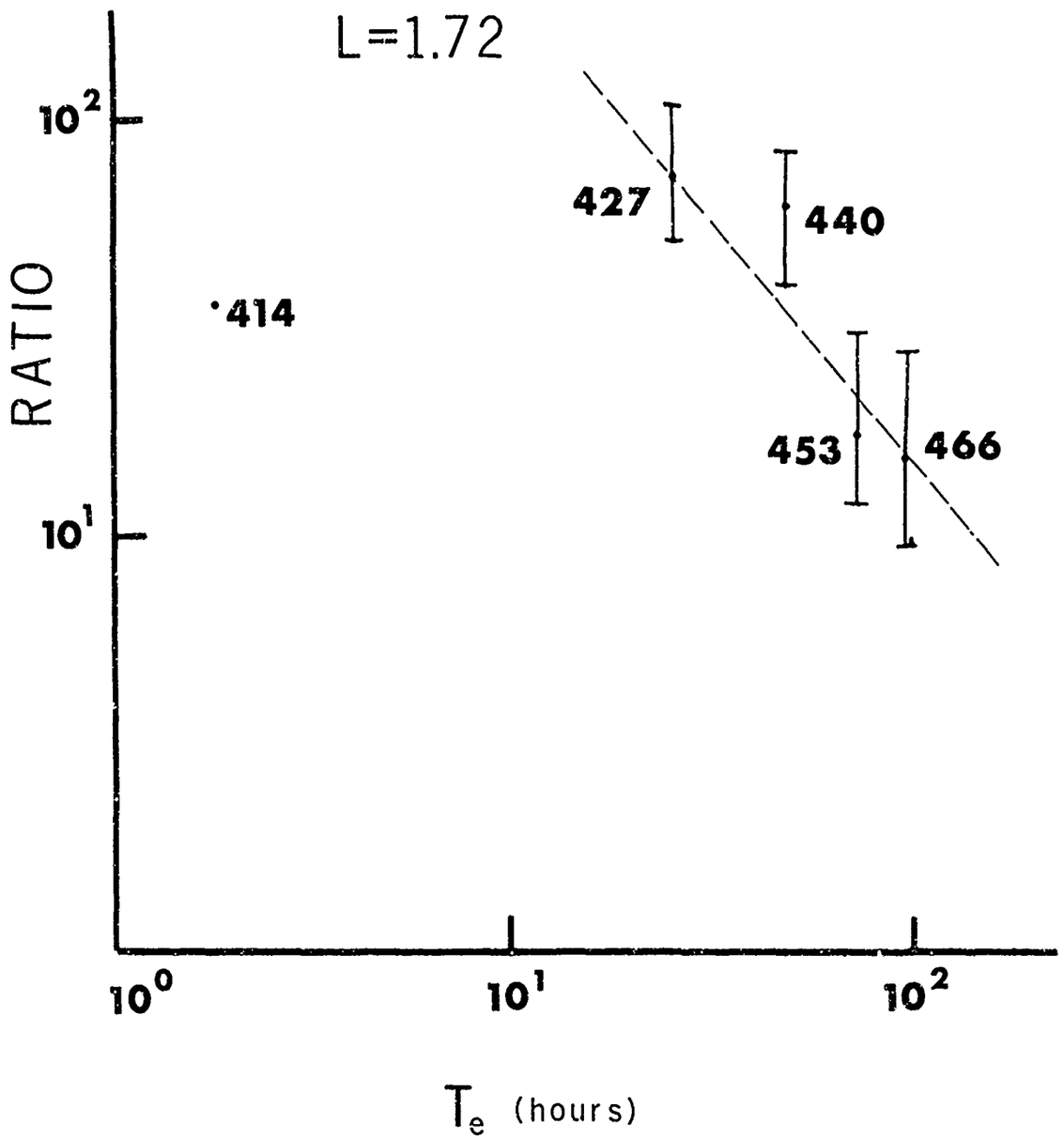
L=1.72
RATIO
10^2
10^1
10^0
10^1
10^2
427
440
414
453
466
T_e (hours)

Fig. C7. The geometrical width at half-maximum of the ARGUS Event 1 region versus the elapsed time T_e since the event. (Pass 453 was the first to contain ARGUS Event 2 data.)

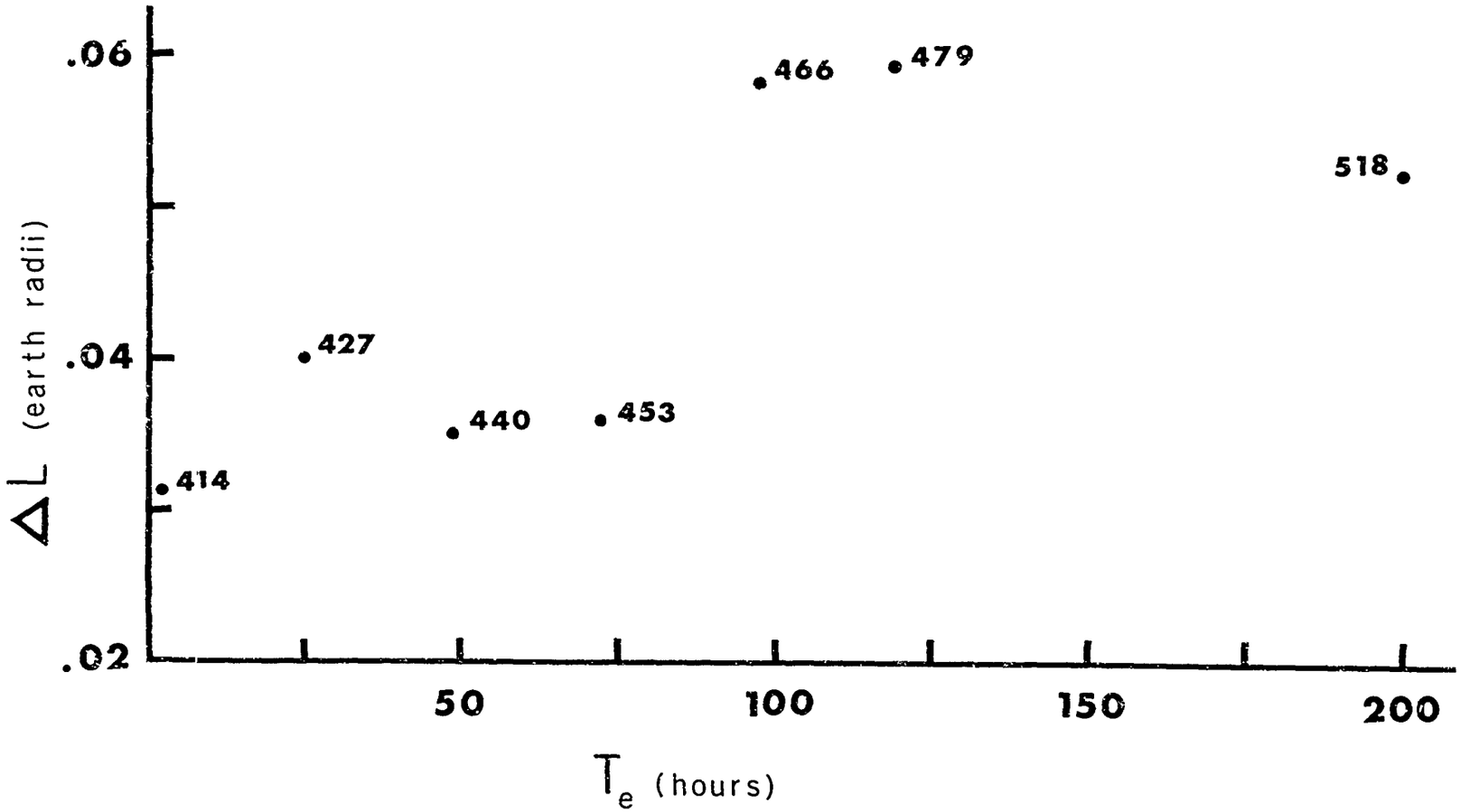
.06
.04
.02
ΔL (earth radii)
466
479
518
427
440
453
414
50
100
150
200
T_e (hours)

Fig. C8. True count-rate of the unshielded (Detector C, Channel 3) G-M counter versus the elapsed time T_e since ARGUS Event 2 for selected L shells.

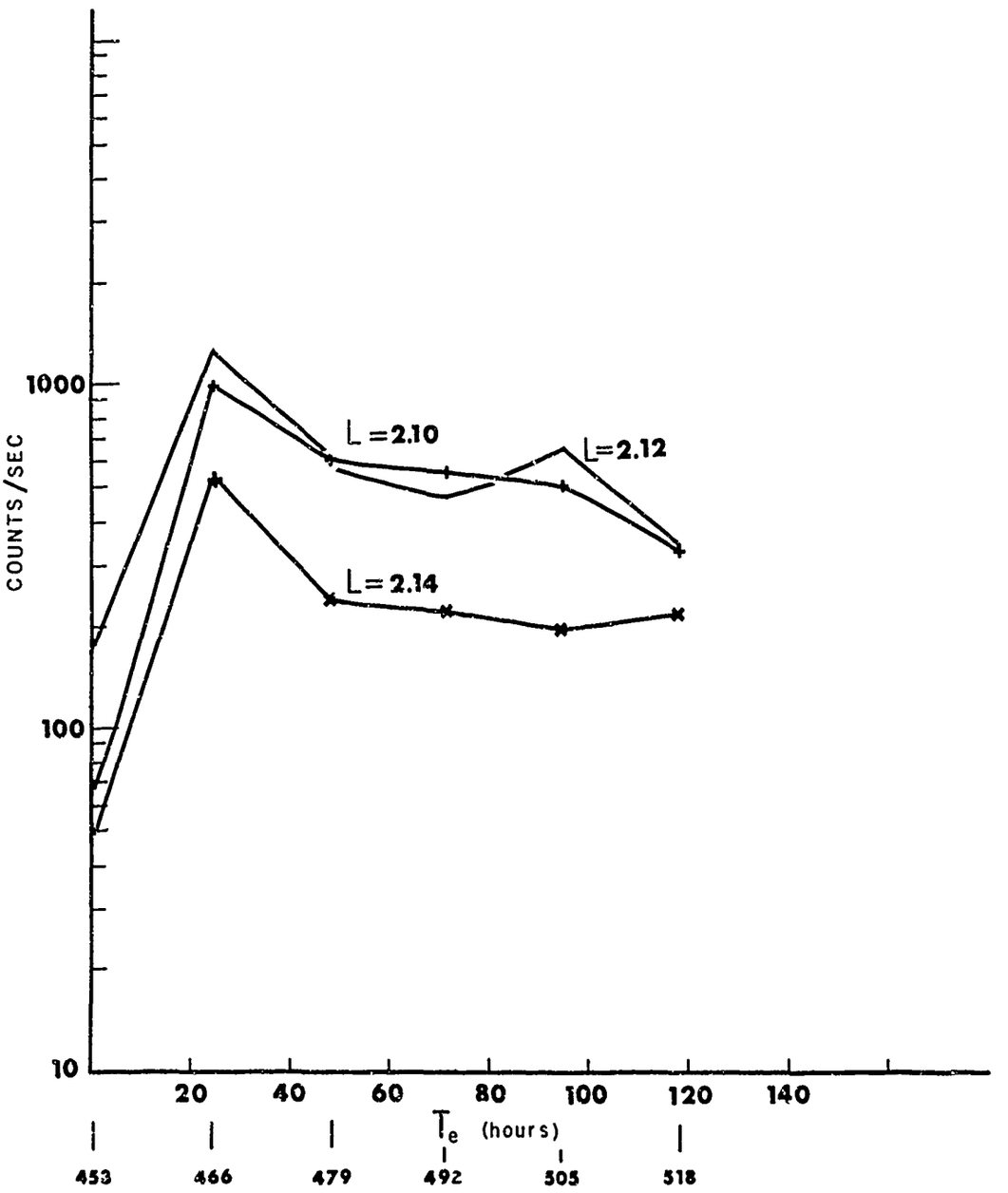
1000
100
10
COUNTS/SEC
L=2.10
L=2.12
L=2.14
20
40
60
80
100
120
140
T_e (hours)
453
466
479
492
505
518

Fig. C9. Logarithmic plot of true count-rate of the unshielded G-M counter (Detector C, Channel 3) vs the elapsed time T_e since ARGUS Event 2 for selected L shells. Passes 505 and 518 were during a period of high magnetic activity.

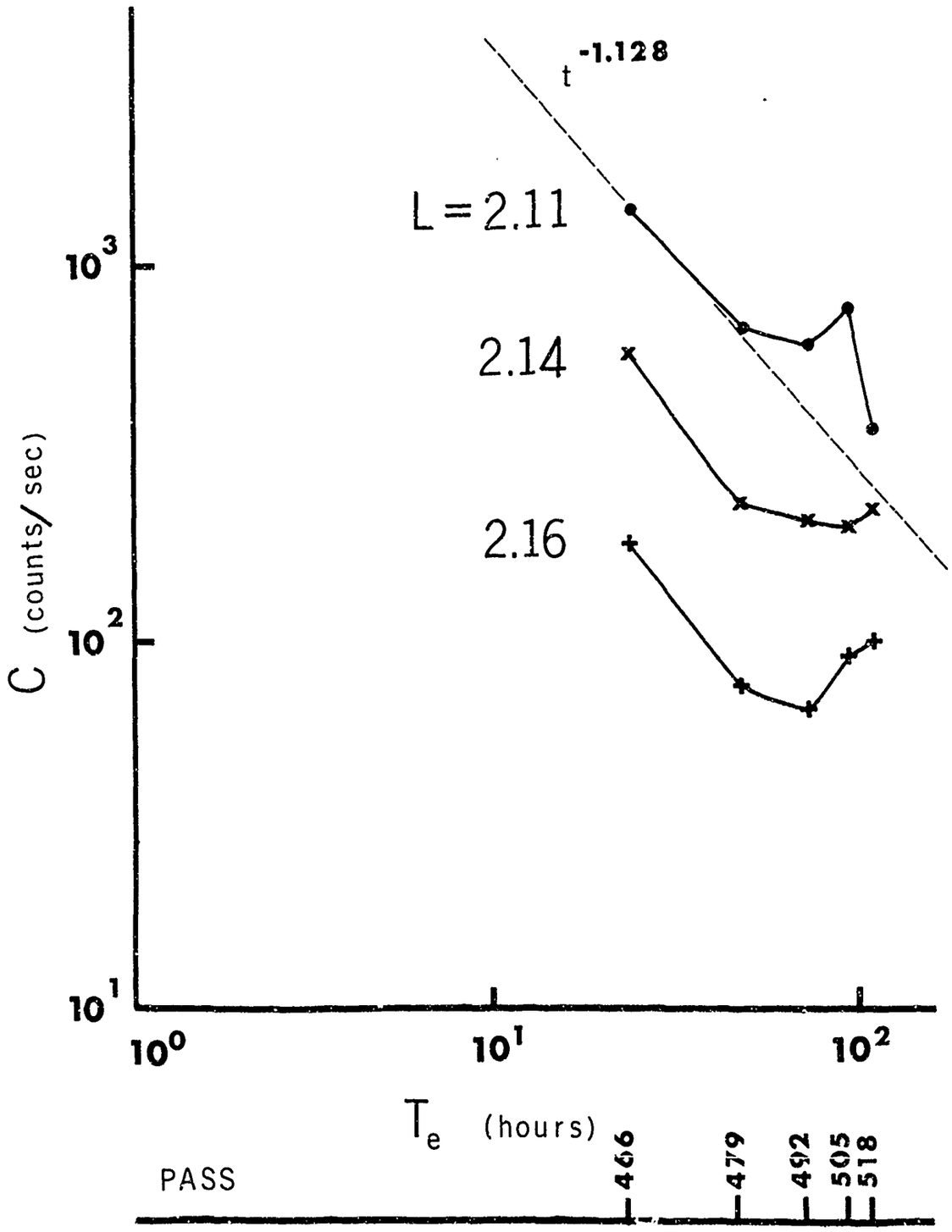
$t^{-1.128}$
L = 2.11
2.14
2.16
10^3
10^2
10^1
C (counts/sec)
10^0
10^1
10^2
T_e (hours)
PASS
466
479
492
505
518

Fig. C10. Count-rate ratio, unshielded (Channel 3)/shielded (Channel 1) G-M counter vs elapsed time T_e since ARGUS Event 2. L = 2.11 is the region of peak intensity of the ARGUS Event 2 region. The numbers above the plotted points are satellite Pass (over Huntsville, Alabama) numbers.

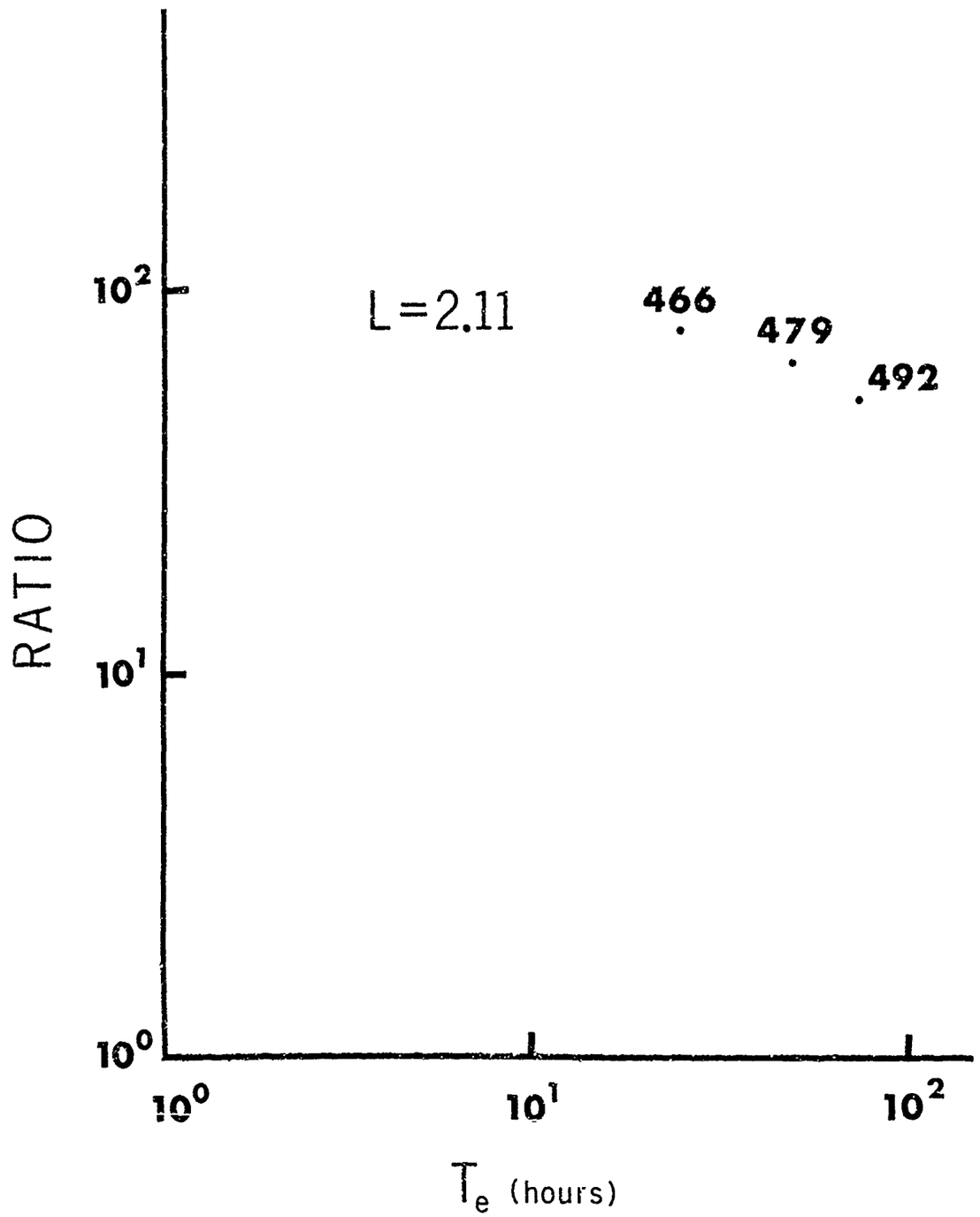
L=2.11
466
479
492
RATIO
10^2
10^1
10^0
10^0
10^1
10^2
T_e (hours)

Fig. C11. Critical energies below which the magnetic moment is conserved in interactions with hydromagnetic waves for particles mirroring at geomagnetic latitudes greater than 30° assuming the hm wave is cut off sharply at ν_{max}. Shown are ν_{max} = 1, 5, and ν_p sec^{-1} (Ref. C19).

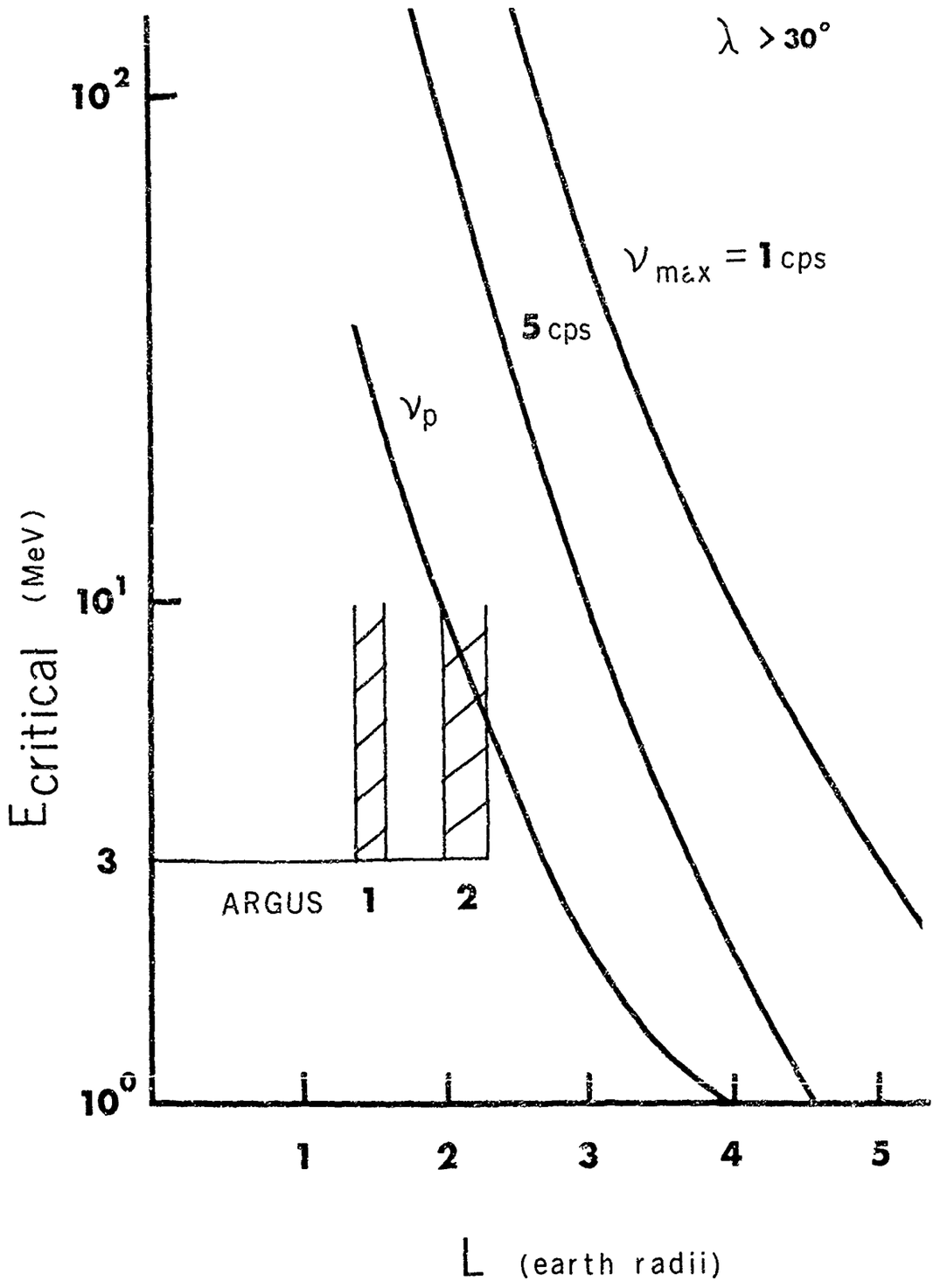
λ > 30°
10^2
10^1
3
10^0
ν_{max} = 1 cps
5 cps
ν_p
ARGUS 1 2
Ecritical (MeV)
1 2 3 4 5
L (earth radii)

Fig. C12. Regions in space where whistlers may be effective in precipitating electrons into the atmosphere. The plot is from Eq. (C4) with the heart of the whistler range being 1 to 10 kc/s (Ref. C20).

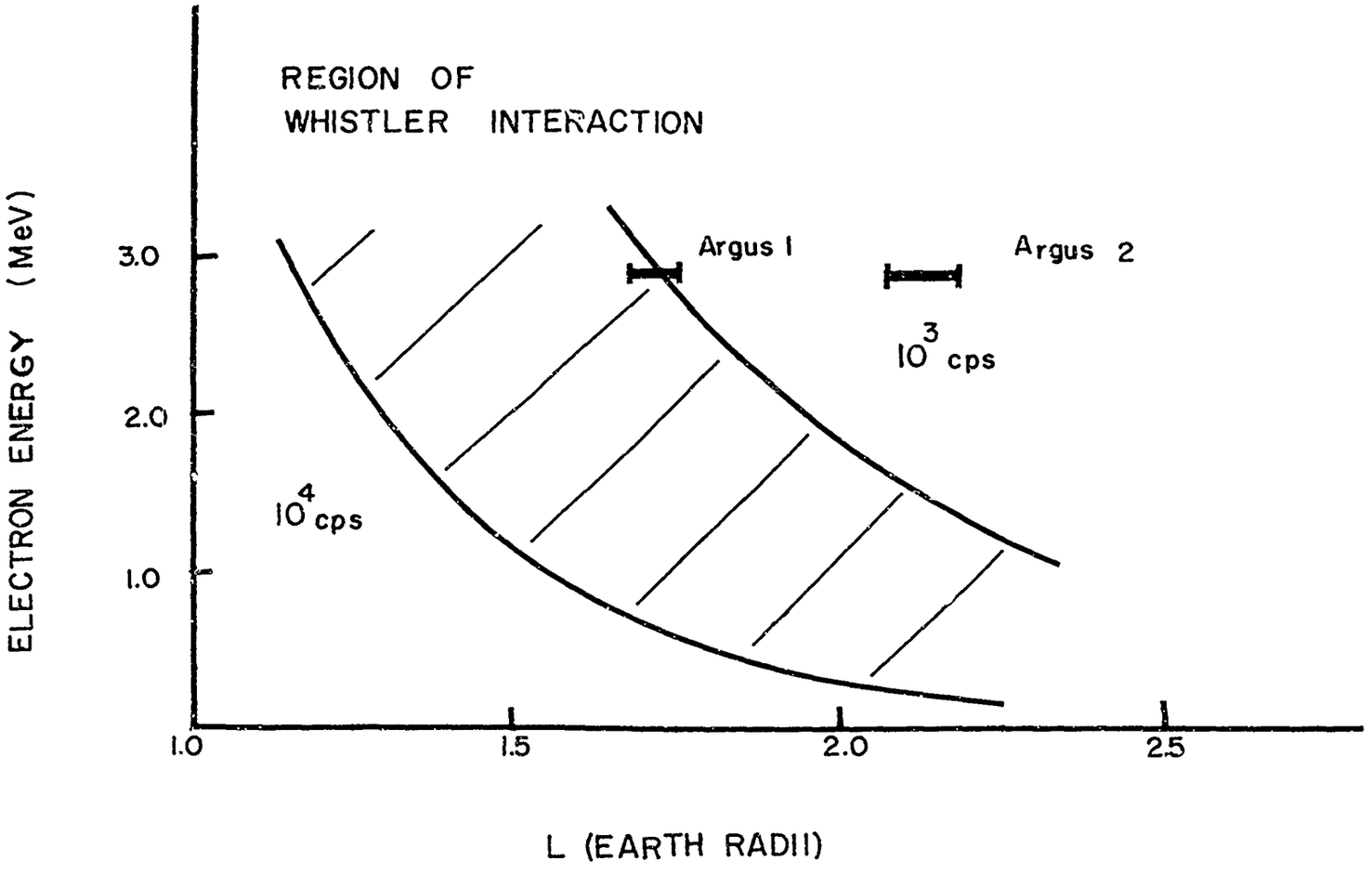
REGION OF
WHISTLER INTERACTION
Argus 1
Argus 2
10^3 cps
10^4 cps
ELECTRON ENERGY (MeV)
3.0
2.0
1.0
1.0
1.5
2.0
2.5
L (EARTH RADII)

Fig. C13. Number of beta rays per fission from U^{235} per energy interval for various energies E in units of $m_o c^2$. The data is taken from Heller (Ref. C24).

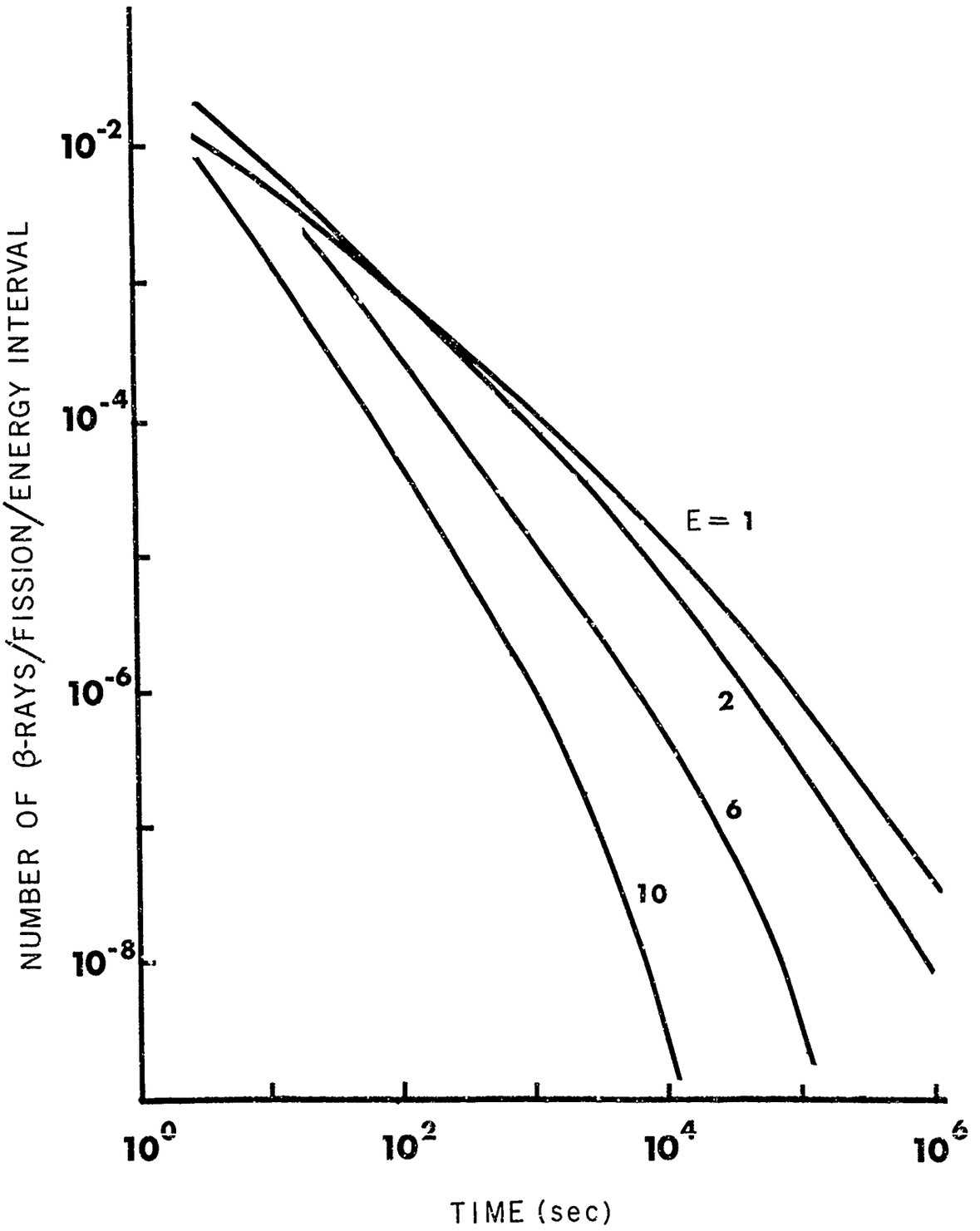
NUMBER OF β-RAYS/FISSION/ENERGY INTERVAL
10^-2
10^-4
10^-6
10^-8
E = 1
2
6
10
10^0
10^2
10^4
10^6
TIME (sec)

Fig. C14. Observed omnidirectional, true initial count-rate C_o contours vs B and L for ARGUS Event 1 (Detector C, unshielded G-M counter, Channel 3). C_o is the true count-rate corrected for decay assuming the $t^{-1.13}$ law, Eq. (C3). The initial time reference for the decay law correction is the beginning of ARGUS shell counting for Pass 427. The solid line count-rate contour curves are best fits to the data from Passes 415, 416, 427, 440, 453, 466, 479 (points not shown).

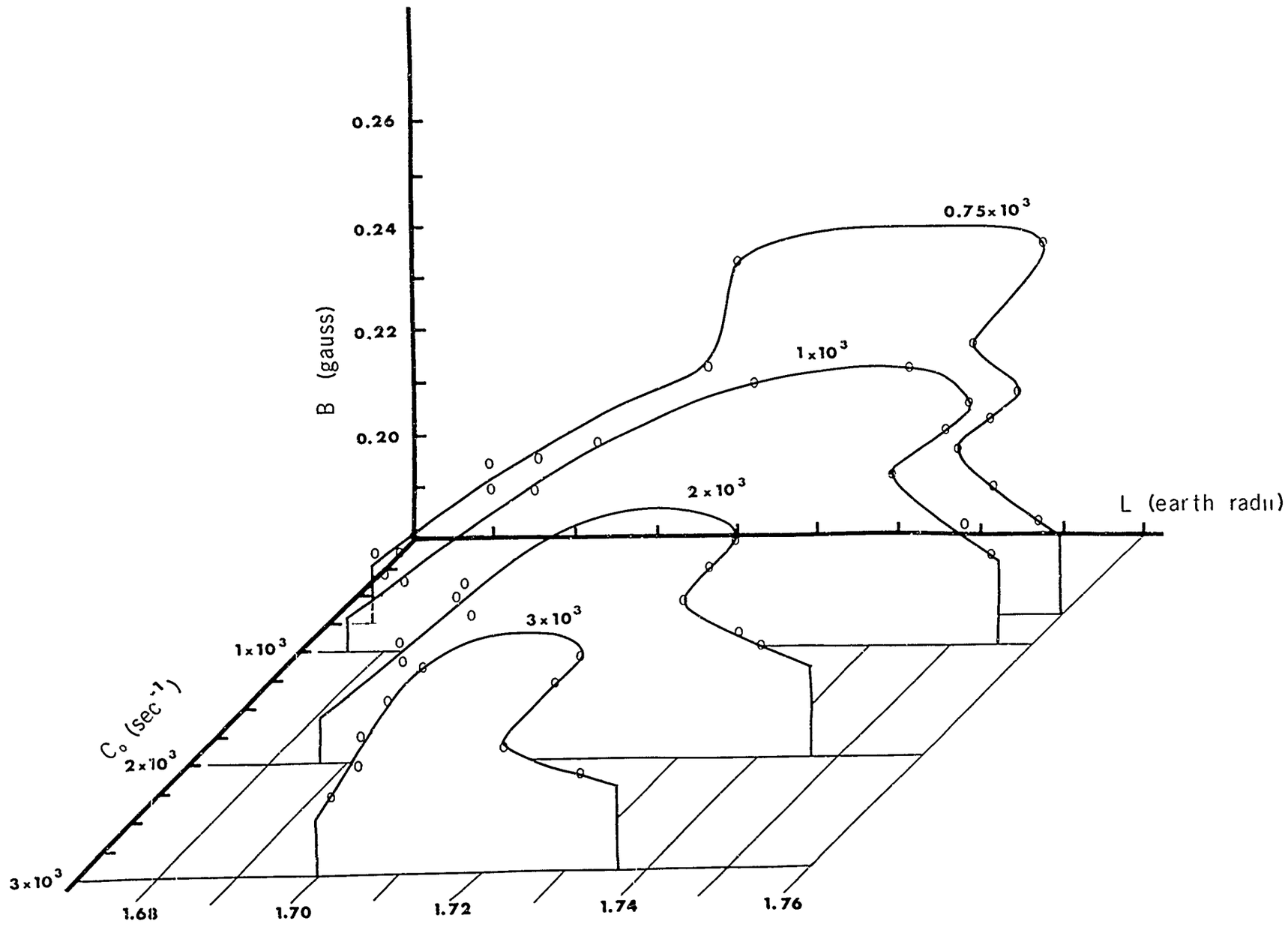
0.26
0.24
0.22
0.20
B (gauss)
0.75×10^3
1×10^3
2×10^3
3×10^3
L (earth radii)
1×10^3
2×10^3
3×10^3
C₀ (sec⁻¹)
1.68
1.70
1.72
1.74
1.76

Fig. C15. Omnidirectional flux density J_o contours vs B and L for ARGUS Event 1 (Detector C, unshielded G-M counter, Channel 3) obtained from the observed omnidirectional true count-rate C_o data (Fig. C14). The conversion is given by $J_o = 67.C_o$.

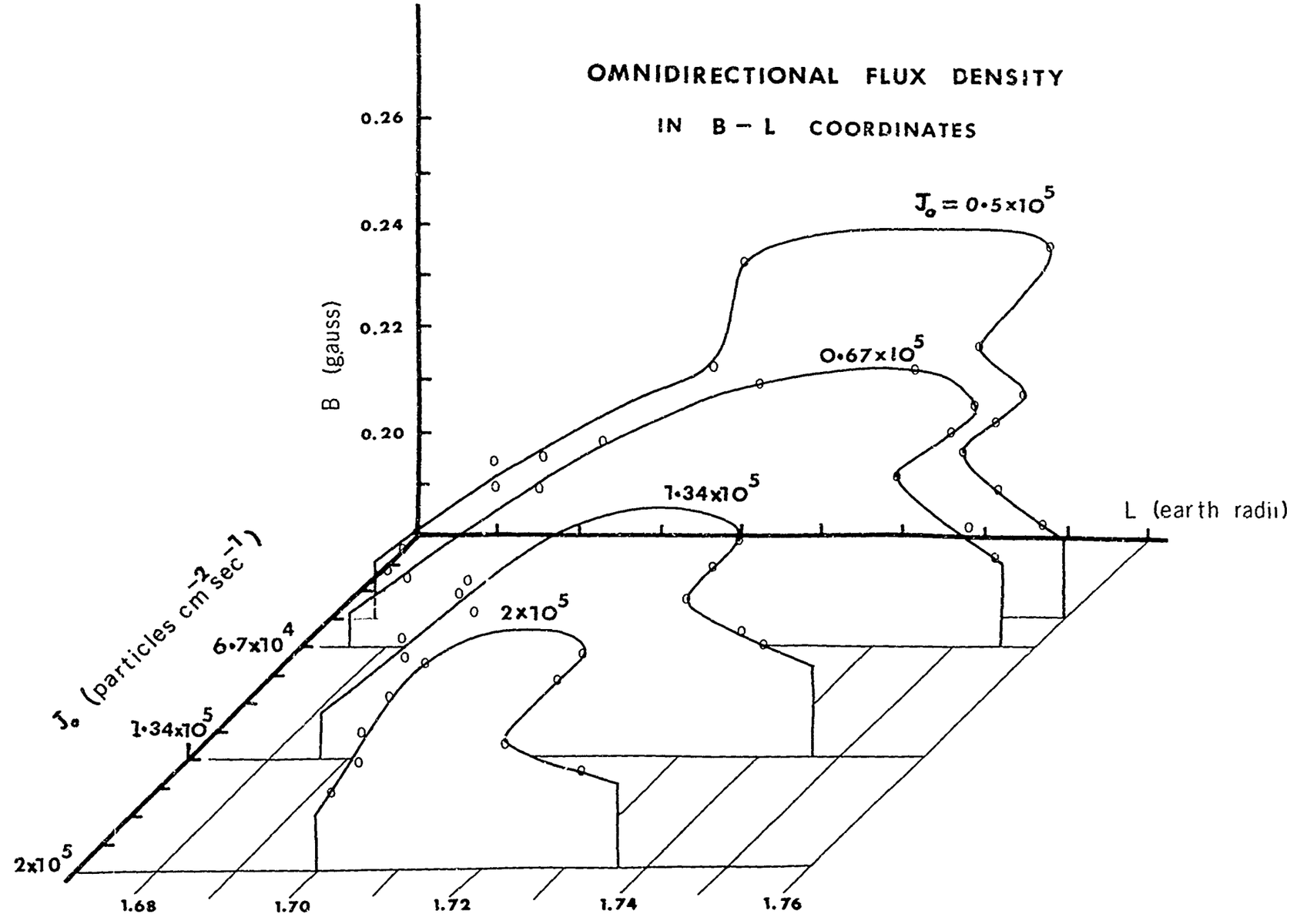
OMNIDIRECTIONAL FLUX DENSITY
IN B – L COORDINATES
B (gauss)
0.26
0.24
0.22
0.20
L (earth radii)
1.68
1.70
1.72
1.74
1.76
$J_o = 0{\cdot}5\times10^5$
$0{\cdot}67\times10^5$
$1{\cdot}34\times10^5$
2×10^5
J_o (particles cm^{-2} sec^{-1})
$6{\cdot}7\times10^4$
$1{\cdot}34\times10^5$
2×10^5

D. Summary of M.S. Thesis, Joseph R. Ockersz, S.J., "Omnidirectional Flux Densities of Geomagnetically Trapped Radiation Explorer 4 Pre-ARGUS Times"; Saint Louis University, Physics Department (May 1966).

D1. Introduction

The purpose of the present Summary is to present experimental aspects of the trapped radiation, including the omnidirectional charged particle flux densities in the geomagnetic field, for pre-ARGUS event times of Explorer 4 Satellite data telemetered over Huntsville, Alabama. Such an investigation is important toward understanding the "background" radiation (natural radiation) against which the artificially injected ARGUS radiation is observed.

D2. Experimental Details

Instrumentation and Calibration of Explorer 4

The University of Iowa group designed the detection instruments. Van Allen has published a complete description of the detection instruments (Ref. D2). Reference D3, Fig. 2.1, p. 16, shows a block diagram of the four detectors A, B, C and D, and the corresponding telemetry channels 2 and 5, 3 and 1. (See also Preface P2, Fig. P2-1).

For the present thesis the omnidirectional count-rates were analysed, involving data obtained by G-M Detectors C and D. Preface P2 of this Report summarizes the characteristics of Detectors C and D. Table D1 lists the telemetry data available for the present analysis and Fig. D1 shows the location of Satellite Explorer 4 for some of the Passes.

The count-rates of the G-M counters must be corrected for

"deadtimes". For detectors C and D, Anton 302 G-M counters, the equation for the correction is

$$C_{obs} = Ce^{-\tau_i C} \qquad (D1)$$

where C_{obs} is the observed count-rate and C is the true or corrected count-rate and τ_i , the deadtime, is 62.5±1.3 microseconds.

Further instrumentation and analysis details are found in DASA Report WT 1613, Ref. (D3).

D3. Results

A complete set of Figures showing the true count-rates vs time for the different B-L regions of the pre-ARGUS Explorer 4 times is found in Ref. Di.

These Ref. D1 Figures are here compactly summarized by three new Figs. D2 (constant omnidirectional count-rate contours in B-L coordinates), D3 (omnidirectional flux densities vs B), D4 (three dimensional plots of omnidirectional true count-rates vs B and L).

The slope of Log(J_o) vs Log(B) straight line (derived from Fig. D4) compares closely with earlier published results (Ref. D4). In general it has been found (Ref. D1) that Passes 2, 13, 26, 52, 78, 107, 173, 207 and 367 recorded small flux densities, between 10 and 30 particles $cm^{-2}sec^{-1}$; while passes 4, 43, 121, 272, 285, 298, 311, 324, 337, 375 and 401 recorded large flux densities between 100 and 20,000 particles $cm^{-2}sec^{-1}$. Passes of small measured flux densities correspond to low altitude (250 < altitude < 700 km). The low count-rates are due chiefly to non-trapped cosmic radiation in space. The Passes of

larger measured altitudes (1000 < altitude < 1500) are specified by $0.17 < B < 0.30$, $1.35 < L < 1.65$ and $0.35 < B < 0.45$, $3.5 < L < 5.5$. The larger omnidirectional flux densities were recorded in the Van Allen region.

D4. References

D1. Ockersz, S.J., Joseph, M.S. Thesis, "Omnidirectional Flux Densities of Geomagnetically Trapped Radiation Explorer 4 Pre-ARGUS Times", 6 May 1966.

D2. Van Allen, J. A., McIlwain, C. E. and Ludwig, G. H., "Radiation Observations with Satellite 1958 Epsilon", US/IGY Project 32.1 of the National Academy of Sciences and the National Science Foundation; by the U. S. Army Ordnance Department; and by the Office of Naval Research and the Atomic Energy Commission.

D3. DASA Report 1613, "Analysis of ARGUS/Explorer 4 Records", by A. H. Weber, et al, Physics Department, Saint Louis University, St. Louis, Missouri, 15 January 1965.

D4. Lundquist, C. A., Naumann, R. J., and Weber, A. H., J. Geophys. Res. 67, 4125-4133 (1962); "Directional Flux Densities and Mirror Point Distributions of Trapped Particles from Satellite 1958 Epsilon Measurements".

Fig. D1 Map showing location of Satellite 1958€(Explorer 4) for Passes 2, 4, 13, 26, 43, 52, 63, 78, 107, 121, 172, 207, 272, 285, 298, 311, 324, 337, 367, 375, 401 and 414 tracked by the U. S. Army Tracking Station at Huntsville, Alabama. Except for Pass 414, these Passes are for pre-ARGUS times. The number in parenthesis is the Pass number, the other numbers are the satellite altitudes at the beginning and end of the tracking period for the Pass.

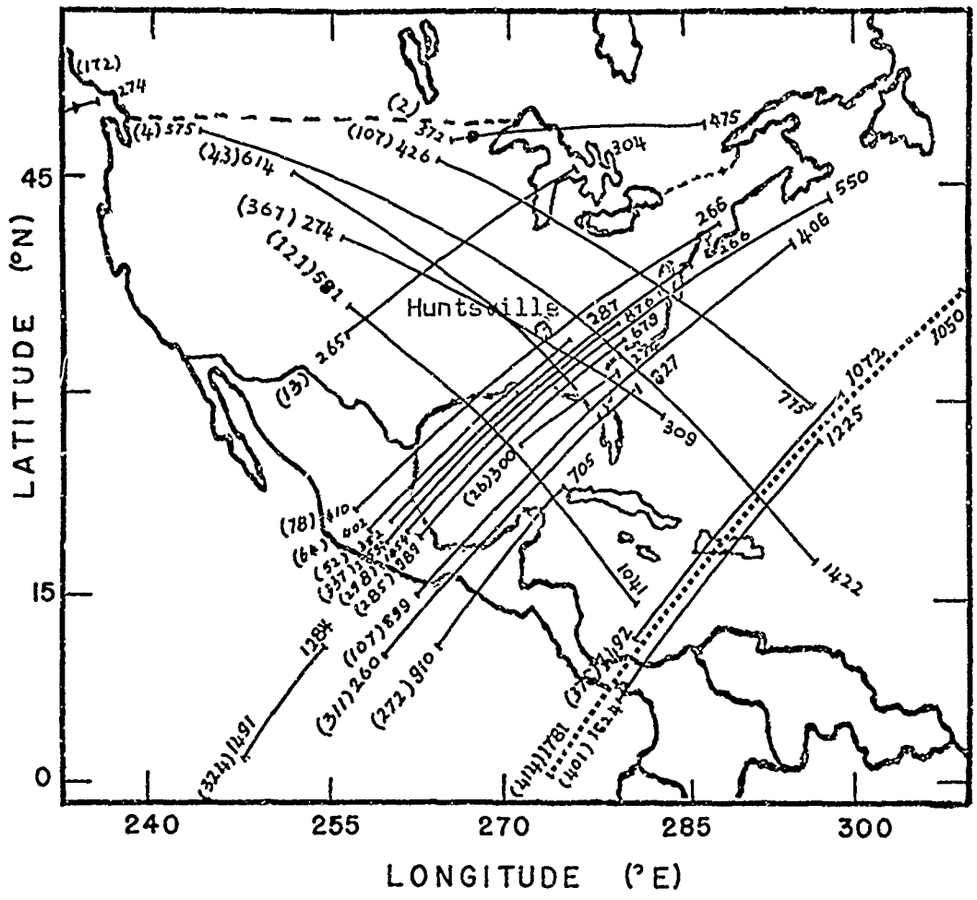
Huntsville
LATITUDE (°N)
LONGITUDE (°E)
45
15
0
240
255
270
285
300

Fig. D2 Omnidirectional true constant count-rate contours in B-L coordinates. Data is for pre-ARGUS times, shielded G-M detector D (channel 1) for the region defined by $1.27 < L < 1.30$ and $0.20 < B < 0.23$. To obtain J_0, the true omnidirectional count-rates are multiplied by 8.4*, a reduction constant derived from the calibration of the detector. (*provisional, subject to correction)

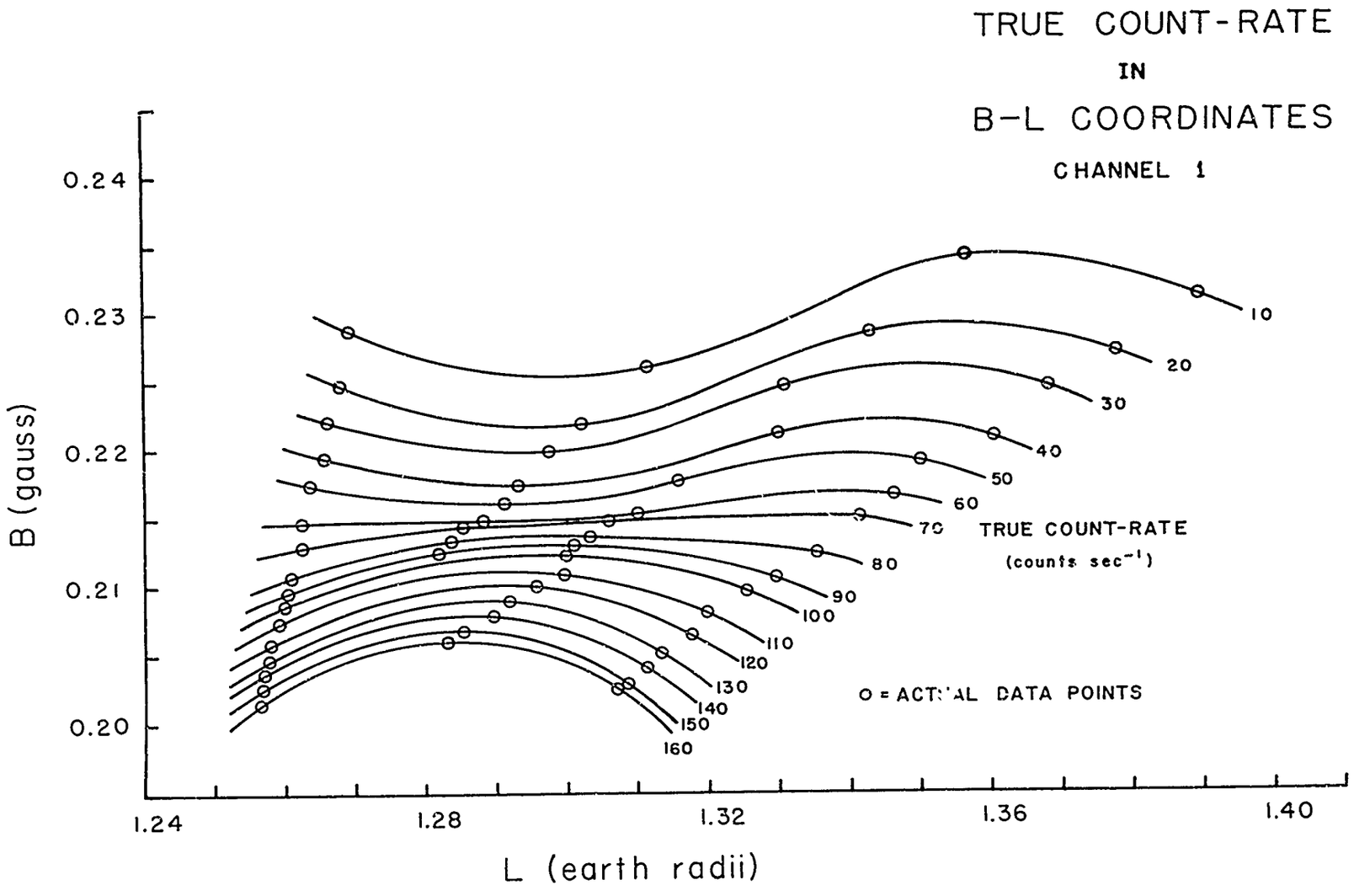
TRUE COUNT-RATE
IN
B-L COORDINATES
CHANNEL 1
B (gauss)
0.24
0.23
0.22
0.21
0.20
1.24
1.28
1.32
1.36
1.40
L (earth radii)
10
20
30
40
50
60
70
80
90
100
110
120
130
140
150
160
TRUE COUNT-RATE
(counts sec⁻¹)
O = ACTUAL DATA POINTS

Fig. D3 Omnidirectional flux densities vs magnetic flux density B. Data is for pre-ARGUS times, shielded G-M detector D (channel 1) for the region defined by $0.20 < B < 0.23$ and $1.27 < L < 1.30$. Log J_0 vs B is plotted instead of log J_0 vs log B in order to obtain somewhat greater spread in data. The data may be represented by the equation $J_0 = k\ B^n$, whence $n = 30$, approximately.

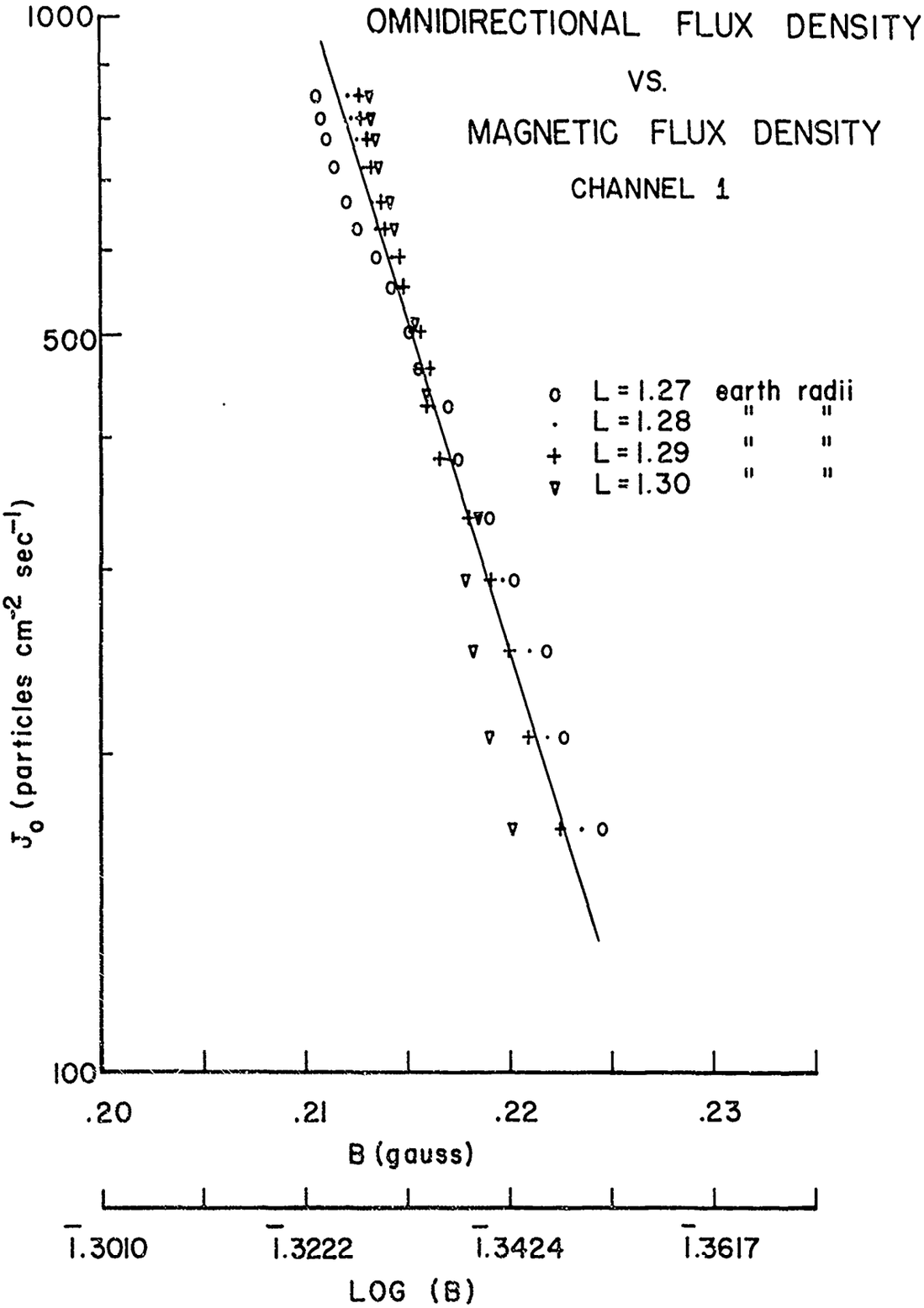
OMNIDIRECTIONAL FLUX DENSITY
VS.
MAGNETIC FLUX DENSITY
CHANNEL 1
o L = 1.27 earth radii
· L = 1.28 " "
+ L = 1.29 " "
▽ L = 1.30 " "
1000
500
100
J_o (particles cm^{-2} sec^{-1})
.20
.21
.22
.23
B (gauss)
$\bar{1}$.3010
$\bar{1}$.3222
$\bar{1}$.3424
$\bar{1}$.3617
LOG (B)

Fig. D4 Three dimensional plot of omnidirectional true count-rates C (shielded G-M counter, Detector D, channel 1) (number sec^{-1}) vs B and L. Sheets of constant L are shown intersecting the contours of constant count-rates. Data is the same as for Figs. D2 and D3.

CHANNEL 1

TRUE COUNT-RATE

on B-L (three dimensional)

PRE-ARGUS

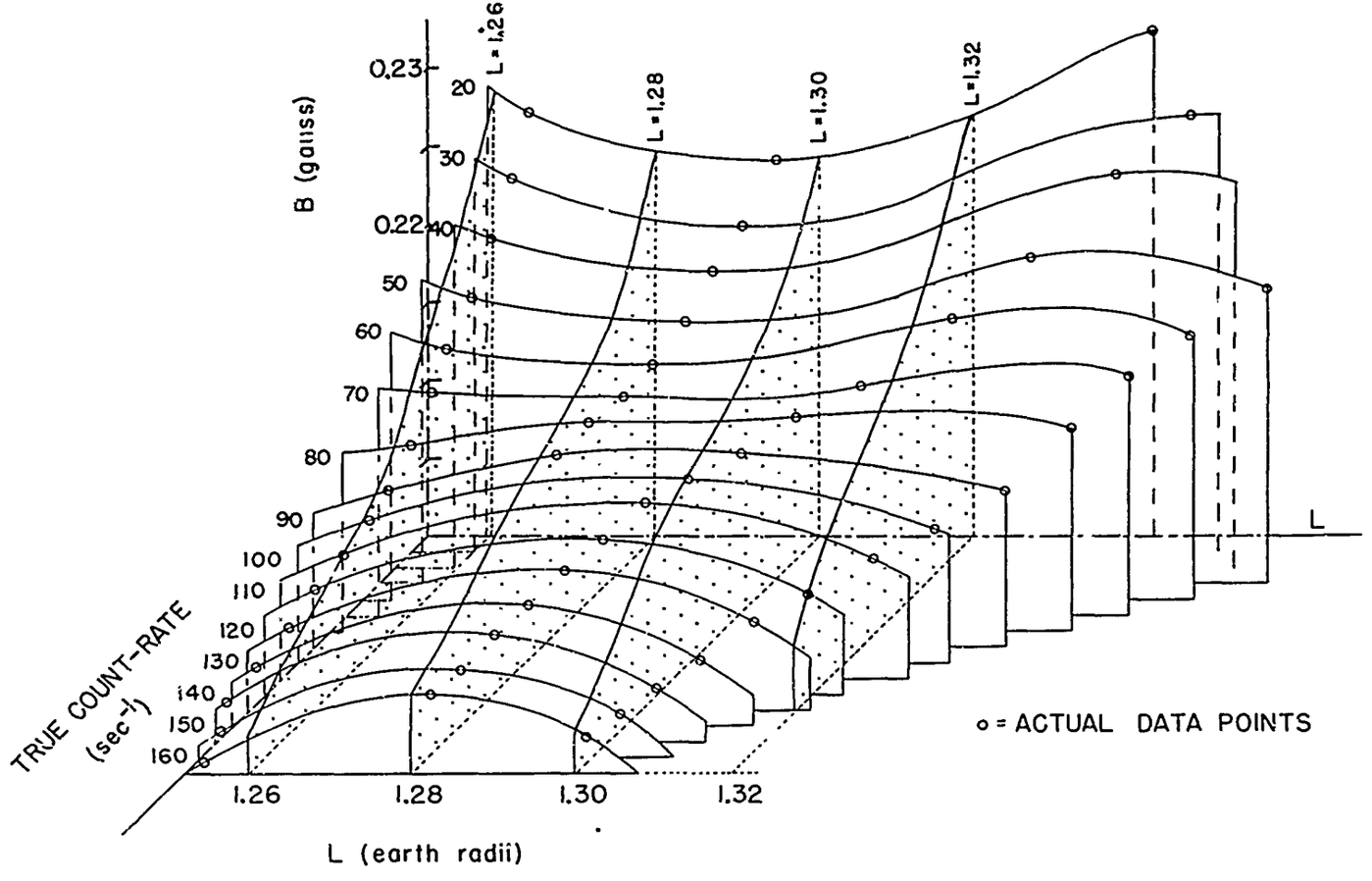

Table D1. Explorer 4 telemetry, pre-ARGUS times data available at Saint Louis University, Physics Department; Passes are over Huntsville, Alabama Tracking Station.

Pass No.	Date	Time
1	July - 26	1658-1702
2	26	1855-1858
3	26	2054-2057
4	26	2240-2257
5	July - 27	0036-0042
13	27	1650-1655
15	27	1848-1851
16	27	2042-2052
17	27	2240-2247
26	July - 28	1449-1451
27	28	1642-1648
28	28	1840-1844
42	July - 29	2026-2035
43	29	2220-2227
52	July - 30	1430-1437
53	30	1627-1632
64	July - 31	1421-1426
66	31	1618-1622
67	31	1816-1818
69	31	2205-
70	Aug. - 1	0000-0007
77	1	1220-1222
78	1	1412-1420
79	1	1609-1614
80	1	1806-1811
81	1	2001-2008
82	1	2154-2208
94	Aug. - 2	1951-1957
104	Aug. - 3	-0841
107	3	1941-1949
108	3	2130-2141
109	3	2331-2335
121	Aug. - 4	2125-2134
122	4	2321-2327
133	Aug. - 5	1921-1927
134	5	2113-2126
147	Aug. - 6	2200-2210
148	6	1257-1305
169	Aug. - 7	1257-1305
172	Aug. - 8	1845-1852
173	8	2039-2050
182	Aug. - 9	1243-1249
189	9	1820-1828

Pass No.	Date	Time
199	Aug. - 10	2015-2025
207	11	1025-1035
208	11	1220-1228
220	Aug. - 12	1010-1021
221	12	1807-1815
222	12	1405-
224	12	1754-1801
225	12	1948-1957
233	Aug. - 13	0957-1008
234	13	1153-1202
237	13	1741-1748
238	13	1935-1943
246	Aug. - 14	0950-0953
247	14	1139-1149
250	14	1725-1734
251	14	1923-1929
259	Aug. - 15	0924-0938
260	15	1125-1132
264	15	1907-1915
272	Aug. - 16	0910-0920
273	16	1107-1118
276	16	1657-1705
277	16	1852-1858
285	Aug. - 17	0855-0906
286	17	1056-1102
298	Aug. - 18	0840-0854
302	18	1627-1633
310	Aug. - 19	0630-0642
311	19	0823-0833
312	19	1022-1032
313	19	1611-1617
324	Aug. - 20	0836-0809
325	20	1004-1015
328	20	1555-1602
337	Aug. - 21	0748-0806
338	21	0949-0959
341	21	1538-1544
355	Aug. - 22	1521-1527
367	Aug. - 23	1503-1510
375	Aug. - 24	0510-0518
401	Aug. - 26	0433-0440
406	26	1408-1414
413	26	2225-2259

E. Summary of Pertinent Analytic Sections of Ph.D. Dissertation, Joseph M. Paikeday, "Interpretation of Directional Flux Densities in ARGUS Shells, Explorer 4 Satellite Data"; Saint Louis University, Physics Department (March 1966).

E1. Introduction

The method used for obtaining the directional flux density $J(\theta')$ (particles $cm^{-2}sec^{-1}ster^{-1}$; θ', angle between scintillation counter axis $\hat{P}$ and $\vec{J}$) follows that of Lundquist, Naumann, and Weber (Ref. E1) in the reduction of the integral equation relating the corrected directional count-rate $C(\theta)$ (number $cm^{-2}sec^{-1}$) and $J(\theta')$ to matrix form (θ, angle between $\hat{P}$ and a plane perpendicular to the magnetic flux density vector B). The matrix elements S_{ij} (Ref. E2, p. 13) associated with the response function have been evaluated to a greater accuracy resulting from a more precise definition in the present analysis of the limits of integration in the integral equation relating $C(\theta)$ and $J(\theta')$ (Ref. E2, Eq. (1.6)). It has been found that the kernel of this integral equation has a vanishingly small determinant and as a consequence established methods of solving the integral equation for $J(\theta')$ values fail to produce physically meaningful results. The kernel of this integral equation is highly sensitive to experimental errors inherent in the $C(\theta)$ data. The present method replaces the inverse of the kernel matrix by an approximate matrix (Ref. E2, Eq. (1.26)) which is insensitive to small errors in the counting rate data.

E2. Summary of the Analytic Procedure

The complete details of the analytic procedure outlined in E1 above are given in the Paikeday Ph.D. Dissertation (Ref. E2). The procedure involves the following steps:

(1) Reduction of the integral equation to a matrix form (see Ref. E2 pp. 7-13).

(2) Representation of the directional scintillation detector (Detector A, Channel 2) response function $S(\alpha)$ (Ref. E2, Fig. 1.2, p. 149) in analytic form (see Ref. E2, Eq. (1.10)) to yield $J(\theta')$ values.

(3) Inversion of the matrix equation (see Ref. E2, pp. 14-33).

E3. Conclusions

With the data available as discrete points of the $C(\theta)$ function, the solutions obtained by using the inverse of the S-matrix are found to be non-physical. The process of getting correct physical solutions does not in any way remove the ill-conditioning of the original matrix S representing the kernel of the integral equation but rather supplies information about the type of errors that enter the counting rate data.

The method developed in the present analysis is found to yield meaningful $J(\theta')$ values for the available $C(\theta)$ data.

E4. References

E1. Lundquist, C., Naumann, R., and Weber, A. H., "Directional Flux Densities and Mirror Point Distributions of Trapped Particles from Satellite 1958 Epsilon Measurements", J. Geophys. Res. 67, 4125-4133 (1962).

E2. "Interpretation of Directional Flux Densities in ARGUS Shells, Explorer 4 Satellite Data", Ph.D. Dissertation, J. M. Paikeday, Saint Louis University, St. Louis, Missouri, 1 March 1966.

Security Classification

DOCUMENT CONTROL DATA - R&D

(Security classification of title, body of abstract and indexing annotation must be entered when the overall report is classified)

1. ORIGINATING ACTIVITY (Corporate author)	2a. REPORT SECURITY CLASSIFICATION
Defense Atomic Support Agency, Department of Defense	Unclassified
	2b GROUP

3. REPORT TITLE

"FURTHER DETAILED ANALYSIS OF TELEMETRY RECORDS OBTAINED BY EXPLORER IV SATELLITE CONCERNING GEOMAGNETICALLY TRAPPED RADIATION"

4. DESCRIPTIVE NOTES (Type of report and inclusive dates)

1 November 1965 through 30 November 1966

5. AUTHOR(S) (Last name, first name, initial)

Weber, Alfred H., Brisken, Axel F., Coughlin, Michael E., Fennell, Joseph F., George, John A., Kottmeyer, William K., Manson, Donald J., Ockersz, Joseph R., S.J., Paikeday, Joseph M.

6. REPORT DATE	7a. TOTAL NO. OF PAGES	7b. NO. OF REFS
30 November 1966	113	49

8a. CONTRACT OR GRANT NO.	9a. ORIGINATOR'S REPORT NUMBER(S)
DA-49-146-XZ-494	
b. PROJECT NO.	DASA Report No. 1889
c.	9b. OTHER REPORT NO(S) (Any other numbers that may be assigned this report)
d.	DASA Report No. 1889

10. AVAILABILITY/LIMITATION NOTICES

Distribution of this Document is Unlimited

11. SUPPLEMENTARY NOTES	12. SPONSORING MILITARY ACTIVITY
None	Department of Defense Defense Atomic Support Agency

13. ABSTRACT

This report (Preface P1, P2; Parts A-E) is essentially a Summary of the five M.S. Theses and Ph.D. Dissertations completed during the contract year for contract No. DA-49-146-XZ-494. The titles of these theses and dissertations are the heading titles for each of the five Parts A-E.

A. Summary of Ph.D. Dissertation, Donald J. Manson, "Van Allen Radiation Belt and ARGUS Directional Flux Density Distributions, Explorer 4, Satellite Data", Saint Louis University, Physics Department, February 1967.

B. Summary of M.S. Thesis of Joseph F. Fennell, "Van Allen Belt and ARGUS Directional Flux Density Distributions, Explorer 4 Satellite Data, ARGUS Event 2", Saint Louis University, Physics Department, July 1966.

C. Summary of Ph.D. Dissertation, John A. George, "Omnidirectional Fluxes; Explorer 4 Satellite Data, ARGUS Events 1 and 2", Saint Louis University, Physics Department, February 1967.

D. Summary of M.S. Thesis, Joseph R. Ockersz, S.J., "Omnidirectional Flux Densities of Geomagnetically Trapped Radiation Explorer 4 pre-ARGUS Times"; Saint Louis University, Physics Department, May 1966.

E. Summary of Pertinent Analytic Sections of Ph.D. Dissertation, Joseph M. Paikeday, "Interpretation of Directional Flux Densities in ARGUS Shells, Explorer 4 Satellite Data"; Saint Louis University, Physics Department, March 1966.

DD FORM 1 JAN 64 1473

Security Classification

Security Classification

14 KEY WORDS	LINK A		LINK B		LINK C	
	ROLE	WT	ROLE	WT	ROLE	WT
Analysis of Explorer IV Telemetry Records Geomagnetically Trapped Radiation Naturally and ARGUS Injected Geomagnetically Trapped Radiation Unidirectional and Omnidirectional Geomagnetically Trapped Radiation Natural and ARGUS Trapped Radiation in B-L Coordinates						

INSTRUCTIONS

1. ORIGINATING ACTIVITY: Enter the name and address of the contractor, subcontractor, grantee, Department of Defense activity or other organization *(corporate author)* issuing the report.

2a. REPORT SECURITY CLASSIFICATION: Enter the overall security classification of the report. Indicate whether "Restricted Data" is included. Marking is to be in accordance with appropriate security regulations.

2b. GROUP: Automatic downgrading is specified in DoD Directive 5200.10 and Armed Forces Industrial Manual. Enter the group number. Also, when applicable, show that optional markings have been used for Group 3 and Group 4 as authorized.

3. REPORT TITLE: Enter the complete report title in all capital letters. Titles in all cases should be unclassified. If a meaningful title cannot be selected without classification, show title classification in all capitals in parenthesis immediately following the title.

4. DESCRIPTIVE NOTES: If appropriate, enter the type of report, e.g., interim, progress, summary, annual, or final. Give the inclusive dates when a specific reporting period is covered.

5. AUTHOR(S): Enter the name(s) of author(s) as shown on or in the report. Enter last name, first name, middle initial. If military, show rank and branch of service. The name of the principal author is an absolute minimum requirement.

6. REPORT DATE: Enter the date of the report as day, month, year, or month, year. If more than one date appears on the report, use date of publication.

7a. TOTAL NUMBER OF PAGES: The total page count should follow normal pagination procedures, i.e., enter the number of pages containing information.

7b. NUMBER OF REFERENCES: Enter the total number of references cited in the report.

8a. CONTRACT OR GRANT NUMBER: If appropriate, enter the applicable number of the contract or grant under which the report was written.

8b, 8c, & 8d. PROJECT NUMBER. Enter the appropriate military department identification, such as project number, subproject number, system numbers, task number, etc.

9a. ORIGINATOR'S REPORT NUMBER(S): Enter the official report number by which the document will be identified and controlled by the originating activity. This number must be unique to this report.

9b. OTHER REPORT NUMBER(S): If the report has been assigned any other report numbers *(either by the originator or by the sponsor)*, also enter this number(s).

10. AVAILABILITY/LIMITATION NOTICES: Enter any limitations on further dissemination of the report, other than those imposed by security classification, using standard statements such as:

(1) "Qualified requesters may obtain copies of this report from DDC."

(2) "Foreign announcement and dissemination of this report by DDC is not authorized."

(3) "U. S. Government agencies may obtain copies of this report directly from DDC. Other qualified DDC users shall request through _____."

(4) "U. S. military agencies may obtain copies of this report directly from DDC. Other qualified users shall request through _____."

(5) "All distribution of this report is controlled. Qualified DDC users shall request through _____."

If the report has been furnished to the Office of Technical Services, Department of Commerce, for sale to the public, indicate this fact and enter the price, if known.

11. SUPPLEMENTARY NOTES: Use for additional explanatory notes.

12. SPONSORING MILITARY ACTIVITY: Enter the name of the departmental project office or laboratory sponsoring *(paying for)* the research and development. Include address.

13. ABSTRACT. Enter an abstract giving a brief and factual summary of the document indicative of the report, even though it may also appear elsewhere in the body of the technical report. If additional space is required, a continuation sheet shall be attached.

It is highly desirable that the abstract of classified reports be unclassified. Each paragraph of the abstract shall end with an indication of the military security classification of the information in the paragraph, represented as *(TS), (S), (C), or (U).*

There is no limitation on the length of the abstract. However, the suggested length is from 150 to 225 words.

14. KEY WORDS: Key words are technically meaningful terms or short phrases that characterize a report and may be used as index entries for cataloging the report. Key words must be selected so that no security classification is required. Identifiers, such as equipment model designation, trade name, military project code name, geographic location, may be used as key words but will be followed by an indication of technical context. The assignment of links, rules, and weights is optional.

Security Classification